UNIVERSITÀ DEGLI STUDI DI PADOVA

Dipartimento di Fisica e Astronomia "Galileo Galilei"

Master Degree in Physics

Final Dissertation

Electrical and photogalvanic properties of Fe:$LiNbO_3$ thin films fabricated by ion slicing

Thesis supervisor

Dr. Marco Bazzan

Candidate

Giulio Grazian

Academic Year 2019/2020

Dedicated to Elisabetta,
Teresa, Giorgio and Valeria

Abstract

With the constantly growing global energy demand and the connected deterioration of the physical environment, great efforts are being devoted to develop renewable and carbon-free energy sources. The ability of photovoltaic to harvest electric energy from light makes it one of the promising technologies to help solving the energy problem. Classical photovoltaic technology, which is based on p-n junctions, could be improved by the transition to ferroelectric materials that exhibit a bulk photovoltaic effect. These materials could provide access to higher power conversion efficiencies, thanks to their higher achievable open-circuit voltages, while the lack of a p-n junction would make them simpler and cheaper to fabricate. It has been recently proposed that a way to increase the conversion efficiency of ferroelectric photovoltaic could be through the use of nano-sized crystals. Focusing our attention on iron doped lithium niobate as a prototypical material, the proposed experiment involves the fabrication of Fe:LN heterostructures based on a commercial Fe:LN Smart-Cut™ thin film, with junctions on metal or semiconductor electrodes. The ultimate goal is to investigate how the current photogeneration behaves at the nano-scale; for this reason, it is mandatory to understand the physics behind the charge transport processes, the role of the interfaces and the impact of the ferroelectric switching on the final device. The study of the electrical and photogalvanic properties is achieved by analysing current-voltage characteristic curves measured with a source meter both in dark and lit conditions. The analysis of dark I-V curves shows that Richardson-Schottky and Poole-Frenkel models are the most appropriate ones to describe the charge transport in our samples, as expected from considering their band diagrams. Then, the particular current peaks observed in the case of PEDOT:PSS electrodes are attributed to the polarization switching of the crystalline film. Their characterization provides an estimation of the main related quantities, such as the spontaneous polarization and the coercive and residual fields, which are compared successfully with results from other works reported in literature. Finally, the measured photogalvanic currents are studied in relation to the illumination irradiance, producing results in line with those present in literature.

Contents

Chapter 1

Introduction

Human activities that are considered harmful for the physical environment are mainly related to the supply and usage of energy.

Nowadays, the global energy demand reaches over 10 millions GW h per year and shows a positive growth rate. Nonetheless, the demand in 2019 was covered for the 80 % by the use of fossil fuels and only the 14 % of renewable sources of energy. The burning of fossil fuels produces globally over 30 billion tonnes of CO_2 per year and natural processes can only absorb a small part of that amount. This results in a net increase of many billion tonnes of atmospheric CO_2 per year. CO_2 is a greenhouse gas that contributes to global warming, which can ultimately affect human behaviour and can prompt mass migrations or battles over clean water.[1]

Transportation is still responsible for 24 % of direct CO_2 emissions from fuel combustion: road vehicles account for nearly three-quarters of transport CO_2 emissions, while emissions from aviation and shipping continue to rise. However, with continuous technology announcements and with market and technology progress being made in electrification and battery performance, the rollout of electric vehicles is expanding quickly. In 2019 electric cars make up 2.6 % of global car sales and even shipping and aviation are making electrification progress. Nonetheless, with renewable energy sources taking only 28 % of share in electricity generation, it is clear that the benefits of transport electrification on CO_2 emissions will be greater only if electric-vehicle deployment takes place in parallel with the decarbonisation of power systems.[1–4]

The lack of electricity access for 850 million people around the world is another major energy-related problem that requires to be addressed.[5]

Optimal use of renewable energy sources minimize environmental impacts, produce minimum secondary wastes and are sustainable based on current and future economic and societal needs. Photovoltaic conversion of sunlight to electricity is one of the promising technologies to solve the energy problem that our society is facing. Thin-film solar cells are made from a variety of semiconductors including amorphous and polycrystalline Si, GaAs, CdTe and organic semiconductors.[6,7]

In a semiconducting material, the absorption of photons with energies above the band gap, $h\nu \geq E_g$, results in the promotion of electrons from the valence band to the conduction band. The process generates holes and electron carriers. In a typical material these excited carriers will decay back to the ground-state, with energy being conserved by the emission of light and/or heat. The photovoltaic effect occurs when an internal electric potential across the material or selective electrical contacts prevents charge recombination, producing a net flow of photogenerated electrons and holes. A method of creating asymmetry for charge separation is to establish a p-n junction by doping different regions of a single crystalline semiconductor, such as silicon, with different impurities providing a high concentration of free carriers with opposite sign, *e.g.* with phosphorous and boron.[8]

The ideal photovoltaic material should separate charges as efficiently as possible, with minimal relaxation of the charge carriers produced from the optical excitation, and transport them independently to the external circuit minimising recombination between electrons and holes. The overall power conversion efficiency η of incident light power P_{in} to electricity may be written as:

$$\eta = \frac{V_{\text{oc}} J_{\text{sc}} FF}{P_{\text{in}}} \ . \tag{1.1}$$

The open circuit voltage V_{oc} is the potential difference developed across a cell under illumination when the terminals are not connected. This represents the maximum voltage which can be generated by the cell and is limited, in a standard semiconductor junction, by the band gap of the absorber layer. The short-circuit current J_{sc} is the photo-current extracted when the voltage across the cell is zero and it is limited by the proportion of the solar spectrum absorbed by the active material in a device. The realised power at the maximum power point on the J–V curve as a fraction of the idealised power is the fill-factor, FF. Recombination of photo-generated electrons and holes limits the efficiency of operating solar cells.

The recombination processes, together with the open-circuit voltage being constrained by the energy band gap of the semiconductor, define the ultimate efficiency of a standard single junction solar cell. A maximum light to electric power efficiency at standard conditions of 33.16 % is predicted for a single function solar cell by following Shockley and Queisser considerations.[9]

The current production of solar cells is dominated by crystalline silicon modules technology because of their mature fabrication techniques and relatively high efficiency. Nonetheless, the crystalline silicon wafers used in solar photovoltaics, which typically have a thickness between 180 and 300 μm, are relatively expensive, leading to the difficulty for making power from photovoltaic competitive with fossil fuel technologies. Alternative photovoltaic mechanisms have to be explored in pursuit either of lower cost and/or improved efficiency.[7]

Light-to-electricity energy conversion in ferroelectrics was envisioned 40 years ago by V. M. Fridkin, who imagined a "photoferroelectric crystal" as a potential solar cell.[10] In those materials, the intrinsic spontaneous polarization gives rise to several light-to-current phenomena that could possibly be used in an energy harvesting context. Among them, the bulk photovoltaic effect has attracted interest either at fundamental level and for practical applications. The BPVE consists in the spontaneous generation of a bulk current under uniform illumination. It is a material's property and does not rely on any physical interface, such as a junction. Due to the high resistance of many ferroelectrics, this current may build up extremely high open-circuit voltages. Moreover, being originated by an intrinsically different microscopic mechanism, BPVE is not *a priori* limited by Shockley-Queisser argument, so that in principle one could hope to improve the conversion efficiency over that of semiconductor p-n junctions. There are additional potential advantages to such device designs: for example, the lack of p–n interface ensures that the entire photovoltaic material is active for current generation and allows for a simple and robust fabrication process;[11] ferroelectric oxides are also stable in a wide range of mechanical, chemical and thermal conditions and can be fabricated using low-cost methods, such as sol–gel thin-film deposition and sputtering.[12]

However, the development of ferroelectric based photovoltaic devices has mostly remained the preserve of academic research. Industry adoption is hampered by the low efficiency, which is still not competitive with p-n solar cells. In spite of this, in recent times ferroelectric materials regained interest when research works finally demonstrated a possible improvement on the light energy conversion efficiency, which could potentially become competitive with semiconductor technology.

The bulk photovoltaic effect observed in the noncentrosymmetric crystals depends on the relative contribution of nonthermalized excited carriers over thermalized ones, that in ferroelec-

tric material become polaronic carriers, self-localized in the band gap and characterized by low mobility. At the nanoscale, when the thickness of the ferroelectric crystal l is comparable to the free path of the nonthermalized electron l_0, the conversion efficiency can be expected to become much larger. For $l \sim l_0$, all excited carriers are nonthermalized and contribute to the photogenerated current.[13,14] This idea is corroborated by preliminary measurements on ferroelectric $BaTiO_3$ films with thickness of few tens of nanometers, revealing an increase by 4 orders of magnitude of the photoinduced electric field in the film and of the efficiency of the light energy conversion, as compared to the bulk material.[13] However, this approach is still under debate and a deeper investigation of the phenomenon of nano-BPVE is mandatory in view of its importance for a practical application.

Several material are known to manifest the bulk photovoltaic effect. The choice of focusing our attention on iron doped lithium niobate is driven by the opportunity of studying it as a prototypical case: it is readily available in high quality at a reasonable price and is a widely studied, well known ferroelectric material, which can be prepared in the form of nanofilms with high crystal quality.

The long-goal of the present reasearch is to investigate how the photogeneration of currents in Fe-doped $LiNbO_3$ thin films is affected by a decrease of the film thickness to the hot carriers thermalization length. To this end, it is very important to develop a robust methodology to measure small currents in Fe:LN. This problem, however, is not trivial in itself. A Fe:LN thin film sandwiched between two metal electrodes constitutes a metal-insulator-metal system where the charge transport is governed by a set of different microscopic mechanisms. The presence of polarization charges at the interfaces further complicates the analysis of the current response of the system. In this context, this thesis aims to study the conduction mechanism, the polarization currents and the photogalvanic currents in a commercially available Fe:LN 300 nm thin film, with the purpose of developing a reliable measurement protocol.

After a brief introduction on lithium niobate in chapter 2, in chapter 3 is described the charge transport modeling both in the bulk of the material, which is mainly due to small polarons, and in Fe:LN heterostructures, which will be treated in first approximation as metal-insulator-metal systems.

The experimental details are then presented in chapter 4. In particular, the details on the Fe:LN Smart-Cut™ film, the choice of three top electrodes (aluminum, PEDOT:PSS and indium tin oxide) and the process of samples preparation are discussed in section 4.1, together with a brief introduction to the techniques involved in the fabrication of the film and in the deposition of the electrodes. Then, in section 4.2 is described the experimental apparatus and the electronic instruments that are used to perform the measurements. The characterization of the two LEDs needed for measuring the photogalvanic currents is also included in this section. Finally, the methodes employed in the electrical measurements are discussed in section 4.3.

In chapter 5 are presented and discussed all the results concerning the electrical measures. Starting in section 5.1 with a simple determination of the most appropriate time to wait for the currents to reach steady state, the focus moves in section 5.2 to the study of the conduction of our samples, which will be based on the charge transport models discussed for the metal-insulator-metal heterostructures in chapter 3 and will be carried on by analysing the measured current-voltage characteristics in particular coordinate systems. Then, the study of particular current peaks emerging from the I-V curves for the PEDOT:PSS electrode, acknowledged to be related to the polarization switching of the Fe:LN film, is presented in section 5.3. Finally, in section 5.4 are presented the measures we obtained for the photogalvanic currents at two different wavelengths, for the two transparent electrodes.

Chapter 6 contains, finally, a summary of the results obtained in the previous chapter.

Chapter 2

Lithium niobate

Lithium niobate ($LiNbO_3$) is an artificial dielectric material that was first discovered to be ferroelectric in 1949 by Matthias and Remeika. It was synthesized in single crystal form and investigated in detail at Bell Laboratories, resulting in a cornerstone of five papers published in 1966. It is now one of the most widely used electro-optic materials.[15–21]

This material is optically transparent in the range of wavelengths from 0.35 to 5 μm and is characterized by large pyroelectric, piezoelectric, electro-optic and photoelastic coefficients, is naturally birefringent and has useful acoustic wave properties.[22] In addition, it exhibits a noticeable strong bulk photovoltaic effect, which in combination with the material's linear electro-optic effect can produce a significant photorefractive effect. This richness of strong physical effects has caused lithium niobate to become widely used in a plethora of applications, from acoustic filters to integrated optics.

2.1 Crystal structure

Below its ferroelectric Curie temperature, around 1210 °C in congruent $LiNbO_3$, lithium niobate's structure consists of planar sheets of oxygen atoms in a distorted hexagonal close-packed configuration. The octahedral interstices formed in this structure are one-third filled by lithium atoms, one-third filled by niobium atoms and one-third vacant. Above the Curie temperature, lithium niobate is in the paraelectric phase, which is non-polar. As the temperature decreases from the Curie temperature, the elastic forces of the crystal become dominant and force the lithium and niobium ions into new positions. The charge separation resulting from this shift of ions relative to the oxygen octahedra causes the material to exhibit spontaneous polarization, thus classifying $LiNbO_3$ as a member of the class of displacement ferroelectrics. The position of the Li and Nb atoms in both the paraelectric and ferroelectric phases are shown in figure 2.1.

In the ferroelectric phase, a lithium niobate crystal exhibits three-fold rotation symmetry about its c axis, a property related to the trigonal crystal system. In addition, it exhibits mirror symmetry about three planes that are 60° apart and intersect forming a three-fold rotation axis. In the trigonal system, two dfferent unit cells can be chosen: hexagonal and rhombohedral. The conventional hexagonal unit cell in $LiNbO_3$ contains six formula weights, while the conventional rhombohedral unit cell contains only two formula weights.

We will focus only on the hexagonal unit cell, which is shown in figure 2.2. In this unit cell, the c axis is defined as the axis about which the crystal exhibits three-fold rotation symmetry. The $+c$ axis is directed out of the c face that becomes negative upon compression. This method can be understood qualitatively by considering the movement of the Li and Nb ions relative to the oygen octahedra. Their undisturbed positions relative to the oxygen octahedra at room

temperature are also shown in figure 2.2. Upon compression, the ions move closer to their centered paraelectric positions with respect to the oxygen layers, thereby reducing the net polarization and leaving an excess amount of negative compensating charge on the $+c$ face, causing the $+c$ face to become negative.

The three equivalent a axes (a_1, a_2, a_3) of the conventional hexagonal unit cell are 120° apart and lie in a plane normal to the c axis. According to the adopted convention, these axes are chosen to be perpendicular to the mirror planes of symmetry.

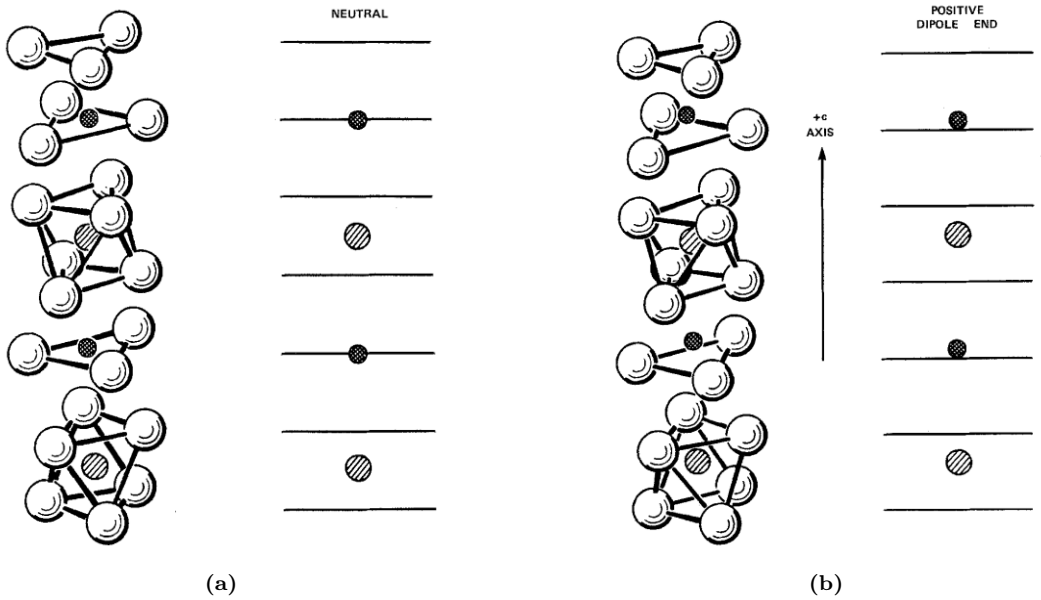

Figure 2.1: *crystal structure of $LiNbO_3$ in (a) paraelectric and (b) ferroelectric phases, from [16].*

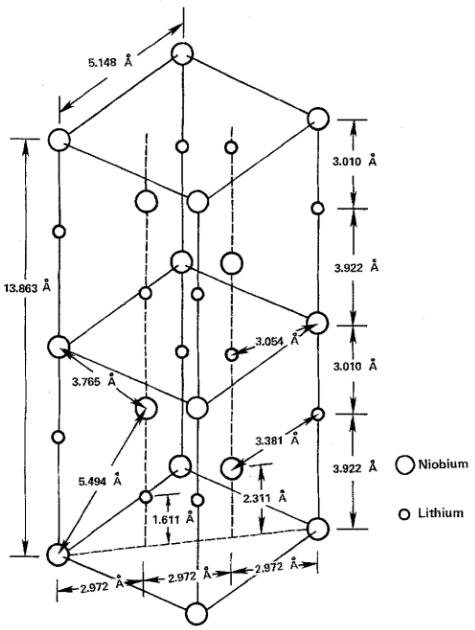

Figure 2.2: *$LiNbO_3$ hexagonal unit cell with undisturbed interatomic distances at room temperature, from [16].*

Crystal properties, which will be described in more detail in the following, are best described in tensor form in a orthogonal coordinate system. The conventional choice of coordinate system for lithium niobate is a right-handed system with the x-axis along one of the hexagonal a axes, the z-axis along the c axis and the y-axis along the direction defined by the vector product $z \wedge x$. Vector properties such as spontaneous polarization and pyroelectricity exist along the z-axis.[23]

Suppliers of lithium niobate crystals provide pieces that are commonly in the form of plates. These slices may be designated x-, y- or z-cut corresponding, respectively, to the x, y or z axis being normal to the large area surfaces.

2.2 Composition variants

We described so far lithium niobate only in the *stoichiometric* composition variant. This variant corresponds to an equal proportion of Li and Nb atoms in the material. But lithium niobate is a material with variable composition, as can seen from the phase diagram of the Li_2O - Nb_2O_5 system in figure 2.3. For example, there are areas in the phase diagram consisting of both $LiNbO_3$ oxide and either Li_3NbO_4 or $LiNb_3O_8$, which are centrosymmetric and therefore non-ferroelectric phases.[22]

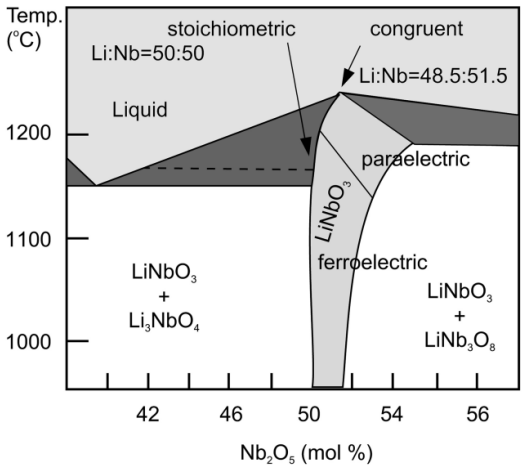

Figure 2.3: *phase diagram of the Li_2O - Nb_2O_5 system near the congruent and stoichiometric composition of $LiNbO_3$, from [24].*

As a matter of fact, lithium niobate is encountered in applications mostly in its *congruent* phase. Congruent $LiNbO_3$ crystals present a Li deficiency, usually measured as $R = [\mathrm{Li}]/([\mathrm{Li}] + [\mathrm{Nb}])$, where the square brackets denote concentration in mol.%. Typically, congruent $LiNbO_3$ measures R around 0.485. At the congruent composition, the melt used for the crystal growth and the growing crystal are identical with respect to the composition, so these crystals show the highest uniformity of properties. In other cases, the composition of the melt and the crystal vary during the growth and the crystal becomes compositionally non-uniform along the growth axis. The [Li]/[Nb] ratio influences strongly the physical properties of the material, especially the optical and the ferroelectric ones.[25]

The shortage of lithium during the growing process, which causes the non-stoichiometry, can be described by various possible processes of Li_2O out diffusion. Charge compensation after Li_2O out diffusion is ensured by structure modifications. The two most accepted models are the *lithium vacancy model* and the *niobium vacancy model*. The first one predicts that some lithium

vacancies are compensated by niobium atoms and is described by the following reaction:

$$\langle\langle \mathrm{LiNbO_3} \rangle\rangle \rightarrow 3\mathrm{Li_2O} + 4V_{\mathrm{Li}}^{-} + \mathrm{Nb}_{\mathrm{Li}}^{4+} \ ,$$

the second one predicts instead that all the lithium vacancies are filled with niobium antisites, leading to the formation of niobium vacancies, and is described by the following reaction:

$$\langle\langle \mathrm{LiNbO_3} \rangle\rangle \rightarrow 3\mathrm{Li_2O} + 4V_{\mathrm{Nb}}^{-} + 5\mathrm{Nb}_{\mathrm{Li}}^{4+} \ .$$

Here V_{Li}^{-} and V_{Nb}^{-} are a lithium and a niobium vacancy respectively, with the minus sign as superscript representing the negative charge state of the defect with respect to the host, and $\mathrm{Nb}_{\mathrm{Li}}^{4+}$ is a niobium antisite defect at V_{Li}^{-}, with 4+ as superscript representing the positive charge state of the defect with respect to the host. The generation of antisite defects and degree of filling the lithium sites by niobium ions depends in general on the growth conditions. At the congruent composition, the lithium vacancy model would cause the presence of a high concentration of about 2×10^{20} cm^{-3} antisite defects. This is the most frequently encountered situation.

A very reliable and accurate indicator of a particular sample's stoichiometry is its Curie temperature. Comparison of the measured Curie temperature with critical temperatures of known stoichiometry uniquely determines the chemical composition of the sample.[16]

2.3 Main physical properties

Pyroelectric effect

A pyroelectric solid exhibits a change in spontaneous polarization in response to a change in temperature. The relationship is linear between the two and can be written as

$$\Delta \mathbf{P} = \tilde{p} \Delta T \tag{2.1}$$

where $\tilde{p}$ is the pyroelectric tensor. In lithium niobate this effect is due to the movement of lithium and niobium ions relative to the oxygen layers. Since the Li and Nb ions move only in a direction parallel to the c-axis, in tensor component form equation 2.1 may be written as $\Delta P_i = p_i \Delta T$, with

$$p_i = \begin{bmatrix} 0 \\ 0 \\ p_3 \end{bmatrix} \tag{2.2}$$

with $p_3 = -4 \times 10^{-5}$ C K^{-1} m^{-2}.[16]

Permittivity

The relationship between electric flux density $\mathbf{D}$ and electric field $\mathbf{E}$ in linear and can be written as

$$\mathbf{D} = \tilde{\varepsilon} \mathbf{E} \tag{2.3}$$

where $\tilde{\varepsilon}$ is the second-rank permittivity tensor. Equation 2.3 may be expressed in tensor component form as $D_i = \sum_j \varepsilon_{ij} E_j$, where $i, j = x$, y or z. In lithium niobate, only the diagonal elements of the permittivity tensor are non-zero; moreover, since lithium niobate is symmetric about the c axis, the permittivity is the same for x and y directions. Therefore,

$$\varepsilon = \begin{bmatrix} \varepsilon_{11} & 0 & 0 \\ 0 & \varepsilon_{11} & 0 \\ 0 & 0 & \varepsilon_{33} \end{bmatrix} \tag{2.4}$$

Permittivity is often normalized in terms of the permittivity of vacuum, ε_0. The dimensionless constant $\varepsilon_{ij}/\varepsilon_0$ is called dielectric constant. The dielectric constant along the z-axis is measured to be around 28; the dielectric constant along the x and y axes is about 45 when a constant strain is applied, 85 at zero stress.[16,26]

Bulk photovoltaic effect

The bulk photovoltaic effect is manifested as a short-circuit current through a solid that is uniformly illuminated. This effect is a material's property and, differently from other situations where light is converted into electrical current, does not require any inhomogeneity in the illumination or in the material (due, for example, to the presence of a junction). For this reason, it was first described as an "anomalous" photovoltaic effect by Glass 1974.[27] The tensor relationship between the short-circuit current density and the illumination can be written

$$J_i = \sum_{jk} = \beta_{ijk} E_j E_k^* \tag{2.5}$$

where J_i is the current density vector, $E_{j,k}$ are components of the light complex electric field vector (* represents complex conjugation) and β_{ijk} is the third-rank photovoltaic tensor. Since $E_j E_k^* = E_j^* E_k$, β_{ijk} has only four non-vanishing independent components that depend on the crystal properties and can be written as a 3×6 matrix as follows:

$$\beta_{ijk} = \begin{bmatrix} 0 & 0 & 0 & 0 & \beta_{15} & -2\beta_{22} \\ -\beta_{22} & \beta_{22} & 0 & \beta_{15} & 0 & 0 \\ \beta_{31} & \beta_{31} & \beta_{33} & 0 & 0 & 0 \end{bmatrix} \tag{2.6}$$

with measured values $\beta_{22} = 1.5{\times}10^{-10}$ A/W, $\beta_{31} = 6{\times}10^{-9}$ A/W and $\beta_{33} = 6.8{\times}10^{-9}$ A/W (β_{15} was not measured), obtained for Fe:$LiNbO_3$.[28] The bulk photovoltaic effect in lithium niobate will be described in more detail in section 3.1.3.

Photorefractive effect

The photorefractive effect, which refers to optically induced changes in the refractive index of the material, is produced by a two step process: charge migration, produced by mainly by bulk photovoltaic effect, followed by a linear and/or quadratic electro-optic effect, which consists in a change of the refractive index under the application of an electric field. This effect raised significant interest during the 90s, beacause it allows a large plethora of light-induced effects even at low intensities, such as beam coupling, phase conjugation, hologram recording and optical damage.

2.4 Fabrication of LN thin films

Many applications require the lithium niobate to be used as a thin film. It is very important for the synthesis method to preserve in the thin film the elemental composition and crystalline structure of a bulk material.

Standard deposition methods, such as liquid phase epitaxy, chemical vapor deposition, pulsed-laser deposition and radio frequency magnetron sputtering, have been used successfully in the fabrication of single phase $LiNbO_3$ films on different types of substrates, for example, lithium niobate itself, sapphire or SiO_2. However, the produced films are still plagued by compositional and structural defects that may hinder the final application. Moreover, those methods are bound

to be used on substrates with a lattice structure favouring the epitaxial growth of the LN films, which limits significantly the type of devices that can be produced.

Nowadays, ion slicing techniques are also employed for tranferring thin slices of material from the surface of a single crystal to different types of substrates. This method is gaining more and more consideration among the LN community as it provides the freedom to deposit a high-quality crystalline film on virtually any substrate. The iron doped lithium niobate films that will be studied in this work are fabricated by NANOLN with a patented ion slicing technique called Smart-Cut™, which will be described in more detail in section 4.1.1.

Chapter 3

Theoretical background

3.1 Bulk charge transport models

3.1.1 Polaron conduction

Being a polar material, $LiNbO_3$ is characterized by a strong interaction between electrons (or holes) and the lattice. In this situation, the classical band transport models used for semiconductors or metals are not appropriate, as the charge carriers very quickly lose energy and tend to form electron or hole polarons. A small polaron can be created when the interaction of a carrier with the surrounding lattice is sufficiently strong to induce a self-trapping of the carrier at one site. Due to the vibration of the surrounding ions, the equilibrium positions of this carrier are displaced. Irregularities of the lattice are enough to cause complete localization of a carrier at one site. The polaronic model is one of the most widely used approaches to describe charge phenomena in lithium niobate and the main charge transport mechanism in this situation is the thermally activated tunneling (hopping).

Charge carriers in single crystal $LiNbO_3$ are strongly influenced by the point intrinsic or extrinsic defects. The three main sources of ionic defects in $LiNbO_3$ are: the impurity content, the non-stoichiometry in Li/Nb and the intrinsic ionic disorder. The intrinsic ionic disorder is the predominant source of ionic defects.

In lithium niobate, the small bound polaron is created if electrons are captured at the niobium antisite defect Nb_{Li}^{4+}. A bound bipolaron can also be formed when the nearest defect pair Nb_{Li}^{4+} - Nb_{Li}^{4+} is able to capture two electrons. The presence of extrinsic ions, like Fe_{Li}^{2+} in iron doped lithium niobate (iron is present in iron doped lithium niobate in two configurations, Fe^{2+} and Fe^{3+}), supports the generation of small bound polarons thanks to their capability of capturing an electron. Also bipolarons $Nb_{Nb}^{4+} : Nb_{Li}^{4+}$ and hole polarons O^{-}, V_{Li} are intrinsic small polarons in iron doped lithium niobate. Nonetheless, bipolarons are usually not observed because the system tends to relax to the more stable Fe defect, while hole polarons are produced at very high visible light intensity pulsed beams by two-photon processes and such high intensities and pulsed illumination are beyond the scope of the present work.

Experimental evidence suggests that electrons are the major carriers in $LiNbO_3$ films, because potentially free electrons can be generated in lithium niobate from oxygen vacancies and from the generation of niobium antisite defects at lithium vacancies, as described by the following reactions:[29]

$$V_O \longleftrightarrow V_O^{+} + e^{-}$$

$$3O + 2V_{Li}^{-} + Nb \longleftrightarrow \tfrac{3}{2}O_2 + Nb_{Li}^{4+} + 6e^{-}$$

Free electrons can be introduced into the lattice also thanks to thermal treatments performed in reducing atmosphere. In this way, a part of the deep impurities, such as Fe^{3+}, is converted

to Fe^{2+}. Those centers can be forced to release their electron by illuminating the material with visible light.

3.1.2 Dark and photoconductivity

Undoped lithium niobate is an insulator material with a band gap of about 3.9 eV. Its conductivity is therefore very poor in the dark. However, it can be increased by several orders of magnitude when the material is doped with Fe and/or when it is illuminated by a sufficiently energetic photon stream. If an electric field E is applied throughout the material, a drift current J_{drift} arises. The drift current density is $J_{\text{drift}} = (\sigma_{\text{d}} + \sigma_{\text{ph}})E$, where σ_{d} and σ_{ph} are the dark conductivity and photoconductivity respetively.

The dark conductivity of the material can be written simply as $\sigma_{\text{d}} = e\mu n$, with n and μ respectively the density and the mobility of the charge carriers in the solid.

Doping a lithium niobate film with iron has a major impact also on its dark conductivity and in particular the iron-induced dark conductivity becomes dominant for iron concentrations larger than about 20×10^{18} cm^{-3}.[30] The physical origin of the iron-induced dark conductivity could reside in the tunneling of electrons between iron sites, as suggested by the work presented in [30].

Several research works suggest that the dark conductivity in Fe:LN depends exponentially on the iron concentration, obeying the relation

$$\sigma_{\text{d}}(c_{\text{Fe}}) \propto \exp\left(a\ {c_{\text{Fe}}}^{b}\right) \tag{3.1}$$

with a a constant and b an exponent. For example, in [31] the iron concentration has power $b = 1$ in equation 3.1, in [30] $b = 1/3$, in [32] $b = 1/4$. The differences in the iron concentration's exponent b are thought to be due to different $c_{\text{Fe}^{2+}}/c_{\text{Fe}^{3+}}$ ratios in the various experiments.

The photoconductivity σ_{ph} may again be expressed as $\sigma_{\text{ph}} = e\mu n$, this time with μ being the drift mobility of the light-induced carriers in the material and n their density. Using a rate-equation system in a band-like description of the iron doped lithium niobate, the photo-excited carriers concentration can be explicitly determined and the photoconductivity can also be written as:[33]

$$\sigma_{\text{ph}} = esN\frac{I}{h\nu}\phi\mu\tau \tag{3.2}$$

where N is the concentration of Fe^{2+} donors and s their cross section, I the light intensity, $h\nu$ the photon energy, ϕ the photo-generation efficiency factor, also referred to as quantum efficiency, *i.e.* the probability to create a charge contributing to the current from an absorbed photon, and τ the light-induced carriers lifetime. However, this description is probably not adequate in the case of polarons because quantities as the polaron lifetime τ and mobility μ are ill-defined in this case.

The mentioned problems can be overcome by considering the quantity that in a band model is given by the product $\mu\tau$, instead of considering μ and τ separately. The product $\mu\tau \equiv \Lambda$ is the average distance $\langle z \rangle$ run by a polaron under unitary electric field from its generation to its trapping:

$$\Lambda = \frac{\langle z \rangle}{E} \tag{3.3}$$

and is called the drift coefficient. This quantity is properly defined also in the case of polaron transport and can be computed by a Monte Carlo simulation.

3.1.3 Bulk photovoltaic effect and photogalvanic current

Apart from the drift current arising when an electric field is applied to Fe:LN, there is another current source that manifests itself as the spontaneous appearance of a high voltage along the z direction of the crystal when it is exposed to visible uniform light. The peculiarity of this phenomenon is that it occures in the bulk of the material, without the need for any inhomogeneity, *e.g.* the illumination intensity or the presence of a junction. For this reason it is dubbed *bulk photovoltaic effect*.

The bulk photovoltaic effect (also anomalous photovoltage or photogalvanic effect) is in fact due to the onset of a current through a solid that is uniformly illuminated and has been observed and described by Glass in 1974. According to [16], a phenomenological tensor relationship between the short-circuit current density and the illumination can be written

$$J_i = \sum_{jk} \beta_{ijk} E_j E_k^* \tag{3.4}$$

where J_i is the current density along the i axis, E_j and E_k components of the light complex electric field vector, β_{ijk} the third-rank photovoltaic tensor. Since $E_j E_k^* = E_j^* E_k$, β_{ijk} has only four non-vanishing independent components that depend on the crystal properties.

The photogalvanic current density J_{PG}, observed along the polar c-axis under uniform illumination, is proportional to the absorbed power density and can also be written:

$$J_{\mathrm{PG}} = \kappa \alpha I = esN \frac{I}{h\nu} \phi L_{\mathrm{PG}} \ , \tag{3.5}$$

where, again, N is the concentration of excitable Fe^{2+} sites and s their cross section, I the light intensity, $h\nu$ the photon energy, ϕ the quantum efficiency and L_{PG} the photogalvanic length; still, $\alpha = sN$ is the absorption coefficient, while κ is the Glass factor.

The origin of the photogalvanic current in Fe:$LiNbO_3$, from an atomic standpoint, is thought to be due to asymmetric charge transfer along the c axis, triggered by the absorption of a photon. The photo-excited charges initially are transported from Fe_{Li}^{2+} to Nb_{Nb}^{5+} conduction band states and the subsequent coherent band-like electron transport is terminated by the formation of Nb_{Nb}^{4+} free small polarons. These free polarons, transported by thermally activated incoherent hopping, are then trapped by deeper defects such as Nb_{Li}^{5+} and Fe_{Li}^{3+} impurities.[34] During their incoherent hopping and before being trapped by a deep level, free small polarons can form a bound small polaron at Nb_{Li}^{4+}.

3.1.4 Monte Carlo simulation of the photoconductivity

The simplest numerical approach consists in simulating one single electron at time. This situation corresponds to a low electron density system where interaction between electrons can be ignored. The electron is randomly placed at an initial Nb_{Nb} site and performs a walk in a structure reproducing the LN lattice. The code, provided by Dr. Marco Bazzan, generates a random defect configuration in a $80 \times 80 \times 80$ super-cell of the LN structure with periodic boundary conditions, in which the polaron is launched. The position at which it is captured by a Fe^{3+} trap is recorded. The defect concentrations are set as follows:

$$[\mathrm{Nb_{Li}}] = 19.0 \times 10^{25} \ \mathrm{m}^{-3}$$

$$[\mathrm{Fe_{tot}}] = 1.89 \times 10^{25} \ \mathrm{m}^{-3}$$

The code computes the rest time on each visited site and the next destination site according to the equations 3.6 and 3.7 for the non-adiabatic hopping frequency $w_{i,f}$ and for the hopping

barrier $U_{i,f}$, as predicted by the Marcus-Holstein polaron hopping model. The initial and final states, i and f respectively, can be the free polaron state Nb_{Nb}^{4+} (FP), the bound polaron state (GP) and the iron defect state.

$$w_{i,f}(r,T) = \frac{1}{2}\left(\frac{\pi}{kT\lambda_{i,f}}\right)^{1/2} \frac{{I_{i,f}}^2}{\hbar} \exp\left(-\frac{r}{a_{i,f}} - \frac{U_{i,f}}{kT}\right) \tag{3.6}$$

$$U_{i,f} = \frac{(2E_i + \epsilon_i - \epsilon_f)^2}{4(E_i + E_f)} \tag{3.7}$$

In equation 3.6, r is the distance between initial and final states, T the absolute temperature, $\lambda_{i,f}$ the reorganization energy corresponding to the energy paid to rearrange the lattice, equal to the sum of the elastic energies of the two polarons, $a_{i,f}$ an orbital parameter describing the overlap between the elctronic wavefunctions at sites i and f, $I_{i,f}$ the pre-exponential factor that describes the intrinsic hopping rate between two sites. In equation 3.7, instead, E_i and E_f are the elastic energies of the polarons, ϵ_i and ϵ_f the pre-localization energies of the electron at zero deformation.

The probability to hop from a site i to a site f is computed as:

$$P_{i,f} = \frac{w_{i,f}}{\sum_f w_{i,f}}$$

where the summation at the denominator goes on all the possible destination sites inside a suitably defined volume surrounding the starting site.

The simulation was repeated for 5×10^4 polarons and for ten different electric fields, spanning a range going from 0.667 to 6.667×10^7 V/m, which corresponds to a range of voltages going from 2 to 20 V in our 300 nm films. The experimental temperature was set to 300 K. The simulations for the electric fields in the range from 0.667 to 3.333×10^7 V/m have been performed by Giovanni De Nardus.

The simulation allowed to compute the average distance $\langle z \rangle$ along the field direction run by the particles before being captured for ten different applied fields, as shown in figure 3.1a.

From equation 3.3, the values of Λ were also calculated for the different fields. They are presented in figure 3.1b.

Remembering equations 3.2 and 3.3, the results shown in figure 3.1 predict an almost linear polaronic conduction in the studied range of fields.

In figure 3.2 are presented also the distributions of the x, y and z coordinates of the trapping distance from the initial site simulated at 6.667×10^7 V/m. As can be seen, the displacement along x and y averages to zero, while the z coordinate is clearly shifted towards positive values, *i.e.* towards the direction of the applied field.

The parameters of the simulations are summarised in table 3.1.

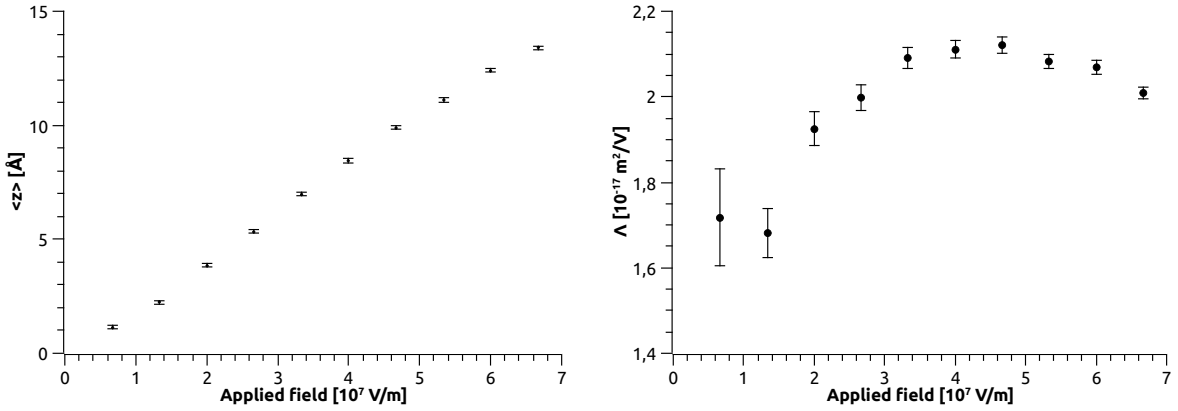

(a) (b)

Figure 3.1: *$\langle z \rangle$ and Λ obtained from the simulations.*

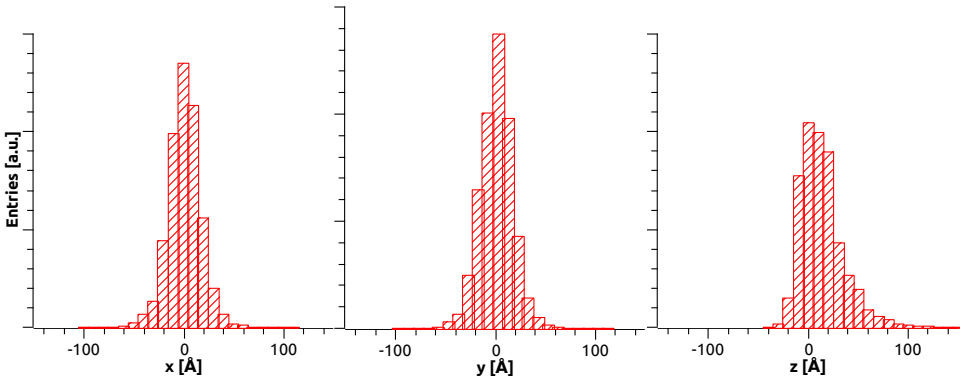

Figure 3.2: *distributions of trapping distances from initial site, along x, y and z coordinates.*

Parameter	Value	Unit
E_{FP}	0.545	eV
E_{GP}	0.75	eV
E_{Fe}	0.7	eV
ϵ_{FP}	0	eV
ϵ_{GP}	0.2	eV
ϵ_{Fe}	1.22	eV
$a_{\mathrm{FP,FP}} = a_{\mathrm{GP,GP}} = a_{\mathrm{GP,FP}} = a_{\mathrm{FP,GP}}$	1.6	Å
$a_{\mathrm{FP,Fe}} = a_{\mathrm{GP,Fe}}$	1.3	Å
$I_{\mathrm{FP,FP}} = I_{\mathrm{FP,GP}} = I_{\mathrm{GP,FP}} = I_{\mathrm{GP,GP}}$	0.1	eV

Table 3.1: *the parameters of the simulation, as reported in [33].*

3.2 Fe:LN heterostructures

Part of the goals of this thesis is to understand the behaviour of a thin film of Fe:$LiNbO_3$ in terms of charge transport and this is experimentally done by observing the current output as a response to an external voltage bias. The film, however, cannot be studied without the ability to connect its $\pm z$ faces to an external circuit; the studied samples are therefore designed to have bottom and top electrodes, essential for creating the two electrical contacts needed for the application of the voltage bias and the measure of the output current. Lithium niobate can be treated like an insulator because of its large bandgap of 3.9 eV.[35] Thus, the most appropriate way to model the conduction process in our samples is to consider them as metal-insulator-metal (M-I-M) systems.

Note that two out of the three top electrodes that will be used are not actually metals and they should be referred to more correctly by calling them conductors. Nonetheless, the models based on the M-I-M system are good starting points, because they give a general idea of the expected behaviour of the film when the presence of the electrodes gives rise to potential barriers at the interfaces. In fact, the conductivity of a M-I-M system is determined not only by the insulator properties, but also and mostly by how the insulator interacts with the electrodes.

The various conduction processes can be classified under two groups: bulk-limited conduction and electrode-limited conduction. In order to distinguish them, it is important to understand the existing contact between the electrode and insulator.

3.2.1 Energy diagrams of contacts

The action of the insulator is to erect between the electrodes a potential barrier extending from the electrode Fermi level to the bottom of the insulator conduction band. The principles that determine the height of the potential barrier and the shape of the bottom of the conduction band within the insulator are:[36]

1. the continuity of vacuum and Fermi levels of electrode and insulator across the interface;

2. the energy difference between the insulator vacuum and Fermi levels far enough from the interface is equal to the work function ψ_i of the insulator.

The first condition determines the height of the interfacial barrier to be, ideally, $\phi_0 = \psi_m - \chi$, where ϕ_0 is the interfacial barrier height, χ the insulator electron affinity and ψ_m the work function of the metal electrode.

It is not the height of the barrier that determines the conduction process; rather it is the type of the contact. The types of contact that can exist at a metal-insulator interface fall into three categories: ohmic contact, neutral contact and blocking contact.

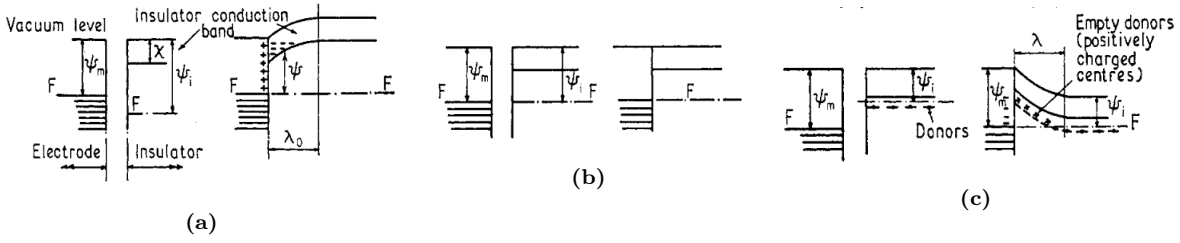

Figure 3.3: *band diagrams for (a) ohmic, (b) neutral and (c) blocking contacts (images from [36]). F is the Fermi energy.*

An *ohmic contact* is achieved when the electrode work function ψ_{m} is smaller than the insulator work function ψ_{i} (see figure 3.3a). In order to reach the thermal equilibrium under this condition, electrons are injected from the electrode into the conduction band of the insulator, creating a space-charge region and hence a space-charge induced electric field in it. This space-charge region extends to a distance

$$\lambda = \frac{\pi}{2}\left(\frac{2kTK\varepsilon_0}{e^2N_t}\right)^{1/2}\exp\left(\frac{\psi_{\mathrm{i}}-\chi-E_t}{2kT}\right) \tag{3.8}$$

into the insulator and is called *accumulation region*.[36] In the expression for λ, k is the Boltzmann's constant, T the temperature, K the insulator dielectric constant, ϵ_0 the permittivity of free space, e the elementary charge, χ the insulator electron affinity, N_t the concentration of shallow electron traps positioned at an energy E_t below the bottom of the conduction band.

The ohmic contact acts as a reservoir of charges and can supply electrons to the insulator as required by bias conditions. The conduction process in this case is limited by the rate at which the electrons can flow through the bulk of the insulator and is not limited by the rate at which they are supplied to it. Therefore this conduction mechanism is bulk-limited.

A *neutral contact* occurs when $\psi_{\mathrm{m}} = \psi_{\mathrm{i}}$ (see figure 3.3b). In this case, the vacuum and Fermi levels of the insulator and electrode line up naturally without the necessity of charge transfer between electrode and insulator, hence the lack of band bending and space-charge within the insulator, together with the flatness of the conduction band up to the interface.

For initial voltage bias, the electrode can supply sufficient current to balance that flowing in the insulator; the field in the insulator is constant, therefore the conduction process is ohmic at this stage. After reaching an internal field $F = v/4\mu$ (where v is the thermal velocity of the carriers and μ their mobility), the current that the cathode can supply becomes limited to the saturated thermionic current over the barrier and the conduction process loses its ohmic nature.

Actually, because of image forces interacting with the electric field at the cathode-insulator interface, the saturated thermionic current increases as a function of $F^{1/2}$. This will be important in defining the Richardson-Schottky effect.

A *blocking contact* occurs when $\psi_{\mathrm{m}} > \psi_{\mathrm{i}}$ (see figure 3.3c). In this case electrons flow from the insulator into the metal to reach thermal equilibrium conditions, giving rise to a space-charge region of positive charge, called *depletion region*; an equal negative charge resides on the metal electrode. The electrostatic interaction between the oppositely charged regions results in a local field within the surface of the insulator, causing the bottom of the conduction band to bend downwards until the Fermi level within the bulk of the insulator lies ψ_{i} below the vacuum level.

The free electron density at the interface is much lower than in the bulk of the insulator, therefore the rate of flow of electrons through the system will be limited by the rate at which they overcome the interfacial barrier. Thus, this conduction mechanism is electrode-limited.

The depth of the depletion region, λ, is estimated by noting that the depletion region has a much lower electron density than the bulk of the insulator and therefore a much lower conductivity; this means that any voltage applied to the system can be assumed, to a good approximation, to be absorbed entirely across the depletion region itself. When a negative bias V is applied to the metal and assuming a donor density of N_{d} inside the insulator, the depth of the depletion region and the field at the interface are, respectively,[36]

$$\lambda = \left(\frac{2(\psi_{\mathrm{m}}-\psi_{\mathrm{i}}+eV)K\varepsilon_0}{N_{\mathrm{d}}e^2}\right)^{1/2}, \tag{3.9}$$

$$F_0 = -\left(\frac{2N_{\mathrm{d}}(\psi_{\mathrm{m}}-\psi_{\mathrm{i}}+eV)}{K\varepsilon_0}\right)^{1/2}. \tag{3.10}$$

3.2.2 Metal-insulator-metal systems

As regards M-I-M systems, where the insulator has a finite thickness L, the space-charge regions can be overlapped. This can happen when the insulator is a very thin film or when the charge in the space-charge regions is insufficient to effectively screen the interior from the conditions at the interfaces. If this is the case, the bottom of the insulator conduction band is bent throughout its length and an electric field exists at all points within the insulator.

When two ohmic contacts are presented at the interfaces, overlapping accumulation regions are required to observe good space-charge limited conduction processes. If the thickness is larger than the two accumulation regions, instead, the conduction process reflects the intrinsic properties of the insulator.

If the depletion regions overlap when two blocking contacts are at the interfaces, then the bottom of the conduction band is always greater than $\psi_\mathrm{i} - \chi$ above the Fermi level, instead of attaining its equilibrium position at $\psi_\mathrm{i} - \chi$; the conduction process is normally electrode limited in this system.

It is important to note that we have assumed the barrier height at the metal-insulator interface to be $\psi_\mathrm{i} - \chi$, but if surface states exist on the insulator surface, this is not necessarily true. In fact, if the surface density is high (about 10^{13} $\mathrm{cm}^{-3}\mathrm{eV}^{-1}$), the interfacial barrier height is virtually independent of the electrode material.[37] These states existence is due in part to the sudden departure from periodicity of the potential at the surface and in part to the chemical nature of the surface, *i.e.* to the film preparation. It is normally not possible to determine *a priori* if surface states will exhibit a dominant role in the determination of the interfacial barrier height and thus we will assign the parameter ϕ to it.

3.2.3 Electrode-limited conduction processes

Accordingly to [36], the electron current density flowing through the M-I-M system is

$$J = 4\pi \frac{em}{h^3} \int_0^\infty \mathrm{d}E \Big(f_\mathrm{c}(E) - f_\mathrm{a}(E) \Big) \int_0^E P(E_x) \mathrm{d}E_x \tag{3.11}$$

where e, h and m are the elementary charge, the Planck's constant and the free elecron mass in each of the three regions respectively;

$$f_\mathrm{c} = \Big[1 + \exp\Big(\frac{E - E_\mathrm{f}}{kT} \Big) \Big]^{-1} \quad \text{and} \quad f_\mathrm{a} = \Big[1 + \exp\Big(\frac{E + eV - E_\mathrm{f}}{kT} \Big) \Big]^{-1} \tag{3.12}$$

are the electron distributions in the cathode and anode electrodes respectively, then E_f is the Fermi energy, V the voltage difference between the cathode and anode, E and E_x the energy and the x-directed energy of the electron and finally $P(E_x)$ the electron transmission probability through the insulator. The parabolic electron energy-momentum relation is assumed in the equation.

If the insulator is sufficiently thin (less than 50 Å), the predominant contribution to the current derives from electrons tunneling from the cathode through the insulator potential barrier, while for thicker films and higher temperatures the current is due to electrons thermally excited over the insulator potential barrier.

Fowler-Nordheim tunneling

To evaluate $P(E_x)$ in equation 3.11 it is normal to use the WKB (Wentzel-Kramers-Brillouin) approximation, a method for finding approximate solutions to linear differential equations with

coefficients that vary in space. Gundlach and Simmons in 1969 have studied the transmission probability through a potential barrier using both an exact method and the WKB tunnel probability and they have shown that the two results, under some conditions, have essentially the same functional form, but different numerical value form. As a result they have stressed the importance of functional rather than direct correlation of experimental and theoretical data.

It can be shown that the simplest generalized formulation connecting the tunnel current $J(V,T)$ at temperature T to $J(V,0)$ at 0 K is given by

$$\frac{J(V,T)}{J(V,0)} = \frac{\pi\alpha kT/2\bar{\phi}^{1/2}}{\sin(\pi\alpha kT/2\bar{\phi}^{1/2})} \tag{3.13}$$

where

$$J(V,0) = \left(\frac{e}{2\pi}h(\Delta s)^2\right)\left(\bar{\phi}\exp\left(-\alpha\bar{\phi}^{1/2}\right) - (\bar{\phi}+eV)\exp\{-\alpha(\bar{\phi}+eV)^{1/2}\}\right) \tag{3.14}$$

and $\alpha = 4\pi\Delta s(2m)^{1/2}/h$, Δs is the width of the potential barrier at the Fermi level of the cathode and $\bar{\phi}$ the mean barrier height above the Fermi level of the cathode. It follows that

$$\frac{J(V,T)}{J(V,0)} - 1 \propto \frac{(\Delta sT)^2}{\bar{\phi}} \ . \tag{3.15}$$

This slight quadratic dependence of the current on temperature (at $V = \text{const}$) is characteristic of the tunnel process.

Since the tunnel currents are only very slightly dependent on temperature, one may use $J(V,0)$ to describe the J-V characteristic at any reasonable temperature, in particular as an expeditious approximation to use when analysisng experimental data, because of its simpler functional form compared to $J(V,T)$.

At high voltages (*i.e.* for voltages much greater than the interfacial barrier height) the forward- and reverse-biased conditions are described by the Fowler-Nordheim formula:[22]

$$J_{\mathrm{F-N}} = AF^2\exp\left(-\frac{B}{F}\right) \tag{3.16}$$

where A is a constant that depends on the material, F is the electric field strength and

$$B = \frac{8\pi\sqrt{2m^*}\phi^{3/2}}{3eh} \tag{3.17}$$

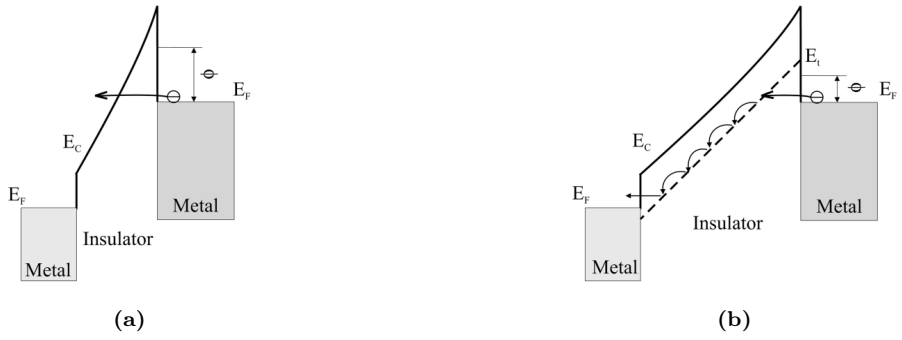

Figure 3.4: *Fowler-Nordheim tunneling, in (a) and (b) without and with shallow traps in the band gap, respectively (images from [22]).* φ_{b} *is the barrier height.*

with h the Plank's constant, m^* the electron effective mass in the insulator and ϕ the average potential barrier height.

According to equation 3.16, the current-voltage characteristics should be a straight line in $\ln(J/F^2)$ versus $1/F$ coordinates (*Fowler-Nordheim coordinates*) with a slope of B. An average interfacial barrier height ϕ can be derived, knowing the slope of a linear fit of the data in Fowler-Nordheim coordinates, from equation 3.17.

Although tunneling through a insulator of thickness greater than 50 Å is improbable, as pointed out in [22], this phenomenon can occur when shallow traps are present in the band gap. In this case an electron is tunneling to the trap level instead of tunneling to the conduction band and can flow through the insulator via hopping or tunneling process between traps. In this case, the barrier height ϕ obtained from equation 3.17 is the energy of traps E_t in the insulator band gap.

Richardson-Schottky emission

When the potential barrier is too thick to permit tunneling to occur, or at sufficiently high temperature, the current flowing through the insulator is limted mainly by the rate at which electrons are thermally excited over the interfacial potential barrier into the insulator conduction band. To determine the current flowing in the system, we set the lower limit in the integral over $\mathrm{d}E_x$ in equation 3.11 to be equal to the interfacial barrier height ϕ and the transmission function $P(E_x)$ to unity. Then, equation 3.11 integrates to the Richardson saturated thermionic emission equation,

$$J = \frac{4\pi me(kT)^2}{h^3} \exp\left(-\frac{\phi}{kT}\right) \ . \tag{3.18}$$

Electrons polarize the surface of the electrode from which they are ejected, causing ϕ to vary with the applied field because of attendant image forces (Schottky effect). Therefore the current does not saturate, but rather is a function of the applied field. Still, the Richardson equation holds only if the mean free path of the electron in the insulator is of the order of the insulator thickness,[36] otherwise the pre-exponential factor becomes $2e(2\pi mkT/h^2)^{3/2}\mu$, where μ is the carrier's mobility in the insulator. Assuming the mean free path of electrons in lithum niobate to be considerably lower than our films thickness, around 300 nm, and remembering the effect of image forces on the interfacial barrier height, the current-voltage characteristics obeys the following law:

$$J_{\mathrm{R-S}} = 2e\left(\frac{2\pi mkT}{h^2}\right)^{3/2} \mu F \exp\left(-\frac{\phi}{kT}\right) \exp\left(\frac{\beta F^{1/2}}{kT}\right) \tag{3.19}$$

that defines the Richardson-Schottky thermionic emission. The parameter β depends only on the dielectric permittivity of the insulator,

$$\beta = \sqrt{\frac{e^3}{\pi\varepsilon\varepsilon_0}} \tag{3.20}$$

The current-voltage characteristic in the case of Richardson-Schottky emission is a straight line in $\ln\left(J/FT^{3/2}\right)$ versus $F^{1/2}$ coordinates (*Simmons coordinates*) with a slope of β/kT and a linear fit in these ccoordinates permits to estimate the dielectric constant of the insulator through equation 3.20.

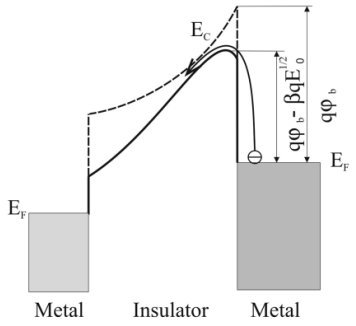

Figure 3.5: *Richardson-Schottky emission (from [22]). E_0 is the applied electric field and φ_b is the barrier height.*

3.2.4 Bulk-limited conduction processes

Poole-Frenkel emission

The Poole-Frenkel effect, or field-assisted thermal ionization, is the lowering of a Coulombic potential barrier when it interacts with an electric field. It is the bulk analogue of the Schottky effect at an interfacial barrier.

According to [36], the current-voltage characteristic in an insulator with shallow traps is described by

$$J_{\mathrm{P-F}} = J_0 \exp\left(\frac{\beta_{P-F} F^{1/2}}{kT}\right) \tag{3.21}$$

where $J_0 = \sigma_0 F$ is the low field current density, dependent on the low field conductivity σ_0, and $\beta_{\mathrm{P-F}}$ is the Poole-Frenkel coefficient, that depends only on the insulator dielectric constant ε and is given by

$$\beta_{\mathrm{P-F}} = \sqrt{\frac{e^3}{\pi\varepsilon\varepsilon_0}} \tag{3.22}$$

As can be seen by equation 3.21, current-voltage characteristic in this case must be linear in $\ln(J)$ versus $F^{1/2}$ coordinates (*Poole-Frenkel coordinates*) with a slope of $\beta_{\mathrm{P-F}}/kT$ and a linear fit in these coordinates permits to derive the dielectric constant of the insulator through equation 3.22. According to [38], also the trap concentration N_t can be estimated from the Poole-Frenkel coefficient as

$$N_\mathrm{t} = \left(\frac{e\sqrt{F_\mathrm{k}}}{\beta_{\mathrm{P-F}}}\right)^3 \tag{3.23}$$

being F_k the electric field corresponding to the beginning of a linear section of current-voltage characteristic in Poole-Frenkel coordinates.

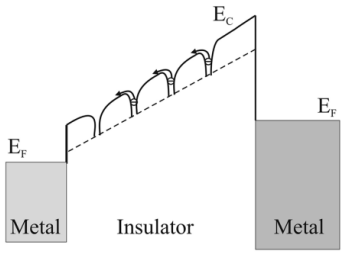

Figure 3.6: *Poole-Frenkel emission (from [22]).*

Space-charge limited currents

When ohmic contacts exist on the insulator and in particular when the two accumulation regions overlap, the conduction process is space-charge limited (SCL). Originally, Mott and Gurney derived in 1948 an equation for the current-voltage characteristic in the case of a *trap-free* insulator:[39]

$$J = \frac{9\mu K\varepsilon_0}{8d^3}V^2 \tag{3.24}$$

where μ is the charge mobility inside the insulator, K the electric permittivity of the insulator and d the film thickness. Nonetheless, equation 3.24 predicts much higher currents than are observed in practice and also does not show temperature dependence, which is also contrary to observation.

This is solved initially by Rose in 1955 by taking into account the presence of *shallow trap states* inside the insulator.[40] In this case, a large fraction of the injected space charge condenses therein, meaning that the free-carrier density is much lower than in a trap-free insulator. Moreover, the occupancy of traps is a function of temperature and therefore the SCL current is temperature dependent. The current-voltage characteristic in this case becomes

$$J = \frac{9\mu K\varepsilon_0\Theta}{8d^3}V^2 \tag{3.25}$$

where Θ is the ratio of free-to-trapped charge

$$\Theta = \frac{N_\mathrm{c}}{N_\mathrm{t}}\exp\left(-\frac{E_\mathrm{t}}{kT}\right) , \tag{3.26}$$

being N_t the shallow traps density inside the insulator, that are positioned at energy E_t below the conduction band, and N_c the electrons in conduction band. Note that equation 3.25 shows that including the effect of shallow traps does not change the dependence of the current on V^2.

In amorphous or polycrystalline structures, which are characteristic of thin film insulators, a distribution of trap levels is to be expected, rather than a discrete level of traps. The case of the *exponential trap distribution*, *i.e.* a distribution of trap levels that decreases expontentially with increasing energy below the conduction band, $N_\mathrm{t} \propto \exp(-E/kT_\mathrm{C})$ (E is the energy measured from the bottom of the conduction band and T_C is a characteristic temperature greater than the measurement temperature), has been treated again by Rose in 1955.[40] The current in this case is given by

$$J \propto V^{\left(\frac{T_\mathrm{C}}{T}+1\right)} \tag{3.27}$$

Lampert, in [41, 42], has noted that space-charge effects should be observed only when the injected free-carrier density (n_i) exceeds the bulk-generated free-carrier density (n_0). When $n_0 > n_\mathrm{i}$, the volume conductivity will predominate, hence the ohmic behaviour. The voltage V_X at which the transition from ohmic to SCL conduction occurs is

$$V_\mathrm{X} = \frac{en_0s^2}{\Theta K\varepsilon_0} . \tag{3.28}$$

When SCL current takes place, the current-voltage characteristic should be linear in $\ln(J)$ versus $\ln(V)$ coordinates (*double logarithm coordinates*). The slope can be: 1, if the voltage is below V_X; 2, in case of trap-free insulator or shallow trap levels; $\frac{T_\mathrm{C}}{T}+1$, in case of exponential trap distribution; other values can occur, for those cases in which the trap distribution differs from the exponential one.

Mott's hopping conduction

Thermally-assisted tunneling (hopping) between localized states is believed to play a major role in determining the conductivity of disordered materials at relatively low temperatures. According to [43], the conductivity is found to be $\sigma \propto \exp(F^2)$ at low fields and $\sigma \propto \exp\left(1/F^{1/4}\right)$ at high fields. The parameter that permits to distiguish between low- and high-field regimes is

$$\beta = \frac{eF}{2\alpha kT} \tag{3.29}$$

where F is, as usual, the electric field and $\alpha \equiv 1/a$ is the inverse of the size of the localized site a.

In the framework of Mott's model, temperature dependence of DC conductivity is described by

$$\sigma = \sigma_0(T) \exp\left(-\frac{A}{T^{1/4}}\right) \ , \tag{3.30}$$

with A and σ_0 both dependent on the localization length a and the density of electronic states $N(E_\mathrm{F})$; this holds only at low fields, at high fields the conductivity is insensitive to temperature instead. The weak temperature dependence of hopping conductivity follows from the fact that it is necessary to transfer enough energy from phonons to charge carriers to overcome the energy difference between initial and final states due to applied electric field.

According to Mott's model, if there is a spatial and energy distribution of sites near the Fermi level in the band gap of a material, an electron hops primarily between sites with the smallest energy difference and the shortest distance between them.

If defect centers are distributed in an insulator with high density near the Fermi level, the non-activated hopping conductivity mechanism follows the current-voltage characteristic

$$J = J_0 \exp\left\{-\left(\frac{F_0}{F}\right)^{1/4}\right\} \ . \tag{3.31}$$

Here F is the applied electric field, J_0 a field independent constant, F_0 the characteristic field which is given by

$$F_0 = \frac{16}{D(E)a^4 e} \ , \tag{3.32}$$

where $D(E)$ is an energy density of localized states near the Fermi level and a is again the localization length.[22] The current described by this model should be a straight line in $\ln(J)$ versus $V^{-1/4}$ coordinates (*high-field hopping coordinates*) with a slope $V_0^{1/4}$, being $V_0 = F_0 d$ the voltage related to the field F_0. The localization length a can be estimated from a linear fit of the measured currents in the high-field hopping coordinates through equation 3.32.

Chapter 4

Experimentals

4.1 Samples fabrication

4.1.1 Techniques involved in sample fabrication

Smart-Cut™ process

The Smart-Cut™ process is a technique used to transfer ultra-thin single crystal layers of wafer substrate material onto another surface and is based on ion implantation and wafer bonding.

This process presents some advantages compared to other film fabrication processes, mostly: thickness homogeneity and high flexibility for thicknesses, good crystalline quality on different kinds of substrates, possibility of transferring structured/patterned layers or even electronic devices and possibility of transferring doped films.[44]

In particular, the growth of $LiNbO_3$ films by traditional thin-film deposition techniques is difficult, maily because the stoichiometry of LN films and their crystalline quality is very sensitive to their growth conditions, which significantly influence the thin-film properties. Furthermore, Smart-Cut™ offers a viable solution to embed below the LN film a conductive metallic electrode, as requested by the present research project. The Smart-Cut™ process is, therefore, an attractive alternative to other LN thin film fabrication techniques.[45]

The Smart-Cut™ process starts from two wafers: wafer A, which is the single-crystal that has to be bound to the substrate, and wafer B, that works as a handle wafer, *i.e.* a stiffner substrate. The process basically comprises four main steps:

1. wafer A is implanted with suitably selected ions at appropriate dose (*e.g.* H^+, He^+, Ar^+ ions), which form a damage layer with microcavities underneath the surface; the depth of the implanted ions exhibits a Gaussian distribution and the peak density is determined by the ions energy;

2. wafer A is bonded to wafer B thanks to hydrophilic bonding layers deposited on the damaged wafer A surface and on the substrate;

3. the bonded pair is then annealed at a temperature above 200 °C, during which the microcavities grow and extend; if the implantation dose is high enough, those microcavities connect to each other leading to the splitting of wafer A in two parts; after this first annealing, another annealing at higher temperature can be performed to strengthen the chemical bonds;

4. the micro-roughness exhibited by the thin layer bonded to wafer B can finally be polished to obtain a flatter surface.

After step 3, the remaining part of the wafer A can still be sufficiently thick to be used again as wafer A, or even as wafer B if it suits the desgin of the final wafer.

Wafer bonding is the critical process that determines wether the thin film can be successfully transferred onto the substrate. So far, hydrophilic bonding using a thin SiO_2 layer as the medium layer is usually adopted.[45]

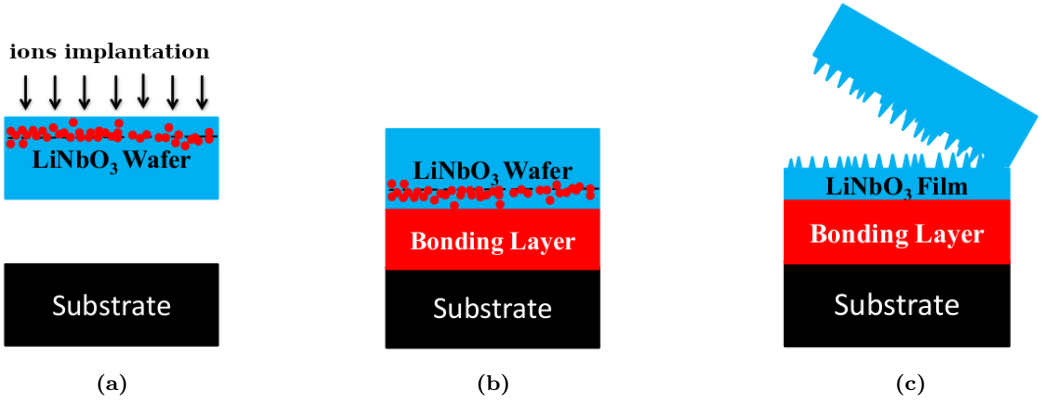

Figure 4.1: *graphical representation of the Smart-Cut™ process for the fabrication of a LN thin film on a generic substrate. (a): ions implantation; (b): wafer bonding; (c): splitting of the LN wafer after annealing. Images from [45].*

DC magnetron sputtering

Sputtering is a *Physical Vapour Deposition* (PVD) process based on the etching of a target through the action of a plasma. If the ions in the plasma can transfer enough momentum to the atoms in the target surface, the atoms of the target material are evaporated and emitted from the material itself. In their turn, if their mean free path is sufficiently low during the process, the etched atoms can be deposited onto an exposed surface of a substrate, placed at a distance from the target, facing it. In order to keep the evaporated atoms mean free path low, the sputtering process works inside a vacuum chamber. The plasma is typically generated by an inert gas, usually argon, which does not react with the target and the substrate. The thickness of the film obtained from this technique can be accurately controlled by adjusting flux or pressure of the gas injected in the chamber or simply the deposition time, giving generally consistent results.

During the deposition of a conducting material, the target and the supporting plate for the samples are used as cathode and anode respectively and when a constant voltage is applied between them, they are responsible for turning on the plasma. This particular case is called DC sputtering because of the direct current that flows through the plasma during the deposition.

Two main parameters have to be fixed in order to make the deposition process work: the pressures range inside the vacuum chamber and the electrical conditions. The lower limit for the pressure is given by the lower value needed to keep the plasma turned on; the upper limit is determined by the decrease of mean free path of the evaporated atoms with increasing pressures. Typical pressure values are in the order of 10^{-6} mbar, rised to about 10^{-3} mbar when the gas is entered the chamber. The electrical conditions are determined by the minimal threshold to turn on the plasma and by the fact that increasing the voltage between the electrodes produces a higher number of collisions between plasma ions, causing them to lose energy before hitting the target and therefore worsening the yield of the evaporation. Usually are applied voltages of some hundreds of volts.

To improve the deposition speed, the target can be immersed in a toroidal magnetic field. The

rotational symmetry axis of the field is perpendicular to the target surface, while its symmetry plane is placed just on the target surface. This permits the confinement of the plasma in a very narrow space close to the target, increasing the number of collisions between the ions and the target, thus increasing the number of evaporated atoms and decreasing the time needed to deposit the desired film thickness. This improved variant of the DC sputtering process is called *DC magnetron sputtering*.

Spin coating

Spin coating is a procedure that permits to apply a uniform thin film of an initially fluid resin to a flat substrate by spinning the substrate at high speed. The final film thickness will depend on the nature of the resin (viscosity, drying rate, percent solids, surface tension, etc.) and the parameters chosen for the spin process. The combination of spin speed and time generally defines the final film thickness. In general, higher spin speeds and longer spin times create thinner films.

The spin coating process consists of four distinct stages.[46]

1. *Dispense stage*: the resin fluid is deposited onto the substrate surface; the dispense can be static, which is when a small puddle of fluid is simply deposited near the center of the substrate, or dynamic, which is when the fluid is deposited while the substrate is already spinning at low speed; the dynamical dispense method is usually needed when the fluid or the substrate has poor wetting abilities, eliminating voids that may otherwise form in the final film.

2. *Substrate acceleration stage*: most of the fluid is expulsed from the substrate surface by the rotational motion; because of the initial depth of the fluid in the substrate surface, spiral vortices may be present during this stage; after the expulsion of the fluid excess, the fluid is evenly spread over the substrate surface with no thickness differences and the film is thin enough to be co-rotating with the substrate.

3. *Stage of constant spinning rate and fluid thinning behaviour is dominated by viscous forces*: it is characterized by gradual fluid thinning; the fluid thinning is generally quite uniform, but with solutions containing volatile solvents it is often possible to see a coating thickness difference around the rim of the substrate, depending mainly on rotation rate and surface tension and viscosity of the resin.

4. *Stage of constant spinning rate and fluid thinning behaviour is dominated by solvent evaporation*: the prior stage should reach a point where the viscosity effects yield only a minor net fluid flow; then, the evaporation of any volatile solvent species becomes the dominant process occuring in the spin coating; as these solvents are removed, the viscosity of the remaining solution will likely rise effectively freezing the coating in place.

After spinning is stopped, many applications require for the coating to be subjected to heat treatment.

4.1.2 Wafer design

All the prepared and studied samples come from a single wafer commercially produced by NANOLN. The wafer, of a diameter of 3 inches and global thickness of approximately 0.50 mm, has been produced using the patented ion-slicing process called Smart-Cut™ and is composed by a stack of the following layers, ordered from the top to the bottom of the wafer:

Material	Thickness	Notes
Fe:CLN	300 nm	The Fe-doped congruent LN thin film to be studied
Cr	30 nm	Adhesion layer between Fe:CLN thin film and bottom electrode
Pt	100 nm	Bottom electrode
Cr	10 nm	Adhesion layer between bottom electrode and insulating layer
SiO_2	2 µm	Insulating layer
LN	500 µm	Substrate

Table 4.1: *all the layers of the wafer structure, from top to bottom.*

The Fe:LN thin film is z-cut, with the $+z$ side of the material at the top of the wafer; thus, the spontaneous polarization $\vec{P}$ of the film is directed upwards. The iron concentration in the ferroelectric thin film is equal to 0.1 mol.%, corresponding to 1.89×10^{19} atoms/cm^3.

The Fe:LN wafer was a custom request and the manufacturer has not been able to provide an uniform quality of the crystalline film, which exhibited evident fabrication defects, such as holes of different sizes (see for example figure 4.2). The film nominal thickness of 300 nm was itself unhomogeneous. The thickness was measured approximately between 280 and 320 nm by the manufacturer.

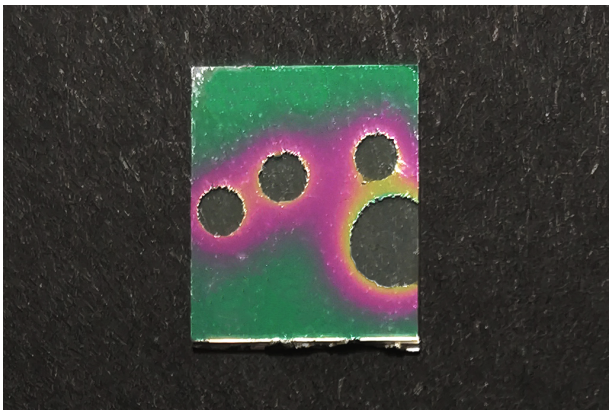

Figure 4.2: *holes in the Fe:LN crystalline film of sample 9.3.*

4.1.3 Electrodes choice

As anticipated at the beginning of section 3.2, well defined electrical contacts have to be made in order to study the electrical and photogalvanic properties of Fe:LN thin films.

We already specified in table 4.1 that the platinum layer takes the role of bottom electrode. Three different materials have been chosen instead as top electrodes: aluminium; PEDOT:PSS, a conductive transparent polymer; indium tin oxide (ITO), a conductive transparent oxide. Performing experiments on samples with electrodes of different materials, which have different characteristics and iteract differently with the ferroelectric film, will allow to analyse the behaviour of the iron doped lithium niobate in different potentially applicative scenarios.

Aluminium

Being a metal, aluminium almost completely reflects light in the visible wavelengths range, even for the small thicknesses measured in our depositions. Therefore, it is useful for studying the electrical properties of the ferroelectric film only in dark conditions. The choice of aluminium among other metals is due to better adhesion onto the LN film surface, eliminating the neccessity of an adhesion layer, which is needed for example when a gold electrode has to be deposited, and therefore simplifying the deposition process; furthermore, it can be easily deposited onto the LN surface through the DC magnetron sputtering process, for which it is usually readily available as a sputtering target.

PEDOT:PSS

PEDOT, poly(3,4-ethylenedioxythiophene), is a conductive polymer that can be combined with poly(styrene sulfonate), PSS, which acts as a charge counter balance to the oxidized PEDOT backbone during polymerization. The PEDOT:PSS complex can achive highly doped states, making it an efficient hole transporter. Moreover, by the addition of PSS a stable micro dispersion can be realized in water, making it an easy-to-process solution.[47]

As also shown in figure 4.3, PEDOT has a transmission window in the visible spectral range, making it useful in applications involving organic optoelectronic devices, such as thin film transistors, light emitting diodes, non linear optical devices and photovoltaic cells.[48]

An electrode made of an almost transparent material like PEDOT:PSS should be preferably used as a thin film to reduce light absorption to its minimum, allowing most of the radiation to reach the Fe:LN film. In this regard, PEDOT:PSS is a great candidate because it can be deposited by spin coating, which allows final electrode thicknesses down to fractions of micrometres.

Thanks to their high transmittance of visible light, PEDOT:PSS electrodes are very useful to study the electrical properties of the ferroelectric film both in dark and lit conditions.

The optical transmittance of PEDOT:PSS, deposited at three different spinning speeds (1500, 2500 and 4000 RPM; see table 4.3 for more details), has been measured with a Jasco V-670 spectrophotometer and is shown in figure 4.3.

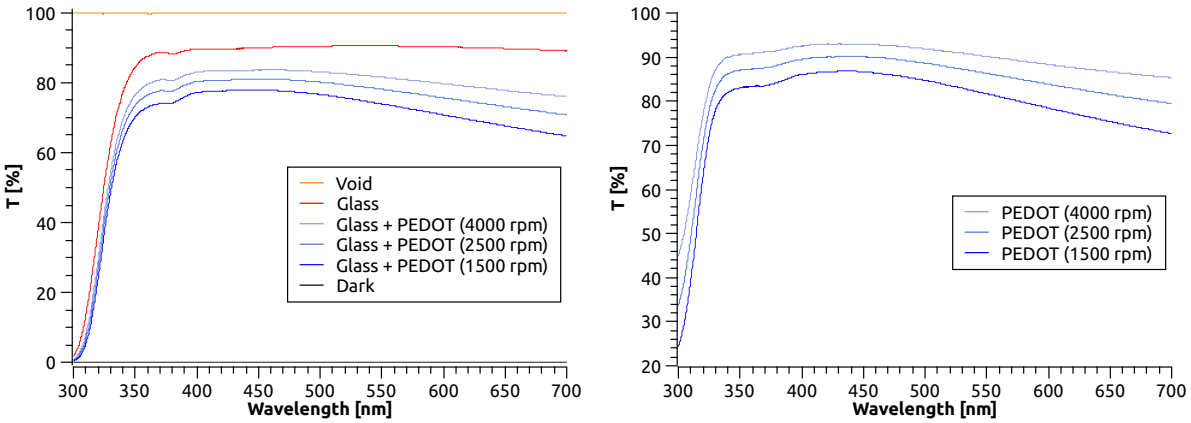

Figure 4.3: *optical transmittance of PEDOT:PSS thin films for three different top spinning speeds, in (a) with the glass where they were deposited, in (b) without the glass and computed by using equation 4.1; see table 4.3 for details on the spin coating recipes.*

As can be seen in figure 4.3, the optical transmittance of PEDOT:PSS in the range of interest for this work (400 to 550 nm) is between 80 and 90 % for any considered deposition thicknesses.

The three different films were deposited onto the surface of some piaces of glass, which were properly cut into $\sim 25 \times 25$ mm^2 squared pieces from microscope slides with the help of a CNC dicing/cutting saw from MTI.

Since the measure of the transmittance obtained by placing a deposited piece of glass into the spectrophotometer is actually a measure of the total transmittance of PEDOT:PSS film and glass one after the other, $T_{\text{glass+film}}$, the optical transmittance of each film alone was obtained as

$$T_{\text{film}} = \frac{T_{\text{glass+film}}}{T_{\text{glass}}} \tag{4.1}$$

having also measured the optical transmittance of a clean piece, T_{glass}, as reference.

The measures for the baseline and dark curves were automatically used by the acquisition software to normalize the optical trasmission data.

ITO

Indium tin oxide exhibits good light transmission characteristics in the visible region of the spectrum, as can be seen also in figure 4.4, while maintaining high electrical conductivity. This unique combination of properties makes ITO useful in a variety of applications, similar to those of interest for PEDOT:PSS, but in particular in liquid crystal flat panel displays and in solar cells.[49]

Again, in order to reduce at its minimum the light absorption by the eletrode, ITO has to be used preferably as a thin film. This is possible thanks to its availability as a sputtering target, allowing very thin and controlled depositions of the material by DC magnetron sputtering. ITO is also found to stick very well onto the surface of our samples.

Thanks to their high transmittance of visible light, ITO electrodes are very useful to study the electrical properties of the ferroelectric film both in dark and lit conditions.

The optical transmittance of ITO (deposition *D2790*, see table 4.2 for details on the parameters) has also been measured with the same procedure used for the analysis of PEDOT:PSS and is shown in figure 4.4.

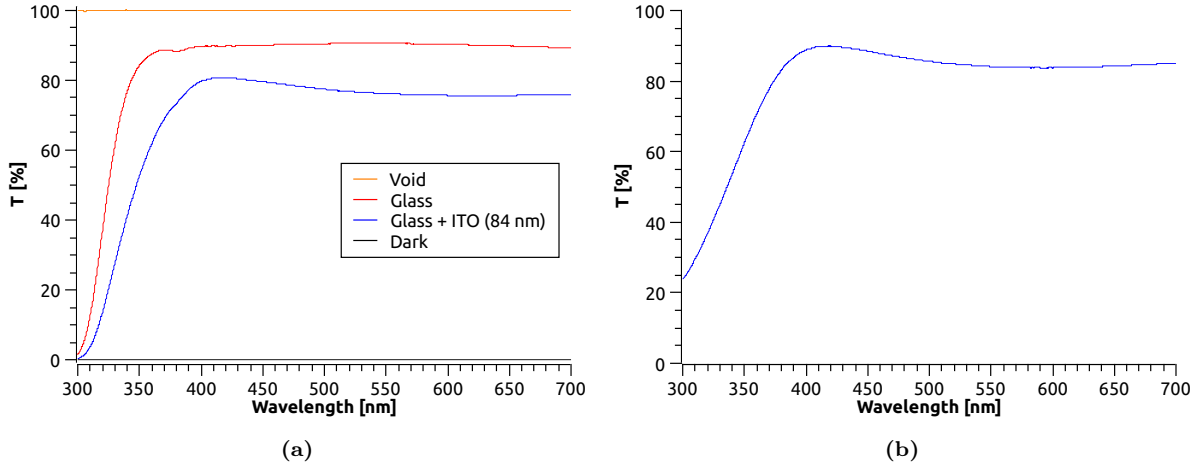

Figure 4.4: *optical transmittance of an 84 nm ITO thin film, deposition number* D2790*, in (a) with the glass where it was deposited, in (b) without the glass and computed by using equation 4.1; see table 4.2 for details on the sputtring parameters.*

4.1.4 Samples preparation

The samples preparation was performed in five steps: dicing of the Fe:LN Smart-Cut™ wafer, cleaning of the diced samples, masking, deposition of the electrodes and application of silver paste on the bottom and side.

The wafer was diced into several 10×12 mm^2 samples using a precision CNC dicing/cutting saw from MTI. The size of the samples was constrained by the size and shape of the measurement apparatus, that will be described later. The samples were cut with the 12 mm side perpendicular to the y-axis of the Fe:LN crystalline film, following the conventional flat indicators in the wafer.

Then, the diced samples surfaces have been cleaned following four steps: manual cleaning with distilled water and soap; ultrasonic cleaning firstly with acetone, then with ethanol and lastly with isopropyl alcohol. For each step, of the duration of 10 minutes, the ultrasonic cleaning was done with the samples bathing in the solvent inside a becker, which was in its turn floating in the water of the ultrasonic cleaner. This is a quite standard cleaning procedure for hard materials that need to be polished without being scratched. Each step is meant to remove the traces left from the precedent one.

Once the samples were cleaned, the electrodes positioning pattern was designed carefully for each different sample to avoid some evident defects in the film.

The opaque electrodes (Al) were designed as circles with a diameter of 2 mm, while the transparent ones (PEDOT:PSS, ITO) were designed with a door-lock shape, *i.e.* as the union of a circular part (diamenter 2 mm) and a rectangular part (2×1 mm^2). The door-lock shape could allow in possible future experiments to connect permanently a wire to the rectangular portion of the electrode using a conductive silver paste, while leaving its circular portion exposed to the light.

For each sample, the electrode mask has been cut into a piece of Kapton tape using a cutting plotter, that was then applied on the surface of the sample. In some cases (*e.g.* for spin coating deposition processes) we found useful to seal completely the sample into a Kapton envelope by adding a second piece of Kapton on the sample back. In this way, droplets of conductive polymer are prevented from creating unwanted short-circuits between the electrodes and the Pt film.

The use of Kapton was preferred among other materials mainly for its stability in a wide range of temperatures and for its characteristic of not polluting very much the high-vacuum needed for the sputtering process.

The deposition on the samples of the electrodes was then performed by DC magnetron sputtering (Al, ITO) and by spin coating (PEDOT:PSS) (the samples with PEDOT:PSS electrodes were heat-treated for 1 hour at 70 °C), and afterwards the masks were removed from the samples.

The deposition parameters are specified for every sample in tables 4.2 and 4.3.

At this stage, the platinum bottom electrode has still to be reached from the outside. The measurement apparatus is designed to place the sample on a conductive base plate; thus, the bottom surface and one side of the sample are spread with some fluid silver paste (which contains some solvents that are left evaporate after the application) that creates an electrical contact with the platinum bottom electrode and makes it accessible to the conducting base plate of the apparatus.

The SiO_2 insulation layer below the bottom electrode is very important to prevent current from the substrate to get collected by the Pt electrode.

A graphical representation of the prepared samples is shown in table 4.4, where they are identified by the wafer id. number followed by the sample id. number, together with the electrodes material and deposition number. Each deposited electrode in every sample is then identified by

a capital letter. Therefore, we will refer to electrodes by calling a sequence composed by their wafer id., their sample id. and their own id.; *e.g.* we will call the electrode B in sample 10 from wafer 9 simply 9.10.B.

Note that touching the PEDOT:PSS electrodes many times with the metal tip during the measurements scratches their surface, damaging them and making it more difficut to create a good electrical contact with them. Therefore, at a certain point the samples 9.10 and 9.12 have been cleaned from the PEDOT:PSS film on the top and from the silver paste on the bottom and have been prepared again with PEDOT:PSS electrodes in the same place. For this reason, in table 4.4 the electrodes of those two samples have two names, the first one related to the first deposition *sc1* (electrodes 9.10.A, B, C, D and 9.12.A, B, C, D) and the second one related to the second deposition *sc2* (electrodes 9.10.E, F, G, H and 9.12.E, F, G, H).

Deposition	**Material**	**Chamber pressure** [$\times 10^{-6}$ mbar]	**Ar pressure** [$\times 10^{-4}$ mbar]	**Time** [min]	**Thickness** [nm]
D2678	Al	1.4	50	12	70
D2693	ITO	4.6	50	11	70
D2759	Al	3.2	50	15	100
D2790	ITO	3.4	50	13	84

Table 4.2: *main parameters for the sputtering depositions.*

Deposition	**Acceleration** [RPM/s]	**Speed 1** [RPM]	**Time 1** [s]	**Speed 2** [RPM]	**Time 2** [s]
sc1	100	800	30	4000	30
sc2	100	800	30	1500	30

Table 4.3: *spin coating deposition recipes.*

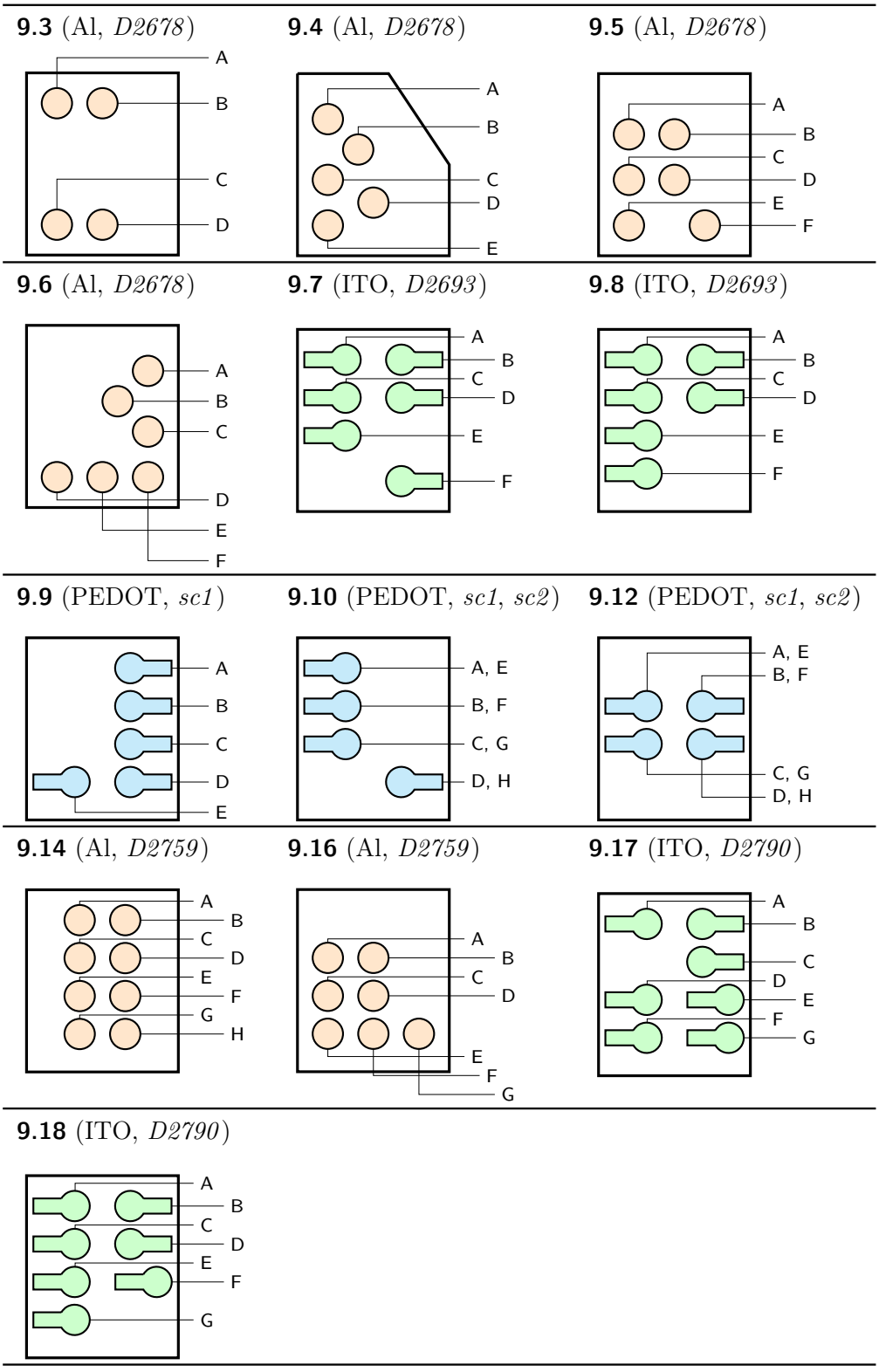

Table 4.4: *graphic representation of all the prepared samples with sample name, electrode material and deposition number.*

4.2 Experimental setup

4.2.1 Apparatus

All the electrical measures are meant to be taken with the samples inside an open vacuum chamber. The chamber is properly equipped with a sample positioning system and a system allowing for electrical contacts on the sample and it is fixed to an optical table.

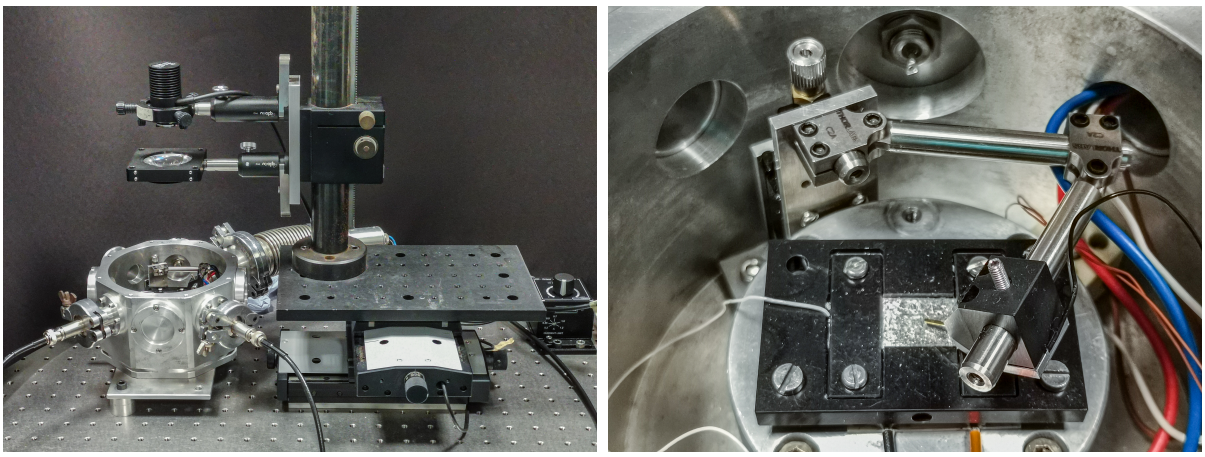

(a) **(b)**

Figure 4.5: *(a) a photograph of the experimental apparatus: measurement chamber in the bottom left, with BNC cables connected to it; LED and lens above it; structure for the optical system on the right side. (b) a photograph of the interior of the measurement chamber, with the sample placer and the metal tip with its holder.*

The sample placer is composed of a conducting base plate slightly larger than 10×12 mm^2, needed to make the electrical contact with the silver paste under the samples, with very small walls around to ease the placing of the samples and to keep them in place. A metal tip is held up by a metallic arm with x-y mobility and can be lowered through a screw mechanism down to the sample level, permitting to make an electrical contact with an electrode of the sample in the placer. The base plate of the placer and the metal tip are connected with two wires to two separate BNC female connectors, installed on the enclosure of the chamber, pointing outwards. These two connectors are the interface that permits to access the top and bottom electrodes of the samples from outside the vacuum chamber. A photograph of the interior of the measurement chamber is shown in figure 4.5b.

Above the chamber is placed an optical system composed by a high power LED, pointing down towards the sample base, and below it a lens, aimed at focusing most of the light emitted by the LED in a small spot. Both the LED and the lens are mounted on a z-translation mount. This system is provided to adjust the z-position of the light source and therefore its distance from the sample. Changing the height of the optical system affects primarily the dimension of the light spot, decreasing its diameter by bringing the optical system closer to the sample base. This mechanism is then fixed to a base that permits a fine x-y position adjustment of the system. Finally, this whole structure is also fixed to the optical table and thus provides an easy and precise x-y-z positioning system for the light source, necessary for centering the focused light spot on the studied electrode. The experimental apparatus is shown in figure 4.5a.

4.2.2 LEDs

Two LEDs are at disposal to be used as light sources. They are the 530 and 405 nm mounted light emitting diodes from Thorlabs (M530L3 and M405L4, respectively), provided with already installed heatsink and cable to connect them to a LED driver. The LEDs are powered by a LEDD1B driver from Thorlabs allowing to set the LED intensity by djusting the current fed to the system. We performed a calibration of the light intensity as a function of the driver settings at the sample surface for a pre-set distance between LED and sample. The light intensity for the LEDs are taken with a PM16-120 power meter from Thorlabs.

The electrical measurements under illumination are meant to be taken with the optical system all the way down to its lowest allowed position, with measured distances of $d_{\mathrm{S-lens}} = 8.0$ cm between the sample surface and the lens holder's bottom and $d_{\mathrm{S-LED}} = 12.5$ cm between the sample surface and the LED (summarized in figure 4.7). Therefore, the same distances were recreated from the power meter detector to the LED when measuring the light intensities. The obtained curves for the irradiance are presented in figures 4.6a and 4.6b. To the measured irradiances are associated a 3 % uncertainty, that is mainly due to the position of the light source at the right distance from the detector.

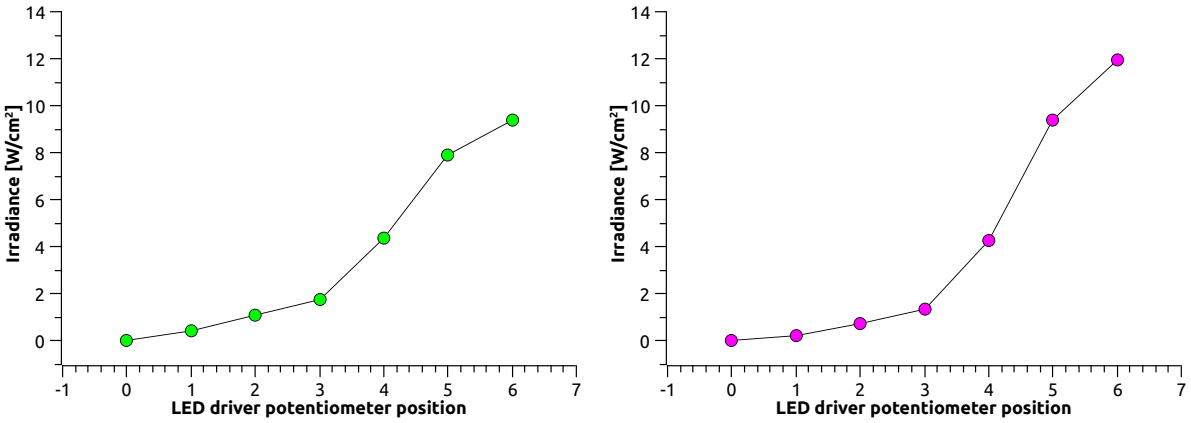

(a) (b)

Figure 4.6: *measured irradiance for the (a) 530 nm and (b) 405 nm LEDs from Thorlabs, taken at a distance* $d_{\mathrm{S-LED}} = 12.5$ cm *from the LEDs.*

4.2.3 Instruments

In order to take current-voltage characteristic curves, we used a 2612A source-meter unit from Keithley. As the name suggests, a source meter combines source and measurement capabilities in a single instrument, removing some difficulties related mainly to the synchronization of measurement and voltage application. According to its reference manual, the instrument allows to set the *acquisition time* choosing between 0.001 and 25 power line cycles (PLC) depending on the accuracy needed for the measure, corresponding to a range going from 20 µs to 500 ms when the power line has a frequency of 50 Hz. The default setting is 1 PLC, which equals 20 ms.[50]

The instrument provides some internal measurement scripts that permit the user to define particular voltage or current ramps and to access the obtained measures data from USB interface. One script in particular was used for measuring the current at a number of equidistant voltage steps going from a starting voltage to an ending one. The script asks also to set a parameter called *settling time*, corresponding to the time to be waited by the instrument at a new applied voltage

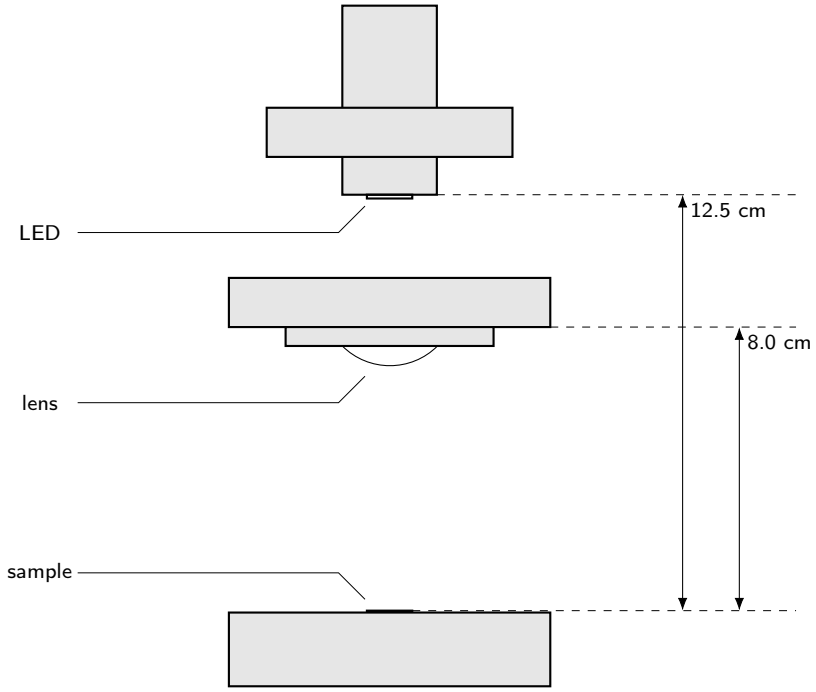

Figure 4.7: *details on the* $d_{\mathrm{S-LED}}$ *and* $d_{\mathrm{S-lens}}$ *distances.*

before taking the current measure. The settling time is very important when it is necessary to study the current at its steady state rather than in the first non-equilibrium instants.

The source meter also offers the possibility of being remotely controlled via computer, through a GPIB IEEE-488 connection. At this regard, a computer software called APRM, written and implemented by N. Argiolas and L. Bacci, provides basic scripting capabilities to set the parameters of three different measurement functions and to launch them through the software interface. The three implemented functions are:

- a triangle, starting at zero volts, reaching a peak voltage (that could be also negative) and coming back to 0 V again; the current is measured after each voltage step, whose amplitude can be set by the user;

- a double triangle, starting at zero volts, reaching a maximum (minimum) voltage, then ramping to a minimum (maximum) voltage and finally coming back to zero; the two triangles have opposite sign;

- a trapeze, working the same of the single triangle, but keeping the maximum voltage for a defined number of measurement points.

Following the instructions contained in the functions, the source meter is meant to be operative during the whole set of measures and to stop operating only when the function terminates all its voltage ramps. The settling time is included in the list of parameters to be set before launching the scripts via APRM.

Other instruments have been used in some occasions: the 3458A multimeter from HP, the HMF2550 Arbitrary Generator from Hameg, the DS7024 Digital Oscilloscope from Rigol and the IPS2303DD DC Power Supply from Iso-Tech.

4.3 Electrical characterization

Before starting with the actual measurements, all the electrodes should be connected to the multimeter for reading their electrical resistivity. Since the film to be studied is an insulator, we expect it to measure a high resistivity, ideally in the hundreds of MΩ or GΩ ranges and above.

Then, in order to study the electrical properties of the Fe:LN film, we decided to take current-voltage (I-V) characteristic curves with the source meter, both in dark and illuminated conditions.

We are interested on the following measures, which will be described in detail in chapter 5:

1. dark I-V characteristics, mainly with the purpose of modeling the charge transport in the Fe:LN heterostructures;

2. polarization-switching currents, where present, to estimate the spontaneous polarization and the coercive and residual fields of the film;

3. I-V characteristics under illumination, to estimate the photogalvanic current.

We observed that in general the I-V characteristic displays a transient response, due to several phenomena, that will be detailed in the following. On the other hand, in these measures the currents related to the switch of the ferroelectric polarization needs to be clearly discriminated from the current induced by electronic transport phenomena.

The dark and illuminated I-V characteristics requires the current to be measured on the steady state, therefore the settling time (defined as the time interval to be waited before the instrument starts the data acquisition) has to be set to some seconds. On the other hand, the poling currents, potentially together with after-poling relaxation currents, are definitely non-equilibrium currents and therefore have to be studied with a low settling time, for example in the range of ms.

We decided to perform the I-V characterization by applying a voltage at the sample ends that grows linearly by performing a set of discrete time steps. The current is measured for each step after the appropriate settling time has been elapsed. According to the voltage ramp sequence to be applied to the sample, different options are available: using the built-in functions of the source meter; by means of the home-made computer software interfaced with the source meter. In general, we use a sequence of triangular ramps, in which the applied voltage rises always from 0 V and back to this value.

It is observed (see figure 4.8) that launching a positive single-triangle ramp followed by a negative single-triangle ramp brings out an offset in zero, as high as tens of nA, probably due to the instrument operation being stopped at the end of a ramp; this means that in correspondence to the very first and very last measuring point the measured current is unaccurate. This is a big issue when the current close to 0 volts is needed to be precise enough to estimate the photogalvanic current and the photoconductivity. Therefore, in this case it is preferred to use double-triangle ramps. Eventually, the photogalvanic current has also to be compared to the current at 0 volts in dark conditions, thus all the I-V characteristics have to be measured by using double-triangle ramps when is needed to change the bias polarity.

Using the source meter in its manual operation mode, it is found that the samples can take up to 25 volts without incurring into dielectric breaks. A range going approximately from -20 to $+20$ V is an appropriate measure range. Notice that if 20 volts are applied to a 300 nm thin film, the film is immersed in an electric field of ~ 70 kV/mm, that is comparable to the values at which the electric breakdown usually happens (in [51] are reported values of 70-80 kV/mm). Thus, applying higher voltages than 20 V should be avoided unless it is done for a short amount

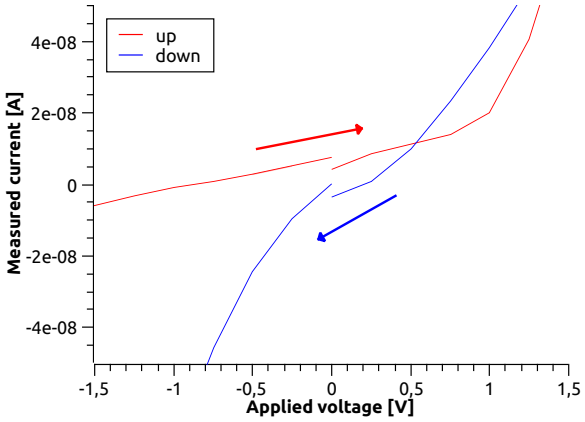

Figure 4.8: *appearance of an offset at 0 volts when single-triangle functions are used to perform the measurements. This particular I-V curve is taken for the 9.8.E ITO electrode illuminated by the 530 nm LED at full power, showing that the offset is too large to extract an accurate measure of the photogalvanic current.*

of time. It is reccomended anyway to limit the current to 100 mA inside the source meter to prevent potential dielectric breaks to compromise the instrument.

The positioning of the light source above the contacted electrode is very important when measuring the I-V curves under illumination to get results that are repeatable and comparable between different electrodes. Ideally, the focused light spot should be placed to ensure uniform illumination of the entire area of the electrode. Early measures, performed with the multimeter on a PEDOT:PSS electrode, show that the output current measured under constant illumination while moving the light spot around the electrode increases substantially as soon as the spot reaches a close proximity to the electrode area, saturating to a maximum value when the whole electrode is illuminated; the saturation current continues to be measured until the spot starts to leave the electrode area, eventually making the current decrease again when the spot moves away from it. The current remains at its maximum within 1 or 2 mm of displacement from the perfect centered alignment between spot and electrode and decreases less than the 5 % within the first 3 mm of displacement. Therefore, the positioning of the light spot can be performed without the study of the current as function of the spot's coordinates with the multimeter and this does not prevent the precision of the results.

During all the electrical measurements, the measurement-chamber has to be screened from the light sources in the room with black paperboard.

Finally, unless otherwise specified, the measure acquisition time is set to the instrument default value, 1 PLC (power line cycles) or 20 ms.

Chapter 5

Results and discussion

5.1 Preliminary study of the settling time

A preliminary study of the settling time was done with the aim of understanding the time needed for the system to be considered appriximately at steady state, which is the condition that has to be fulfilled when analysing the charge transport modeling.

The analysis has been performed for the 9.4.A aluminium electrode, taking I-V curves at different settling times in the range from 500 ms to 10 seconds. The results, shown in figure 5.1, have been proven to be repeatable and show that after some seconds the I-V curve stabilizes around what seems to be an equilibrium curve. The best compromise between accuracy and time needed to perform the whole measure is around 3.5 seconds. The time needed to reach the steady state is assumed to be mainly due to the Fe:LN film rather than to the electrodes, therefore the same value is considered also when studying ITO and PEDOT:PSS electrodes.

Note that all the electrical measurements presented in this work have been done by taking from 2 to 4 current measures per volt (voltage steps from 0.4 to 0.25 V). With the purpose of improve this study, it could be interesting to see if the time needed to reach the equilibrium current for a given applied voltage depends on the actual voltage jump between two consecutive measures. If it does, the actual parameter to be studied could be the voltage-increase (or -decrease) rate given by the amplitude of the entire range of applied voltages divided by the time needed to go from the first to the last voltage, $\Delta V/\Delta t$. A brief test was performed by applying to different electrodes a particular waveform, generated by the arbitrary function generator and appropriately amplified to reach the ± 20 V range; its current response was observed by connecting it to a load (a resistor) and reading its voltage with an oscilloscope (more details about the circuit used to perform the test are included in the appendices). The custom voltage signal represented 4 positive triangles followed by 4 negative triangles and its frequency was set to roughly match the voltage-increase ratio of the measures taken with the source meter. Such an input signal should be a good reproduction of the voltage ramps applied by the source meter in our experiments, but with much smaller voltage steps. The observed signal was a current-time representation of our I-V curves, suggesting that the voltage-increase ratio was a reliable parameter in replicating the I-V results on the oscilloscope.

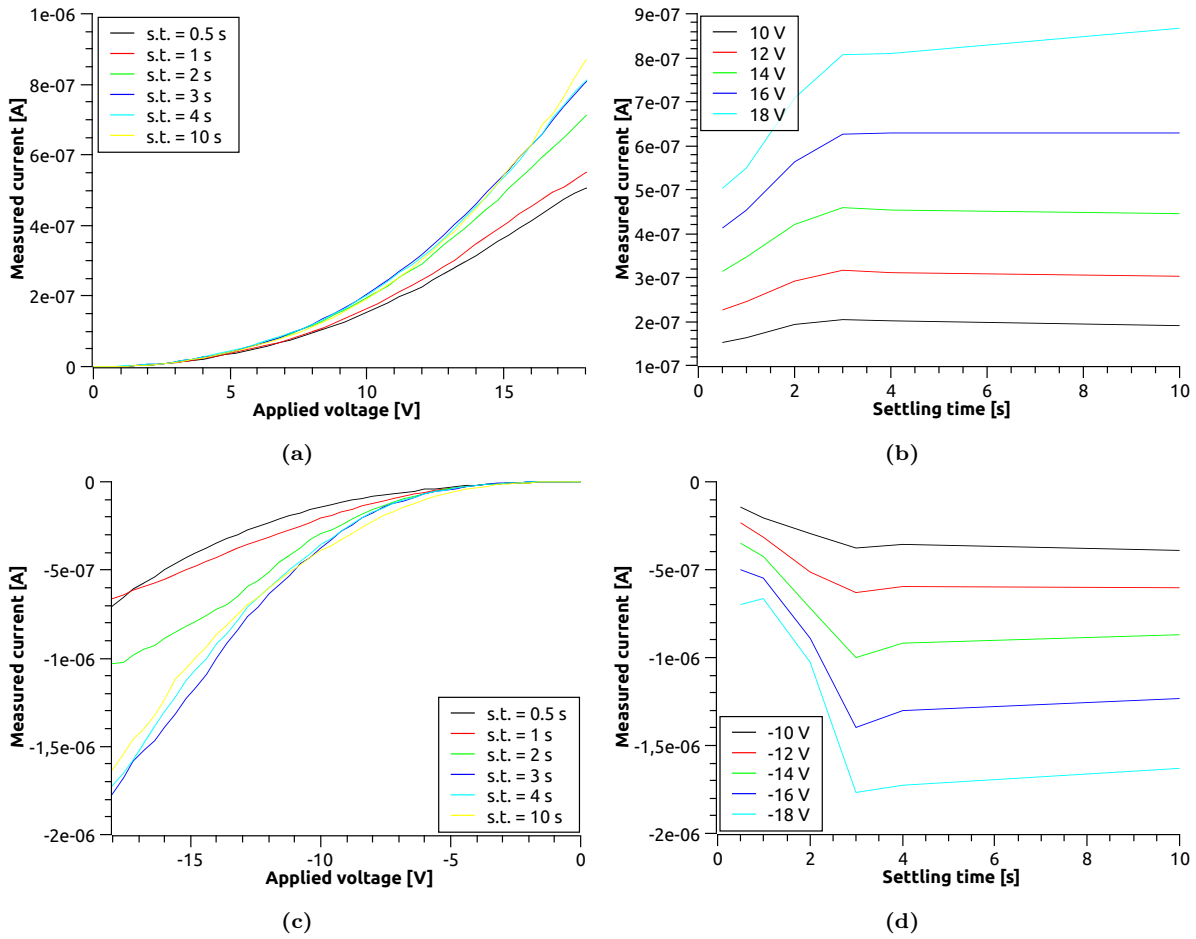

Figure 5.1: *in (a) and (c) are presented the I-V characteristics at different settling times (s.t.) in the case of positve and negative voltages, respectively; in (b) and (d) are presented instead the currents as function of the settling time, extracted from the I-V curves at different positive and negative voltages, respectively. The measurements have been performed on the 9.4.A Al electrode.*

5.2 Dark I-V characterization

The goal of this section is to understand the charge transport mechanism in our samples in the dark. This is done by studying the current-voltage characteristics measured in dark conditions.

A current-voltage characteristics is shown for each electrode material in figures 5.2, 5.3 and 5.4. The measuring sequence that produced these results was composed by two double triangles, a positive-negative one and a negative-positive one.

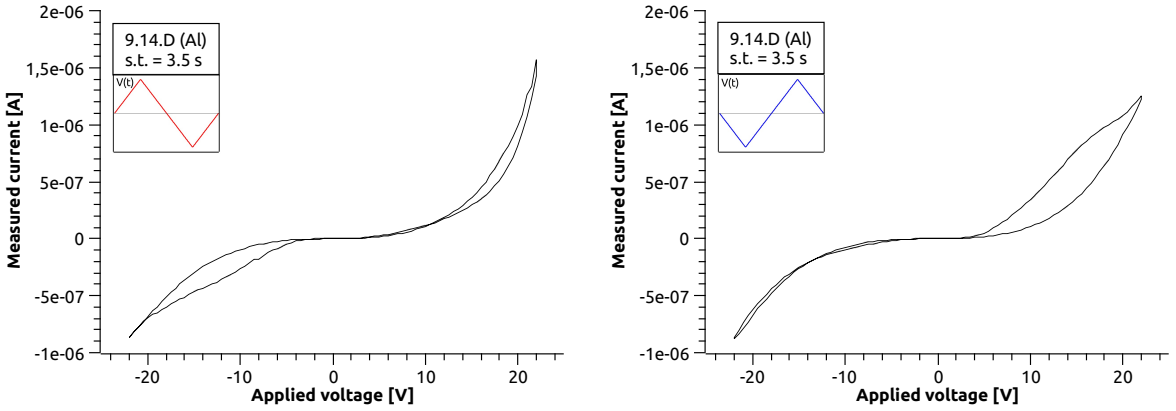

Figure 5.2: *typical I-V curves for Al electrodes at settling time s.t. = 3.5 seconds; in (a) and (b) are presented the results for the positive-negative double triangle and for the negative-positive double triangle, respectively.*

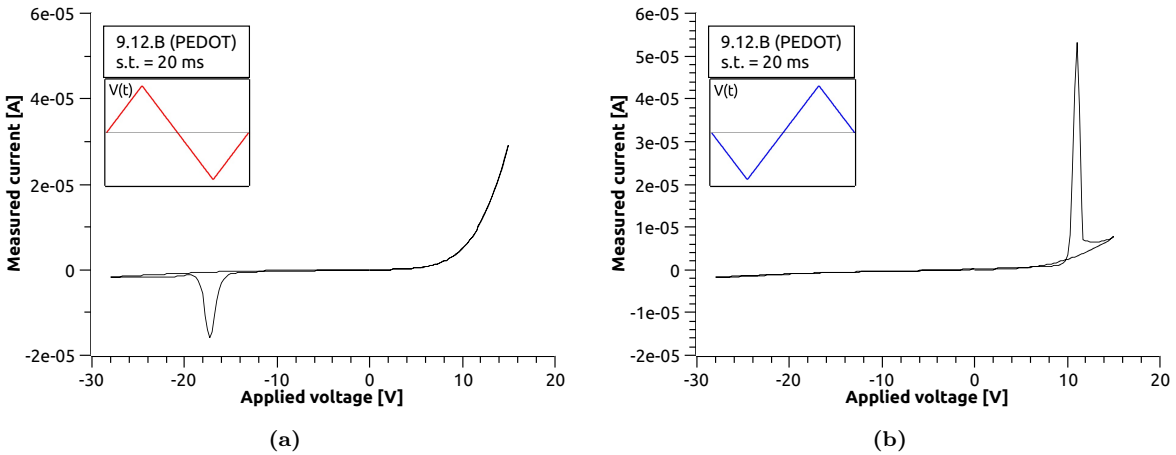

Figure 5.3: *typical I-V curves for PEDOT:PSS electrodes at settling time s.t. = 20 milliseconds; in (a) and (b) are presented the results for the positive-negative double triangle and for the negative-positive double triangle, respectively.*

Observing figures 5.2, 5.3 and 5.4, in some regions of the plots appears an evident hysteretical behaviour. The hysteresis, as shown for example in figure 5.5, disappears when measuring multiple I-V characteristics of the same polarity. Therefore we attribute this behaviour to be related to polarization switching phenomena. Since the objective of this section is the study of the conduction mechanisms in the material, we paid attention to consider into the analysis only the measures that are related to the electronic conduction.

The datasets that have been analysed are shown in figures 5.6, 5.7 and 5.8. The settling time was set to 3.5 seconds.

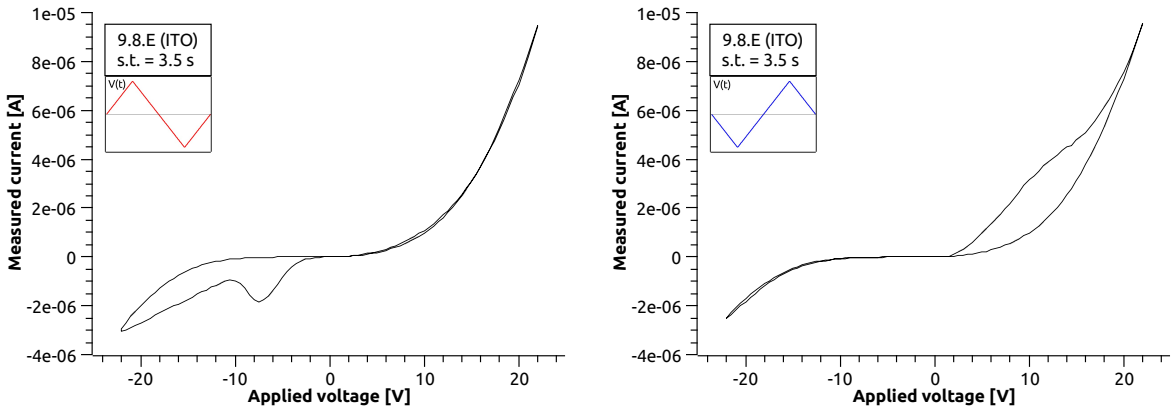

(a) (b)

Figure 5.4: *typical I-V curves for ITO electrodes at settling time s.t. = 3.5 seconds; in (a) and (b) are presented the results for the positive-negative double triangle and for the negative-positive double triangle, respectively.*

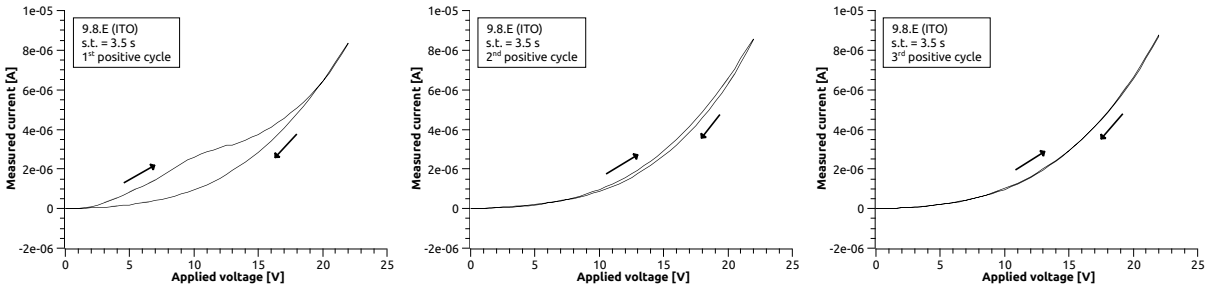

(a) (b) (c)

Figure 5.5: *hysteretical behaviour disappearing after measuring multiple I-V curves of the same polarity; the case of the 9.8.E electrode has been taken as an example.*

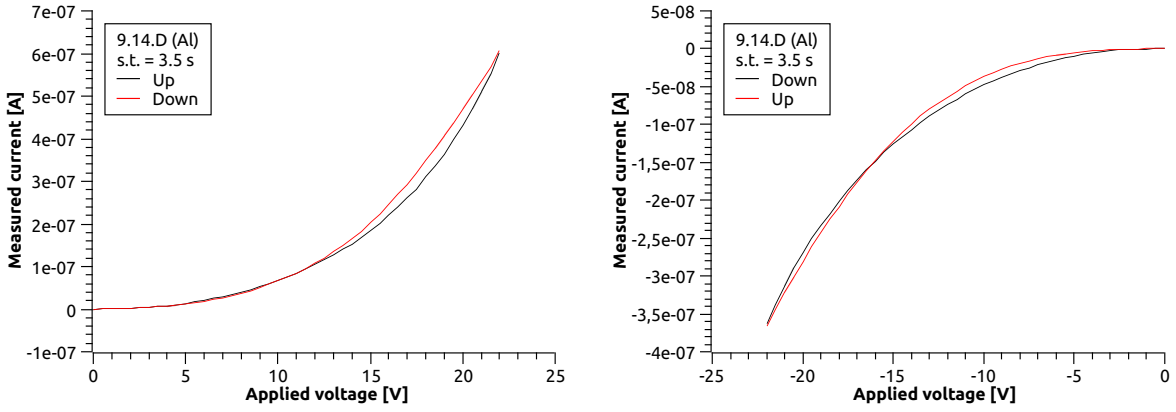

(a) (b)

Figure 5.6: *the I-V curves used for modeling the conduction in Cr/Fe:LN/Al heterostructures.*

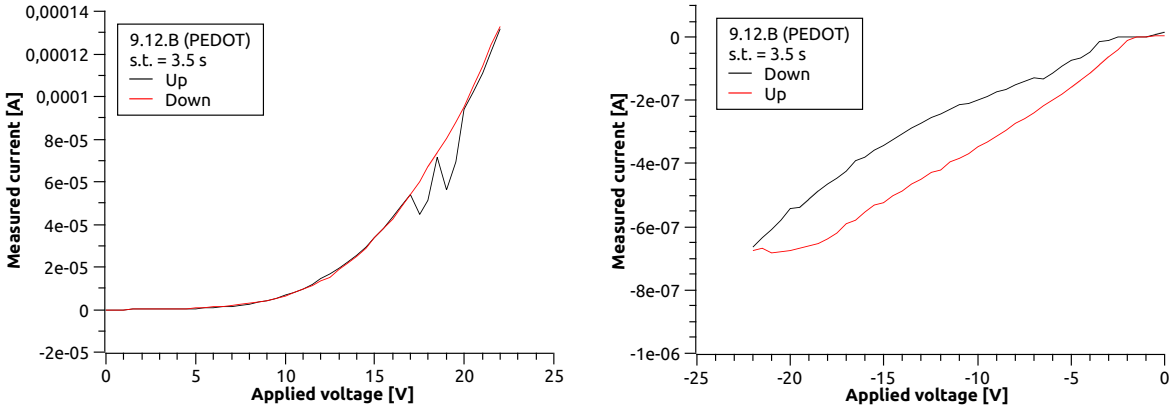

(a) (b)

Figure 5.7: *the I-V curves used for modeling the conduction in Cr/Fe:LN/PEDOT:PSS heterostructures.*

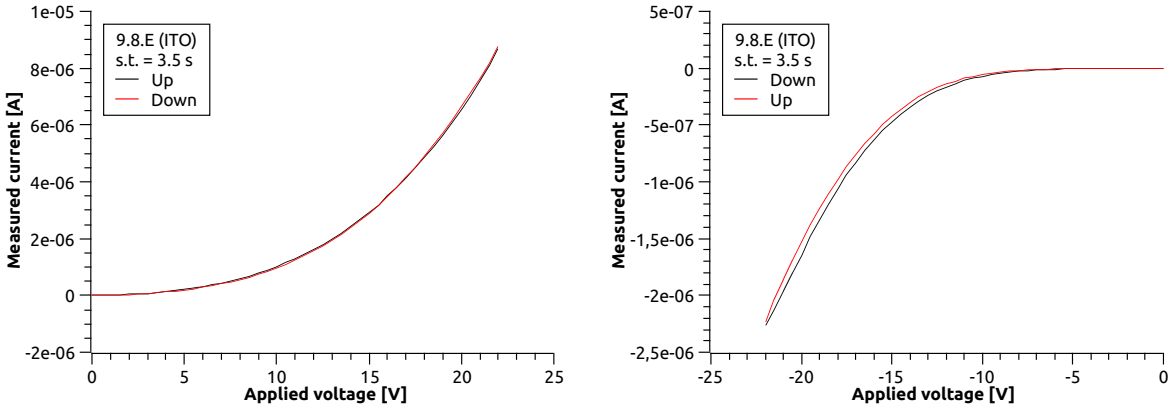

(a) (b)

Figure 5.8: *the I-V curves used for modeling the conduction in Cr/Fe:LN/ITO heterostructures.*

The conduction mechanisms in a metal-insulator-metal system, corresponding in first approximation to the heterostructures we are dealing with, can be electrode-limited or bulk-limited processes. As discussed in more detail in section 3.2, the Richardson-Schottky (R-S) and Fowler-Nordheim (F-N) models are the two main models that describe an electrode-limited conduction, while the Poole-Frenkel (P-F), Mott's hopping and space-charge-limited currents (SCLC) models describe a conduction that is limited by the bulk of the insulator.

In order to compare the measures with these models, the typical procedure consists in plotting the measured I-V curves in coordinates that are specifically defined to put in evidence the distinctive features of one or another type of conduction mechanism. If a curve is linear in the coordinates system of a particular model, it means that its functional dependence on the applied bias follows the one predicted by the model.

The I-V curves predicted by the different models, together with the coordinates systems that linearize them, are summarised in table 5.1.

Notice that all the mentioned models, apart from the SCLC one, derive actually an equation for the current density as a function of the applied electric field. In table 5.1 we present instead current-voltage relations. During the analysis we paid attention to respect the units of the slopes in the original current-field characteristics, described in section 3.2, taking into account the film thickness when needed.

Model	I-V characteristic	y	x
R-S	$I \propto V \exp\left(-\frac{\phi}{kT}\right) \exp\left(\frac{\beta_{\mathrm{R-S}} V^{1/2}}{kT}\right)$	$\ln(I/V)$	$V^{1/2}$
F-N	$I \propto V^2 \exp\left(-\frac{B}{V}\right)$	$\ln(I/V^2)$	$1/V$
P-F	$I \propto \exp\left(\frac{\beta_{\mathrm{P-F}} V^{1/2}}{kT}\right)$	$\ln(I)$	$V^{1/2}$
SCLC	$I \propto V^{\alpha}$	$\ln(I)$	$\ln(V)$
hopping	$I \propto \exp\left\{-\left(\frac{V_0}{V}\right)^{1/4}\right\}$	$\ln(I)$	$V^{-1/4}$

Table 5.1: *the I-V characteristics predicted by each considered model and the coordinates systems that linearize them.*

The hopping characteristic curve considered here refers to the high-fields regime.

The physical quantities that can be extracted from the slope σ of the linear interpolations are, according to the disscussion in section 3.2:

- for the R-S model, the dielectric constant: $\varepsilon_{\mathrm{R-S}} = \dfrac{e^3}{\sigma^2_{\mathrm{R-S}}(kT)^2\pi\varepsilon_0}$;
- for the F-N model, the height of the potential barrier: $\phi_{\mathrm{F-N}} = \left(\dfrac{3\sigma_{\mathrm{F-N}} eh}{8\pi\sqrt{2m^*}}\right)^{2/3}$;
- for the P-F model, the dielectric constant: $\varepsilon_{\mathrm{P-F}} = \dfrac{e^3}{\sigma^2_{\mathrm{P-F}}(kT)^2\pi\varepsilon_0}$;
- for the SCLC model, the exponent $\alpha = \sigma_{\mathrm{SCLC}}$;
- for the hopping model at high fields, the localization length $a_{\mathrm{hop}} = \left(\dfrac{16}{D(E)\sigma_{\mathrm{hop}} e}\right)^{1/4}$.

From the beginning of a linear region in Poole-Frenkel coordinates, E_{k} in units of V/m, the trap density in the insulator can also be estimated as $N_{\mathrm{t}} = \left(\dfrac{e\sqrt{E_{\mathrm{k}}}}{\beta_{\mathrm{P-F}}}\right)^3$.

Some notes about the analysis: (i) according to the theoretical discussion in the previous chapters, the SCLC model can fit only when two ohmic contacts are created at the interfaces, together with overlapping accumulation regions; none of the two conditions are satisfied, in particular there cannot be ohmic contacts at the interfaces, given that $\psi_{\mathrm{m}} > \psi_{\mathrm{Fe:LN}}$. Therefore, the SCLC model has not been considered in the present analysis; (ii) when computing the localization length, a_{hop}, from the slope of a linear fit in hopping coordinates, a value of $D(E) = 3.8 \times 10^{21}$ eV^{-1}cm^{-3} has been used for the energy density of states, having assumed that hopping occurs over iron defect centers, which are distributed with a concentration of $c_{\mathrm{Fe}} = 1.89 \times 10^{19}$ cm^{-3} in our samples and have energy density, according to [52], of $n_{\mathrm{Fe}} \sim 200$ eV^{-1}; (iii) the computation of the potential barrier height from the linear fits in Fowler-Nordheim coordinates is done by using the effective mass $m^* = 0.058\, m_e$, as reported in [53].

The analysis proceded by using a custom software written in Python that plots the measured I-V curves in the different coordinates and performs, when required, a linear interpolation of

the data. We paid attention to plot correctly the negative currents and the negative-voltage branches of the I-V curves.

To discuss the results that will be obtained from the data analysis, it is necessary to have an idea of the band diagram of the Fe:LN heterostructures we are dealing with. The parameters that compete to define the interaction between the thin film and the electrodes, which are needed to draw an ideal representation of the band diagrams, are presented in table 5.2. Note that also the work function of chromium is reported, because Cr is the metal actually touching the bottom face of the ferroelectric film and its work function is actually the one responsible for the interfacial barrier height.

The band diagram of the heterostructures encountered in this work can be approximately estimated by using this method:

1. draw the band diagram at the two interfaces as if they were two separate contacts between a metallic/conductive electrode and an infinitely thick film;

2. at equilibrium, the Fermi energy must be the same within the heterostructure, otherwise the charge carriers would drift from one side to the other throughout the material according to the potential energy difference; therefore, bring the band diagrams of the two separate interfaces at a distance equal to the film thickness and align the Fermi energy of the electrode on the right side to the Fermi energy of the electrode on the left side, while keeping fixed the distances of the conduction and valence bands from the Fermi energy at the interface.

This is clearly an imprecise derivation, but it should be good enough given that we are treating only almost-symmetric diagrams.

In estimating the band diagrams of the three heterostructures (shown in figures 5.9 and 5.10), the Fe:LN film has been treated like an n-type doped semiconductor. Assuming that the iron sites in the film can be considered to be the donor centers, knowing their concentration and the LN dielectric constant along the c axis (28, according to [16, 26]) permits to estimate the depth of the depletion regions (equation 3.9 from 3.2), $\lambda = 19$ nm. Also, in estimating the band diagram of the Cr/Fe:LN/PEDOT:PSS heterostructure, the electrode has been treated like a highly-doped p-type semiconductor.

The Richardson-Schottky model could be appropriate to predict the charge transport mechanism: the blocking interfacial barrier, equal to 3.4 eV at the interfaces with Cr and ITO, 3.18 eV at the interfaces with Al and ~ 3.9 eV at the interfaces with PEDOT:PSS, is thicker than 50 Å; furthermore, the operating temperature of 300 K, together with the Schottky effect, could be enough to favour the thermionic emission over the tunneling through the barrier. Nonetheless,

Material	**Work function ψ**	**Other parameters**
Fe:LN	/	$\chi = 1.1$ eV,[35] $E_g = 3.9$ eV,[35] $E_F = 2.4$ eV[35]
Cr	4.5 eV[54]	
Pt	5.65 eV[54]	
Al	4.28 eV[54]	
PEDOT:PSS	/	$E_{LUMO} = 3.5$ eV,[55] $E_{HOMO} = 5.2$ eV[55]
ITO	4.5 eV[49]	

Table 5.2: *band structure parameters for electrodes and Fe:LN film; χ is the electron affinity, E_g the band gap energy, E_F the Fermi energy, E_{LUMO} the Lowest Unoccupied Molecular Orbital energy, E_{HOMO} the Highest Occupied Molecular Orbital energy.*

when the charge carriers overcome the interfacial barrier it is possible, being forced to hop between defect sites, that their mobility is too low within the film and eventually the current results bulk limited instead; in this case, the conduction could be well described by the Poole-Frenkel effect.

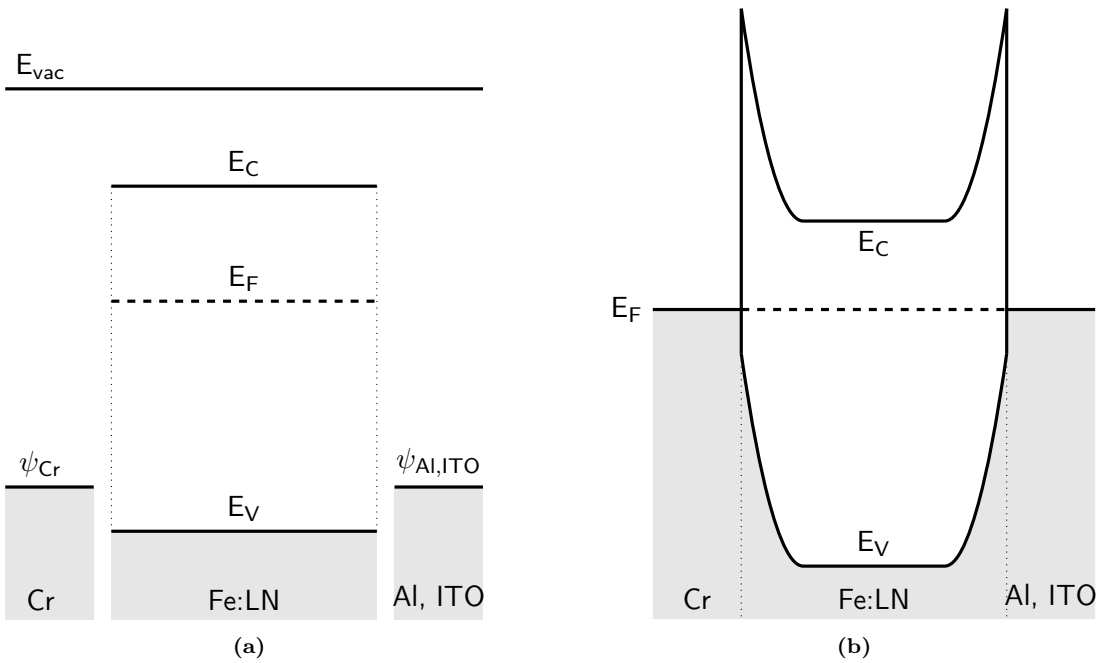

Figure 5.9: *(a) energy levels and (b) ideal representation of the energy band diagram for the Cr/Fe:LN/Al and Cr/Fe:LN/ITO heterostructures.*

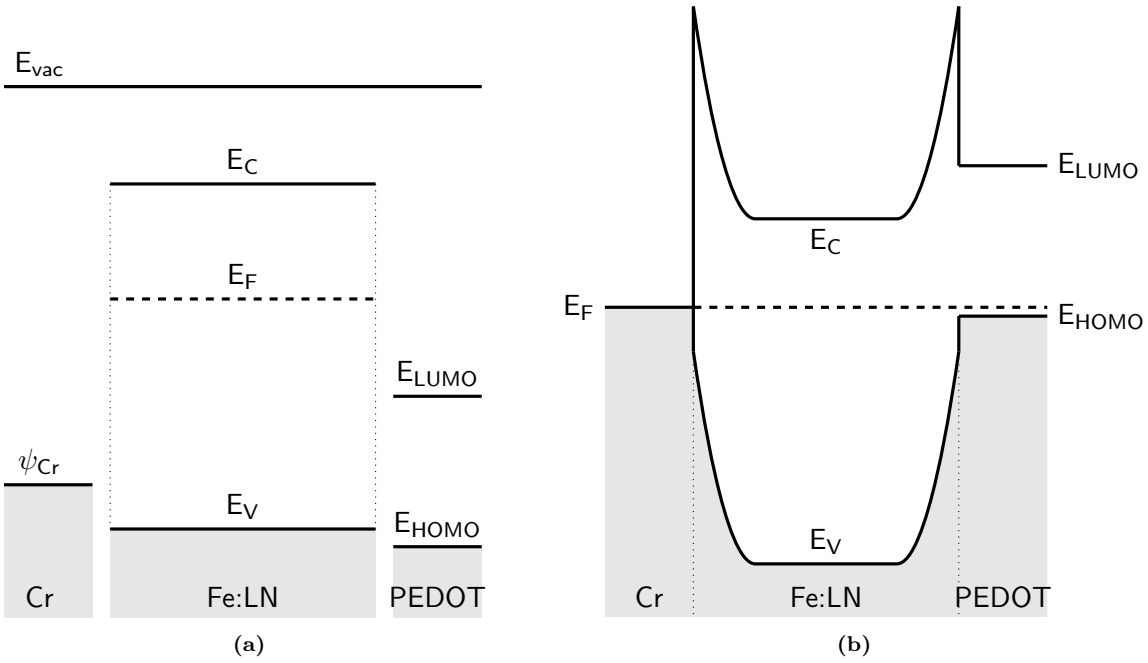

Figure 5.10: *(a) energy levels and (b) ideal representation of the energy band diagram for the Cr/Fe:LN/PEDOT:PSS heterostructure.*

In order to summarise more effectively the results of the analysis, each I-V curve have been divided by the software into four datasets:

- one for positive voltages, with the applied voltage increasing from 0 V to the maximum value (A in figure 5.11); we will refer to this dataset by writing $V > 0$, up;
- one still for positive voltages, but with decreasing applied voltage (B in figure 5.11), *i.e.* $V > 0$, down;
- one for negative voltages, with the applied voltage decreasing from 0 V to the minimum value (C in figure 5.11), *i.e.* $V < 0$, down;
- finally one for negative voltages, with the applied voltage increasing to 0 V (D in figure 5.11), *i.e.* $V < 0$, up.

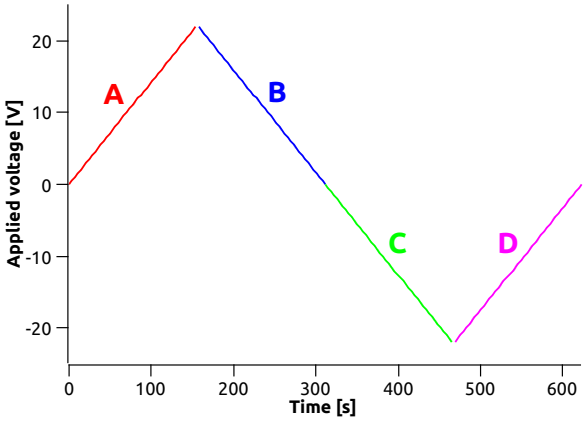

Figure 5.11: *the four different portions of the double-triangle ramps.*

The different datasets have been analysed separately, giving the following results.

Results for electrode 9.14.D (Al)

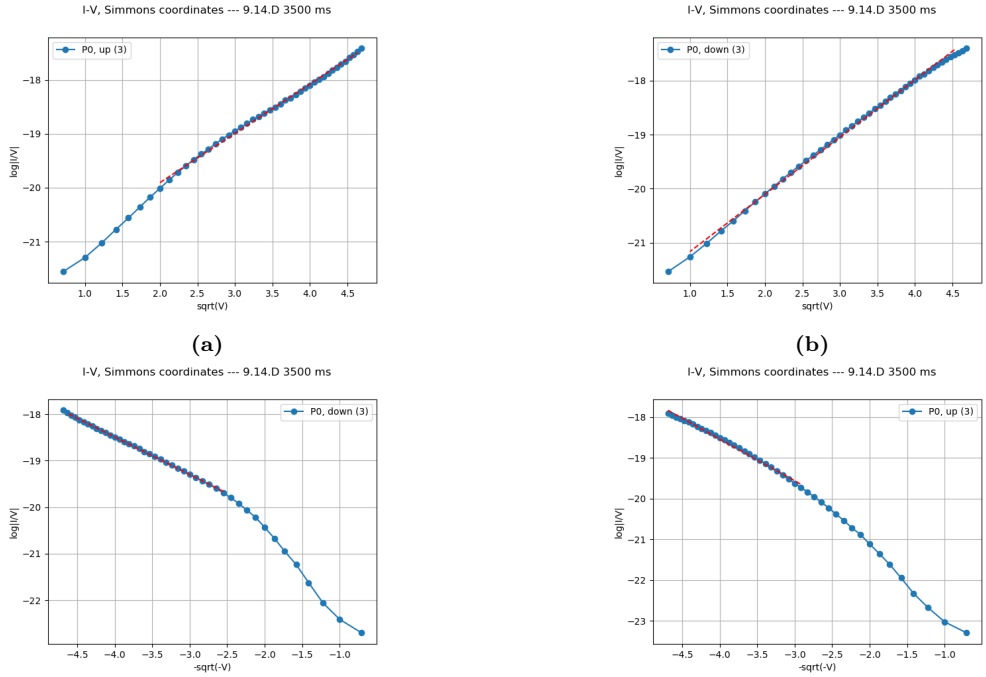

Figure 5.12: *linear fits (red dashed lines in the plots) for the 9.14.D electrode in* ***Simmons*** *coordinates. (a) and (b): $V > 0$, up and down, respectively; (c) and (d): $V < 0$, down and up, respectively.*

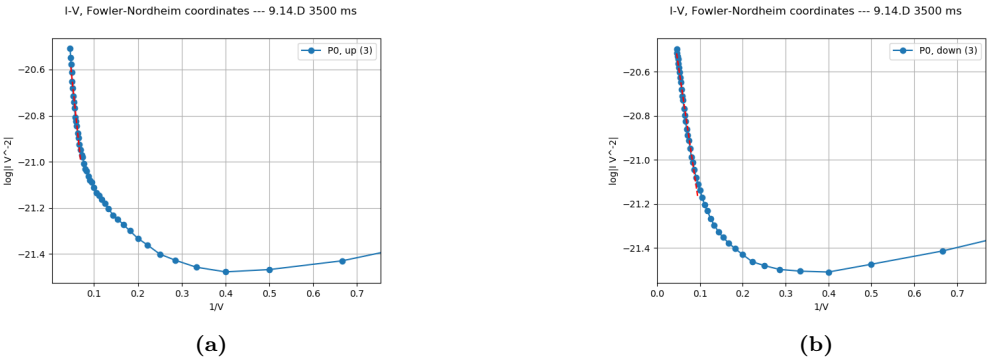

Figure 5.13: *linear fits (red dashed lines in the plots) for the 9.14.D electrode in* ***Fowler-Nordheim*** *coordinates. (a) and (b): $V > 0$, up and down, respectively.*

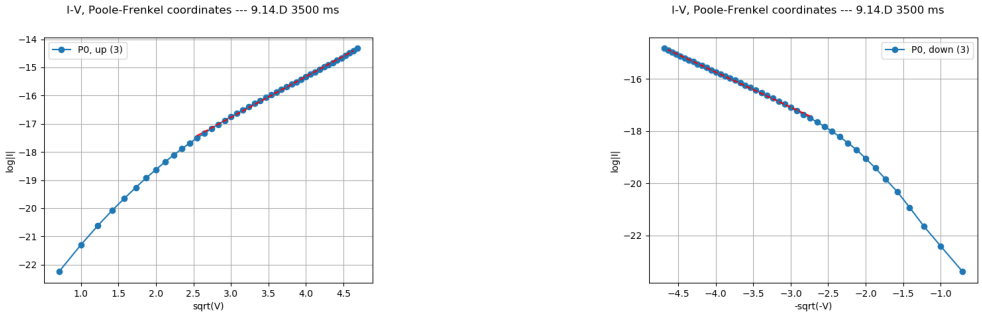

(a) **(b)**

Figure 5.14: *linear fits (red dashed lines in the plots) for the 9.14.D electrode in* ***Poole-Frenkel*** *coordinates. (a): $V > 0$, up; (b): $V < 0$, down.*

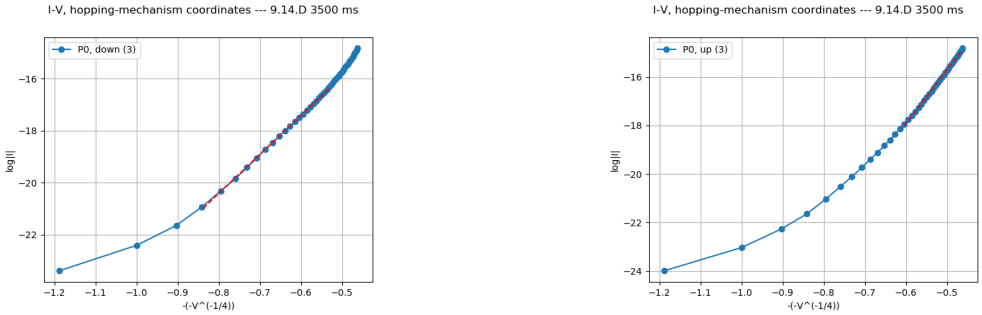

(a) **(b)**

Figure 5.15: *linear fits (red dashed lines in the plots) for the 9.14.D electrode in* ***hopping*** *coordinates. (a) and (b): $V < 0$, down and up, respectively.*

Results for electrode 9.12.B (PEDOT)

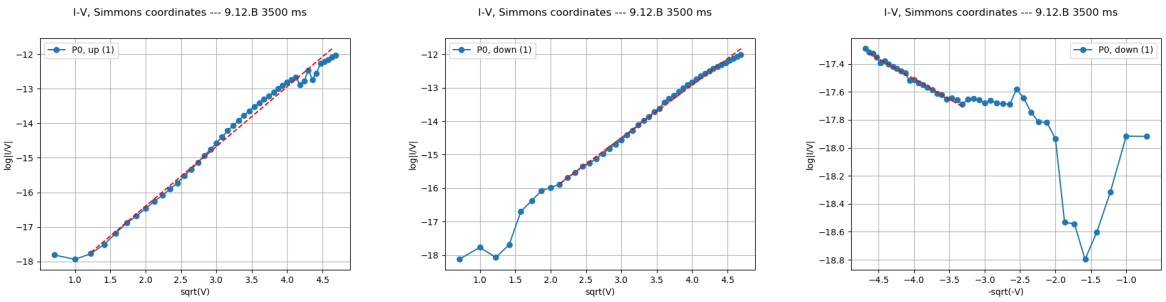

(a) **(b)** **(c)**

Figure 5.16: *linear fits (red dashed lines in the plots) for the 9.12.B electrode in* ***Simmons*** *coordinates. (a) and (b): $V > 0$, up and down, respectively; (c): $V < 0$, down.*

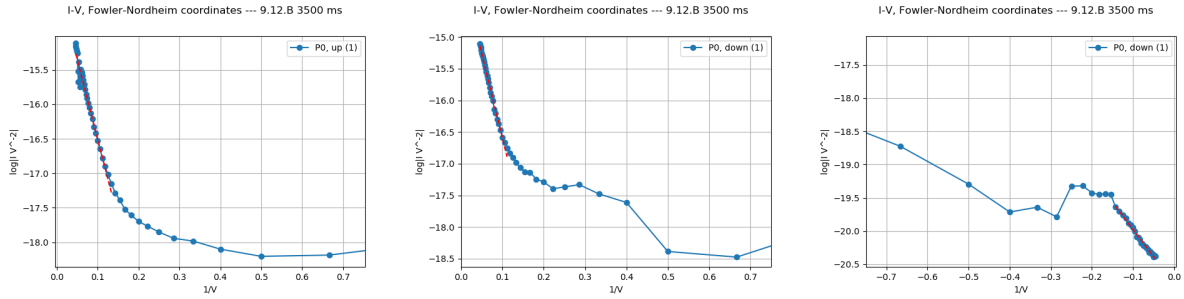

(a) **(b)** **(c)**

Figure 5.17: *linear fits (red dashed lines in the plots) for the 9.12.B electrode in* ***Fowler-Nordheim*** *coordinates. (a) and (b): $V > 0$, up and down, respectively; (c): $V < 0$, down.*

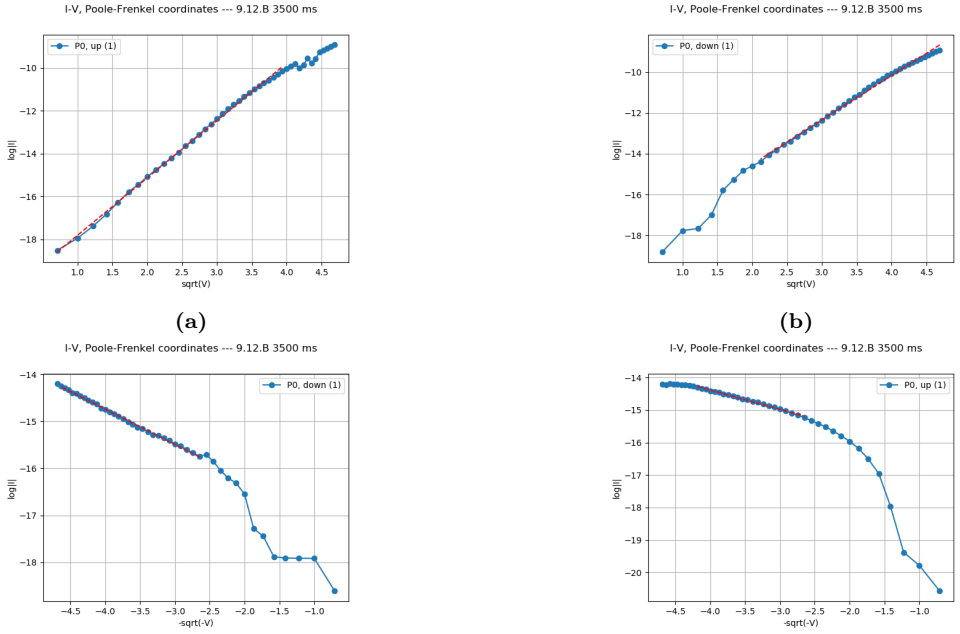

(a) **(b)** **(c)** **(d)**

Figure 5.18: *linear fits (red dashed lines in the plots) for the 9.12.B electrode in* ***Poole-Frenkel*** *coordinates. (a) and (b): $V > 0$, up and down, respectively; (c) and (d): $V < 0$, down and up, respectively.*

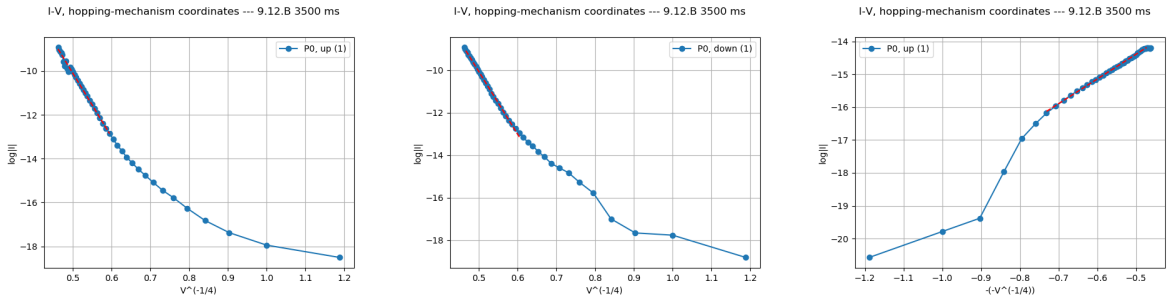

(a) **(b)** **(c)**

Figure 5.19: *linear fits (red dashed lines in the plots) for the 9.12.B electrode in* ***hopping*** *coordinates. (a) and (b): $V > 0$, up and down, respectively; (c): $V < 0$, up.*

Results for electrode 9.8.E (ITO)

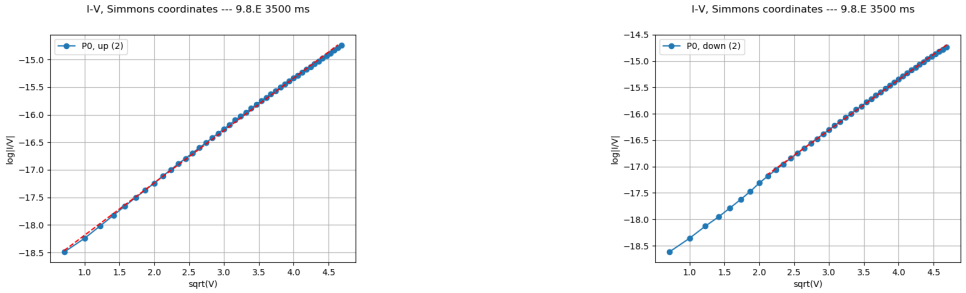

(a) **(b)**

Figure 5.20: *linear fits (red dashed lines in the plots) for the 9.8.E electrode in* ***Simmons*** *coordinates. (a) and (b):* $V > 0$*, up and down, respectively.*

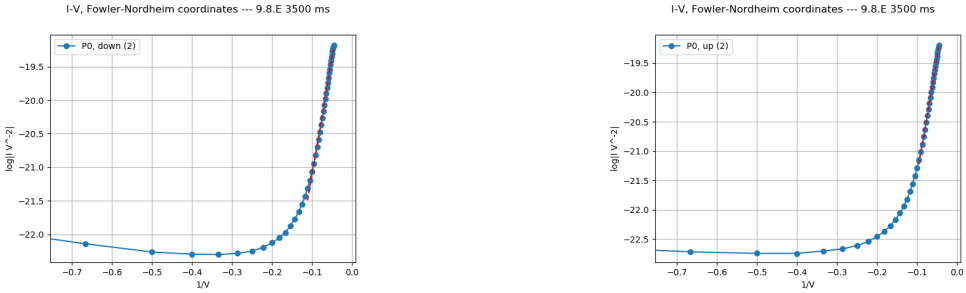

(a) **(b)**

Figure 5.21: *linear fits (red dashed lines in the plots) for the 9.8.E electrode in* ***Fowler-Nordheim*** *coordinates. (a) and (b):* $V < 0$*, down and up, respectively.*

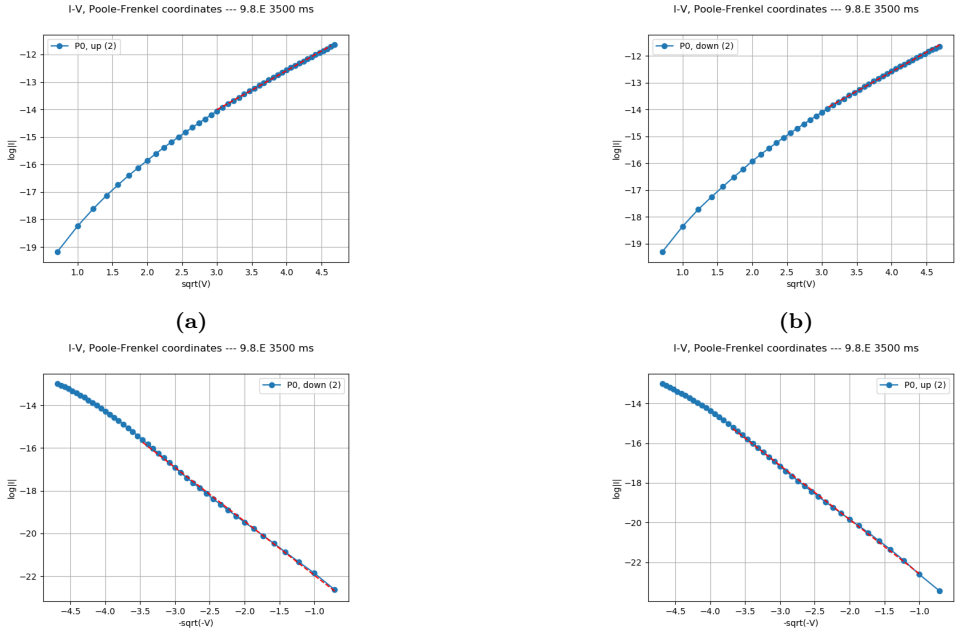

Figure 5.22: *linear fits (red dashed lines in the plots) for the 9.8.E electrode in* ***Poole-Frenkel*** *coordinates. (a) and (b): $V > 0$, up and down, respectively; (c) and (d): $V < 0$, down and up, respectively.*

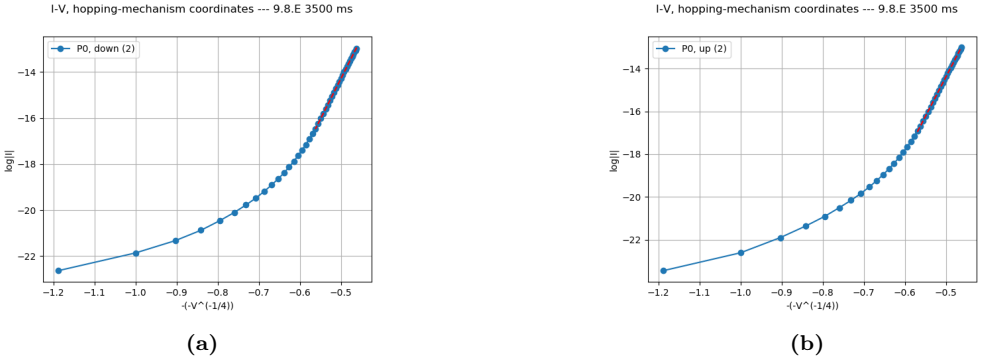

Figure 5.23: *linear fits (red dashed lines in the plots) for the 9.8.E electrode in* ***hopping*** *coordinates. (a) and (b): $V < 0$, down and up, respectively.*

The hopping mechanism model does not describe the obtained current measures in any case. In the bulk of the material the charge transport has mainly a polaronic nature and small polarons have a localization length that is of the order of the interatomic distances. Therefore, the localization lengths estimated from the fit results in hopping coordinates are too large by at least an order of magnitude. This agrees with the results of the simulation, discussed in section 3.1.4, which predicted an almost ohmic conduction for polaronic hopping in the measured voltage range.

The Fowler-Nordheim model does not describe the measured data, either. The potential barriers estimated from the fit results in Fowler-Nordheim coordinates are in fact too low to be compatible with the theoretical ones, which are higher than 3 eV.

For what concerns the Al and ITO electrodes, the estimated values for the dielectric constants ε from the Richardson-Schottky model are almost compatible with the one that is found in the

Electrode	**Dataset**	$\varepsilon_{\mathrm{R-S}}$	$\phi_{\mathrm{F-N}}$ [eV]	$\varepsilon_{\mathrm{P-F}}$	$N_{\mathrm{d\ (P-F)}}$ [cm^{-3}]	a_{hop} [nm]
9.14.D (Al)	$V > 0$, up	34 ± 1	0.11 ± 0.01	14 ± 1	$\sim 10^{19}$	/
	$V > 0$, down	26 ± 1	0.09 ± 0.01	/	/	/
	$V < 0$, down	44 ± 1	/	/	/	3.0 ± 0.2
	$V < 0$, up	27 ± 1	/	16 ± 1	$\sim 10^{19}$	2.8 ± 0.2
9.12.B (PEDOT)	$V > 0$, up	10 ± 1	0.13 ± 0.01	4.0 ± 0.1	/	2.6 ± 0.2
	$V > 0$, down	12 ± 1	0.14 ± 0.01	6.0 ± 0.1	/	2.6 ± 0.2
	$V < 0$, down	350 ± 30	0.065 ± 0.001	51 ± 2	/	/
	$V < 0$, up	/	/	82 ± 4	/	3.6 ± 0.2
9.8.E (ITO)	$V > 0$, up	32 ± 1	/	14 ± 1	$\sim 10^{19}$	/
	$V > 0$, down	31 ± 1	/	14 ± 1	$\sim 10^{19}$	/
	$V < 0$, down	/	0.17 ± 0.1	4.5 ± 0.5	$\sim 10^{17}$	2.5 ± 0.2
	$V < 0$, up	/	0.19 ± 0.1	3.8 ± 0.5	$\sim 10^{17}$	2.4 ± 0.2

Table 5.3: *physical quantities extracted from the fit results.*

literature ($\varepsilon = 28$, according to [16, 26]), while those from the Poole-Frenkel model are usually half the comparison value, or even lower. Still, the defects density, estimated by knowing the beginning of the linear region in Poole-Frenkel coordinates by using equation 3.23 in section 3.2.4, is found to be of the order of $10^{17} \div 10^{19}$ cm^{-3}, which could correspond to a fraction of the iron or niobium antisites concentrations, respectively $\sim 2 \times 10^{19}$ and $\sim 2 \times 10^{20}$ cm^{-3}.

The height of the interfacial barrier is however too high to be easily overcome by the electrons, since their thermal energy at 300 K is around 26 meV, which is over 100 times lower than the energy of the ideal barrier. Nonetheless, the barrier is probably lower than what is predicted by the theory. The phenomenon that affects the height of the barrier is related to the ferroelectric nature of the film: as found in [56] for the specific case of $BaTiO_3$ and in [57] for a more complex organic-inorganic perovskite material, the spontaneous polarization has an impact on the bending of the conduction and valence bands of the material. In particular, at the $+z$ and $-z$ surfaces of the crystal, the spontaneous polarization gives rise to two thin sheets of positive and negative charges. This creates a local electric field so that the electronic bands are thought to be intrinsically bent downwards at the $+z$ interface and upwards at the $-z$ interface; for this reason, the band diagram of an heterostructure made by a metal-ferroelectric-metal system would present barriers at the $+z$ and $-z$ interfaces that are respectively lower and higher than those in the correspondent metal-insulator-metal heterostructures. This is confirmed also by several papers, reporting the evidence of different measured work functions for ferroelectric domains with opposite polarization in lithium nobate; for example, in [58] a difference of more than 1.6 eV is found between P_{up} and P_{down} domains in a Mg:LN film.

A possible representation of the polarization-dependent band diagram in the case of Al and ITO electrodes is presented in figure 5.24. The effect of the positive polarization of the film is shown as a difference of 1.5 eV between the two interfacial barriers.

The barrier that is encountered by the electrons in our specific measurement scenario is always the one that corresponds to the $+z$ face of the ferroelectric film, which is indeed the lower one. In fact, let us suppose to have just taken some measures at negative voltage, with V_{bias} high enough to have caused the polarization to become negative in the film; the following measures are taken with a positive triangle function that reaches a sufficiently high V_{bias} to cause the polarization to return positive in the film (see figure 5.25); these measures have to be discarded

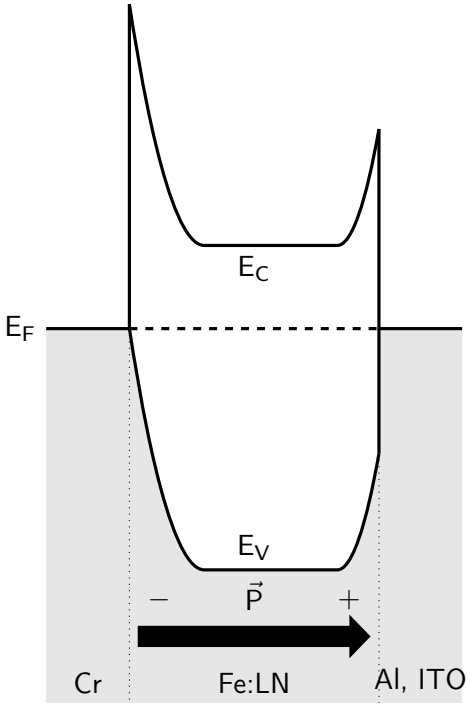

Figure 5.24: *ideal representation of the energy band diagram for the Cr/Fe:LN/Al and Cr/Fe:LN/ITO heterostructures when considering the ferroelectric nature of the Fe:LN film.*

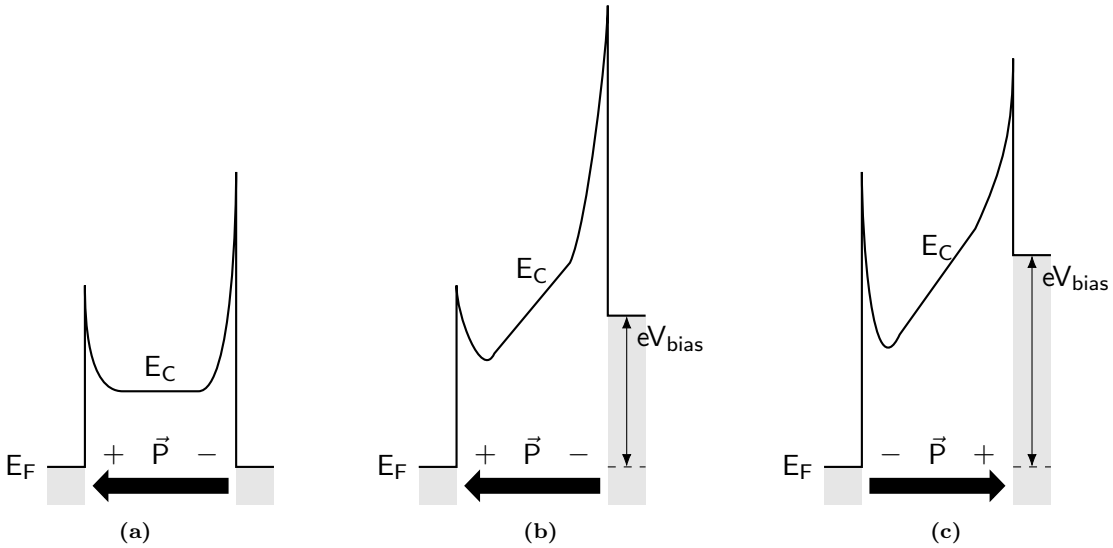

Figure 5.25: *energy band diagram for the Cr/Fe:LN/(Al, ITO) heterostructures when considering the polarization of the film; for simplicity, only the conduction band is shown.*
(a): the film is, for example, in the negative polarization state; (b): a voltage bias is applied between top and bottom electrodes; (c): eventually, increasing the applied bias causes the polarization to switch, changing the height of the interfacial barriers.

when modeling the charge transport mechanism, because of the unwanted hysteresis included in the I-V curve; taking again the same measures following a positive triangle function means rising the Fermi energy from the top-electrode-side and therefore the interfacial barrier blocking the electrons from flowing into the material is the one that is lowered by the thin layer of positive charges near the interface. The same thing happens when applying a negative bias: the first

negative voltage ramp flips down the polarization of the film during the measurement. When the following negative voltage ramp is applied, the Fermi energy of the bottom-electrode side is rised and thus the interfacial barrier that blocks the electrons from flowing into the material is again the one that is lowered by the thin layer of positive charges near the interface.

Now, it should be mentioned that almost all the measures obtained for the PEDOT:PSS electrodes were more noisy than the ones obtained for Al and ITO electrodes, often showing a behaviour dependent on the contact between the metal tip and the electrode's surface. This could be due to the softness of the material's surface; in fact, after almost every electrical contact made with the metal tip, the electrode surface was scratched a little bit, meaning that during the electrical measurements the PEDOT:PSS was too soft to sustain even the minimal pressure exerted by the metal tip, causing the electrodes to be damaged.

The Richardson-Schottky and the Poole-Frenkel models seem to describe qualitatively the conduction mechanism in the case of the PEDOT:PSS electrode for positive voltages, nonetheless the estimated dielectric constants are far from the one found in literature. Moreover, it is not clear where actually is the beginning of the linear portion of the curve in Poole-Frenkel coordinates, therefore the estimation of the trap density has not been possible. For what concerns the negative voltages, the only reliable result comes from the *down* dataset in Poole-Frenkel coordinates.

To summarize, the models that better suit the data, as suggested by the analysis results, are presented in table 5.4. Up and down datasets have been comprised within their positive or negative voltage branches; in fact, once the polarization currents have been removed from the analysed data, the measured current at a particular voltage bias and at steady state should not depend on the history of applied voltages.

El. material	**Voltage**	**Model(s)**
Al	$V > 0$	R-S or P-F
	$V < 0$	R-S or P-F
PEDOT	$V > 0$	R-S or P-F
	$V < 0$	P-F
ITO	$V > 0$	R-S or P-F
	$V < 0$	R-S or P-F

Table 5.4: *best fitting models for each electrode material.*

To obtain a better modeling of the PEDOT:PSS heterostructures, the problems derived by the softness of the polymeric material could be addressed by changing the design of the electrode. The PEDOT:PSS thin film could be coated with the deposition of a thin layer of another suitable electrode material, *e.g.* aluminium if the measurement is not expected to be done in illuminated conditions, before removing the Kapton mask needed for the spin coating deposition. This would provide a more resistant surface to protect the PEDOT:PSS from the metal tip, while leaving the heterostructure of the sample almost intact.

As a perspective, further insights could be obtained by implementing a temperature control in the sample placer. The charge transport models described in 3.2 show different temperature dependences, therefore the study of the I-V curves at different temperatures would help to understand better the correct model for the different electrodes. Furthermore, the temperature dependence would provide access to additional physical quantities related to those models, such as the potential barrier in the case of the Richardson-Schottky model.

5.3 Polarization switching currents

As can be seen from the I-V curves presented at the beginning of section 5.2, in some regions of the plots there is a very noticeable hysteresis, affecting the three different electrode materials, meaning that the presence of the hysteresis is due to the film rather than to the type of contact at the interfaces. It can be observed that when applying a series of positive triangles followed by a series of negative ones, the hysteresis always shows up in correspondence to the first positive or negative triangles. Remembering the ferroelectric nature of the Fe:LN film under analysis, the hysteresis could be due to the switch of polarization direction in the film and possibly to the correlated structural relaxation at the atomic level. The particular case of the measured peaks in the PEDOT:PSS I-V characteristics deserves some more attention and will be studied in this section.

The samples with PEDOT:PSS as the top electrode manifest a specific and reproducible hysteretic behaviour. In particular, the hysteresis consists of two current peaks that emerge around specific positive and negative voltages when a positive voltage ramp is measured after having applied one or more negative ramps and *vice versa*. The particular conditions at which these peaks are measured suggest that we are potentially dealing with poling currents.

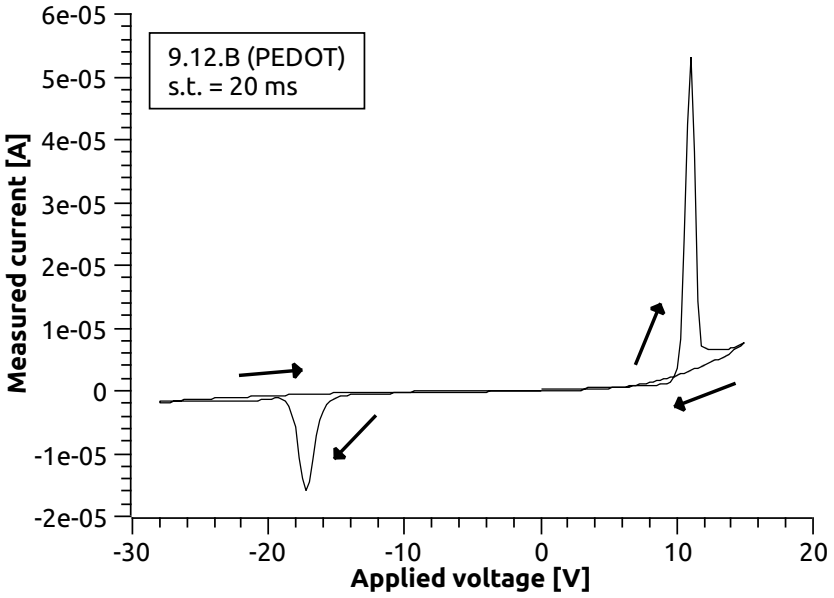

Figure 5.26: *the currents peaks observed in the I-V curves of samples with PEDOT:PSS as top electrodes. Notice that the applied voltage range is asymmetric, going from* -28 *to* $+15$ V.

Let us consider the two thin sheets of positive and negative charges that are distributed close to the $+z$ and $-z$ faces of the film because of the spontaneous polarization. The polarization switching is basically the movement of the off-centered atoms (Li and Nb) to their alternative equilibrium position in the lattice and macroscopically has the effect of changing the sign of the net charges distributed close to the z faces of the film. If the Fe:LN film is contacted with electrodes at the top and the bottom and is connected to a closed circuit, the switching of the net charges is then compensated by the arrival of opposite charges to the electrodes, provided by the external circuit. Notice, in this regard, that the sign of the measured current peaks (positive for positive voltages and *vice versa*) is coherent with the microscopic behaviour of the polarization switching: let us consider for simplicity the face of the film contacted to the top electrode and let us suppose that the polarization is, for example, negative; the polarization switching makes

the negative charges close to the top surface become positive, attracting electrons from the outer circuit to compensate; but then the electrons current is measured as a positive current output by the source meter (see figure 5.27). The same argument applies to the other cases. Note also that, given the nature of the polarization switching and known that the measured currents are actually flowing in the outer circuit towards the electrodes rather than inside the film, the poling currents are added on top of the I-V characteristic curve and are not affected by the discussion around the charge transport modeling.

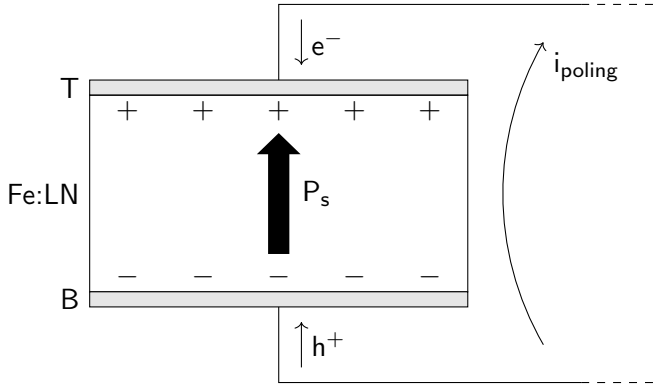

Figure 5.27: *electrons (holes) flow towards the top (bottom) electrode after the polarization is switched to positive, giving a positive current* i_{poling} *in output.*

To confirm the hypothesis of polarization switching currents, there are some physical quantities that can be measured and compared with what is found in other reasearch works. The two main parameters that define the phenomenon of the polarization switching currents are the spontaneous polarization P_{s} and the coercive field E_{c}, *i.e.* the threshold electric field that has to be applied to the Fe:LN film to switch the direction of its spontaneous polarization. Both quantities can be extracted from the I-V curves that have been measured with the source meter.

To estimate the coercive field, it is sufficient to mark the voltage at which the peak has its maximum and divide it by the nominal thickness of the film.

Then, the total charge in the peaks should correspond to the difference between the charge distributed near the top surface of the film before and after the polarization switching. Therefore, the total charge divided by the area of the electrode should allow to estimate $2P_{\mathrm{s}}$.

To take one single current value, after the application of a voltage to the sample the source meter waits a time equal to the settling time and then takes a certain number of current measures (using a standard ratiometric analog/digital conversion technique[50]) for a duration that we call acquisition time; then it computes and store the average current value measured in that time. Thus, to get a measure of the charge within the peaks it is sufficient to integrate the current as if it was a function of time. Since the source meter measures a single average current value for each voltage step, the integral of each current value is performed by taking into consideration a time interval equal to the acquisition time.

The charge is estimated for each applied voltage, starting for example from the currents measured by a positive voltage ramp, as follows:

- define the initial charge as $C_0 \equiv 0$ μC;
- compute the charge for each j-th applied voltage as $C_{\mathrm{j}} = C_{\mathrm{j}-1} + \frac{1}{2}(I_{\mathrm{j}-1} + I_{\mathrm{j}})\Delta t$, with I_{j} the current at the j-th applied voltage and Δt the acquisition time.

This procedure includes also the electronic contribution to the current, which obviously is not related to the polarization switching. A simple condition in the algorithm can be included to eliminate the I-V characteristics from the final measure of the polarization: once the maximum applied voltage is reached, the computation of the charge flowed in the circuit C_j is carried on by *subtracting* the next contributions. This is done until the point at 0 volts is reached. This approach is repeated equally for measures taken with negative voltage ramps: summing the charge contributions down to the minimum applied voltage and then subtracting them going back up to zero volts.

After each triangular voltage ramp, the total charge flowed between the beginning and the end of the triangular ramp, divided by the electrode area ($A \sim 5$ mm^2 in the case of PEDOT:PSS electrodes), gives an estimation of $2P_s$. In the results will be presented directly the measure of the polarization for both positive and negative current peaks, P_s^+ and P_s^- respectively.

One other thing that is evident from the I-V curves is that the positive and negative current peaks do not appear at the same applied electric field. Therefore, the difference between the coercive field at positive and negative voltages, called internal residual field, will also be measured simply as $E_r = (E_c^- - E_c^+)/2$.

The study of polarization switching currents has been carried on by analysing I-V curves measured for the 9.12.B and 9.12.F electrodes. Observing preliminary current measurements, like the one in figure 5.26, the current peaks are always found around +10 V and between −20 and −15 V, therefore the applied voltage range has been chosen to go from −28 to +16 V.

The first analysis on 9.12.B is performed on two I-V curves measured with 20 ms of acquisition time and settling times of 1 and 20 ms. The measures have been taken by applying a negative voltage triangular ramp followed by a positive one. I-V and polarization curves are shown in figure 5.28. In table 5.5 are shown the measured quantities, instead.

Then, the measures on the 9.12.F electrode have been carried on by varying both the acquisition time and the settling time. The acquisition time has been varied manually between the *fast*, *medium* and *normal* speed settings on the source meter, corresponding to 200 µs, 2 ms and 20 ms of acquisition time respectively. The settling time has been varied instead between 1 µs, 10 µs, 100 µs and 1 ms. I-V and polarization curves are shown in figures 5.29, 5.30 and 5.31, while the measured quantities are presented in table 5.6.

s.t. [ms]	E_c^+ [kV/mm]	E_c^- [kV/mm]	E_r [kV/mm]	P_s^+ [µC/cm^2]	P_s^- [µC/cm^2]
1	37 ± 3	58 ± 4	11 ± 3	62 ± 2	48 ± 2
20	37 ± 3	58 ± 4	11 ± 3	27 ± 1	24 ± 1

Table 5.5: *coercive fields $E_c^\pm$, internal residual field E_r and polarizations $P_s^\pm$ measured for the 9.12.B electrode at 1 and 20 ms of settling time.*

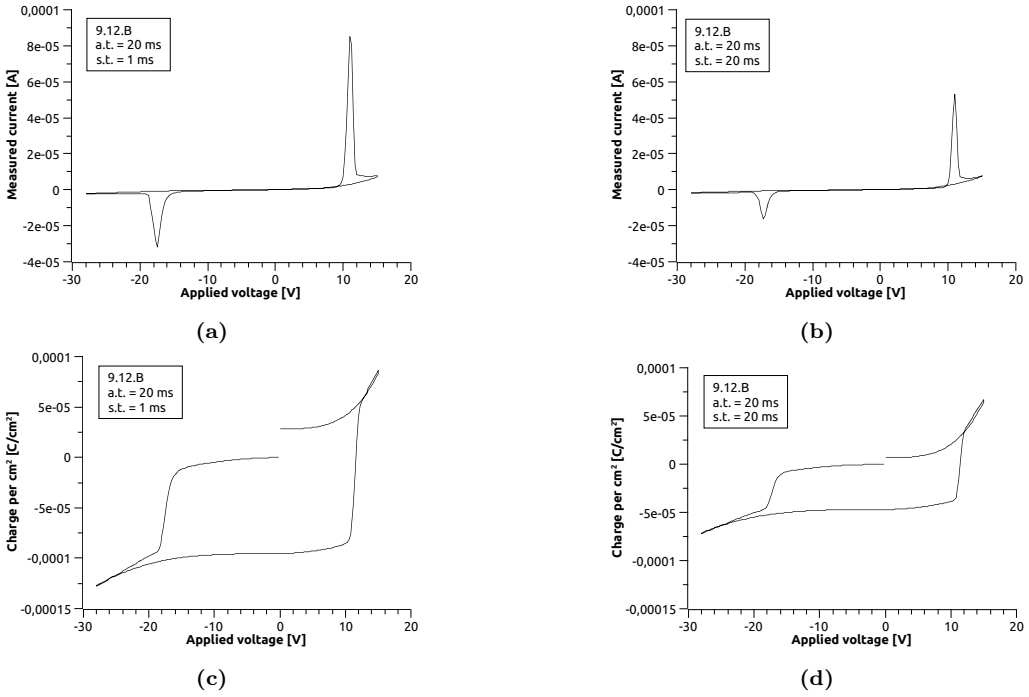

Figure 5.28: *in (a) and (b) the I-V curves for 1 and 20 ms, respectively; in (c) and (d) their polarization curves, computed following the algorithm described at the beginning of this section.*

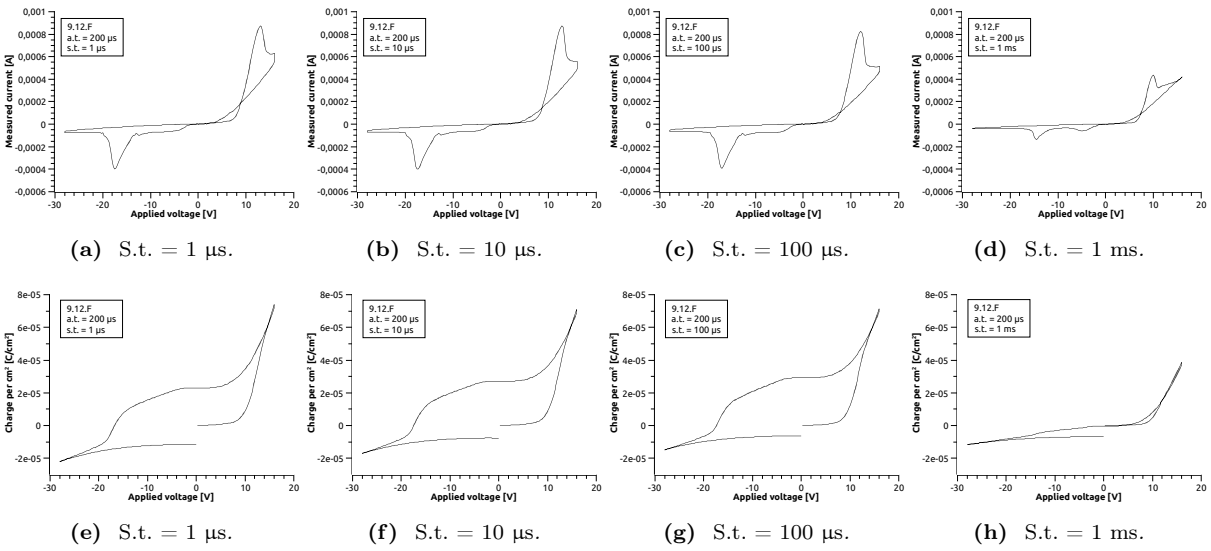

Figure 5.29: *I-V (top) and polarization curves (bottom) for a* ***fast*** *acquisition time,* a.t. = 200 µs.

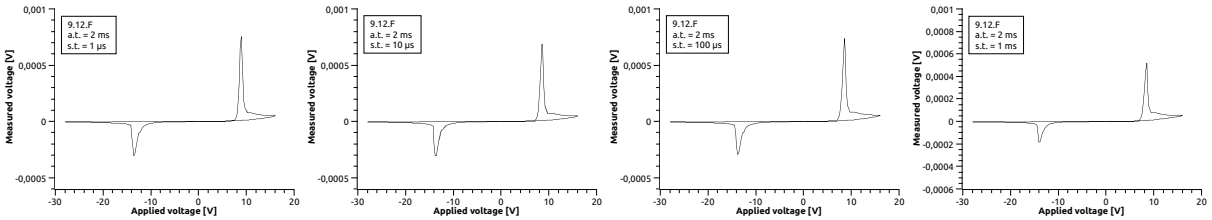

(a) S.t. = 1 µs.

(b) S.t. = 10 µs.

(c) S.t. = 100 µs.

(d) S.t. = 1 ms.

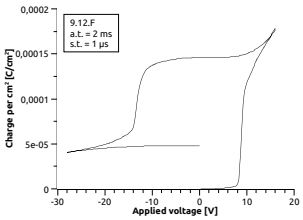

(e) S.t. = 1 µs.

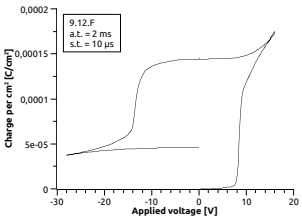

(f) S.t. = 10 µs.

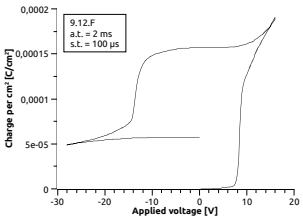

(g) S.t. = 100 µs.

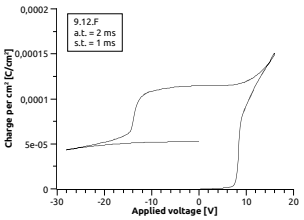

(h) S.t. = 1 ms.

Figure 5.30: *I-V (top) and polarization curves (bottom) for a* ***medium*** *acquisition time,* a.t. = 2 ms.

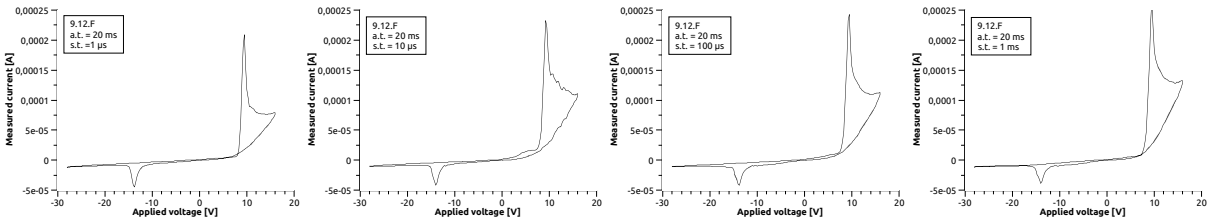

(a) S.t. = 1 µs.

(b) S.t. = 10 µs.

(c) S.t. = 100 µs.

(d) S.t. = 1 ms.

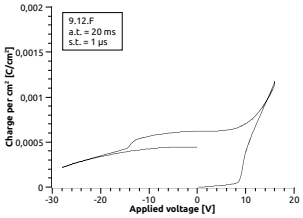

(e) S.t. = 1 µs.

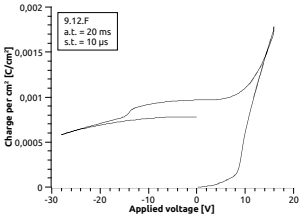

(f) S.t. = 10 µs.

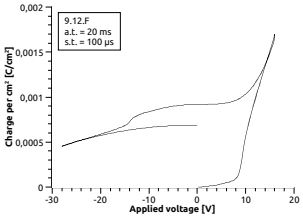

(g) S.t. = 100 µs.

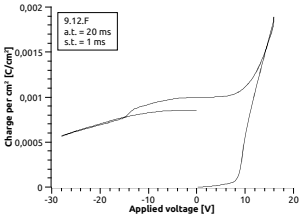

(h) S.t. = 1 ms.

Figure 5.31: *I-V (top) and polarization curves (bottom) for a* ***normal*** *acquisition time,* a.t. = 20 ms.

a.t. [ms]	**s.t.** [ms]	E_c^+ [kV/mm]	E_c^- [kV/mm]	E_r [kV/mm]	P_s^+ [$\mu C/cm^2$]	P_s^- [$\mu C/cm^2$]
0.2	0.001	43 ± 3	58 ± 4	8 ± 3	11.5 ± 0.5	17.3 ± 0.7
	0.01	43 ± 3	58 ± 4	8 ± 3	13.5 ± 0.5	17.4 ± 0.7
	0.1	40 ± 3	57 ± 4	9 ± 3	14.6 ± 0.6	17.9 ± 0.7
	1	33 ± 2	49 ± 4	8 ± 2	0.0 ± 0.1	3.3 ± 0.1
2.0	0.001	30 ± 2	45 ± 3	8 ± 2	73 ± 3	49 ± 2
	0.01	28 ± 2	46 ± 3	9 ± 2	72 ± 3	49 ± 2
	0.1	28 ± 2	46 ± 3	9 ± 2	78 ± 3	50 ± 2
	1	28 ± 2	46 ± 3	9 ± 2	57 ± 2	31 ± 1
20.0	0.001	32 ± 2	46 ± 3	7 ± 2	310 ± 10	88 ± 4
	0.01	31 ± 2	47 ± 3	8 ± 2	485 ± 20	93 ± 4
	0.1	32 ± 2	46 ± 3	7 ± 2	460 ± 20	117 ± 5
	1	32 ± 2	47 ± 3	8 ± 2	500 ± 20	72 ± 3

Table 5.6: *coercive fields $E_c^\pm$, internal residual field E_r and polarizations $P_s^\pm$ measured for the 9.12.F electrode at different acquisition and settling times.*

The errors associated to the coercive fields have been estimated by considering the precision of the peak-maximum voltage, which is due to the discretization of the voltage-axis, and the uncertainty related to the thickness of the Fe:LN film. The errors associated to the polarization of the film, instead, have been estimated by considering the instrumental accuracy of the measured currents, amplified by their sum along the whole triangular voltage ramp, and the uncertainty on the effective area of the electrode.

The I-V curves measured on the 9.12.F electrode at 20 ms of acquisition time (figure 5.31) show a substantial difference from the ones measured for 9.12.B, which are equally measured at 20 ms of acquisition time, even when comparing the curves at the same settling time of 1 ms (figure 5.28a). This has clearly a major impact on the results of the polarization measures. In particular, the positive-side of the I-V curves seems to be boosted in amplitude on the 9.12.F with respect to the other case, resulting in P_s^+ values that are an order of magnitude higher than all the other cases.

Regardless, the measured coercive fields are always between 28 and 43 kV/mm (positive current peak) and between 45 and 58 kV/mm (negative current peak). This is in line with what is found in literature: for example, in [51] are found coercive fields around 20 kV/mm for Fe:LN films with iron concentrations similar to that of our samples.

The residual field indicates that some additional field is present in the sample. A possible origin for this field is attributed to the presence of polar defects.[59] Those defects cannot be switched at room temperature and work as permanent electric dipoles embedded in the crystal volume. Collectively they produce a macroscopic field that sums up to the applied one, shifting the hysteresis loop. In lithium niobate, those permanent dipoles are generally attributed to the Nb_{Li} antisite defects that are present with large concentrations in congruent crystals.[60]

For what concerns the measure of the polarization, apart from the case of the 9.12.F electrode at 20 ms of acquisition time and few other singular cases, the estimated values for $P_s^\pm$ are of tens of μC per squared centimetre. In particular, the values for P_s^+ for the 9.12.B electrode at 1 ms of settling time and those for the 9.12.F electrode at 2 ms of acquisition time at all settling times are in line with the value of about 70 $\mu C/cm^2$ usually reported for the congruent $LiNbO_3$.[61] A variation in the polarization magnitude from sample to sample is not unusual and is generally

attributed to the presence of polar defects located both at the interfaces and in the bulk of the material. Those defects may be local charges accumulation regions due to inhomogeneous population of Fe traps or structural features like dislocations. The polar defects act as pinning centers for ferroelectric domains. When the field is applied above the coercive threshold of an homogeneous crystal, the regions surrounding polar defects do not reverse their polarization as this is pinned by the defect. This creates some residual domains whose volume fraction is proportional to the lack of polarization.

It should be noted, however, that there is an evident correlation between the two time parameters (settling and acquisition time) and the measured polarizations. Actually, non-equilibrium phenomena, such as the polarization switching, are difficult to be represented by considering only one average-current value per voltage step (see for example the hypothetical case described by figure 5.32). The correlation between the data and the measuring procedure suggests that the poling currents are described by a non-trivial dependence on time.

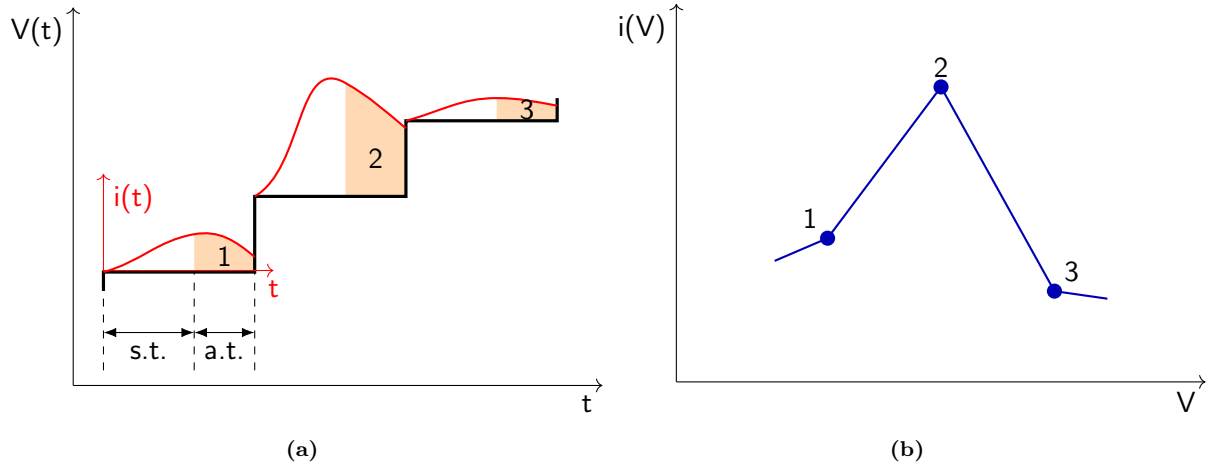

Figure 5.32: *schematic representation of the measuring procedure followed by the source meter; for each applied voltage, the instrument waits a time interval equal to the settling time (s.t., which is set by the user), then it measures a number of current values for a time equal to the acquisition time (a.t., which can also be set by the user) and finally stores its average value. As an example, in (a) are shown the hypothetical current measurements that are performed at three consecutive voltage steps, which translate into the I-V characteristic presented in (b).*

It should be observed also that the polarization obtained from the negative current peaks always results as a different value from that measured from the positive peaks. This could be due to the combination of (i) the effect ferroelectricity has on the band diagrams of the heterostructures and (ii) the asymmetry of the I-V curves. The first effect has been discussed in the previous section 5.2. Let us suppose, for example, that the material is polarized negatively; then, during the first half of a positive triangular ramp the film polarization switches back to positive; this means that the potential barrier that is encountered going from the top electrode towards the Fe:LN is initially higher than its predicted value (because the top electrode touches the $-z$ face of the film), but becomes lower when eventually the applied voltage is enough to flip up the polarization (the top electrode touches now the $+z$ face of the film) and the same barrier height is presented at the second half of the triangular ramp; therefore the currents measured by the first half of the triangular ramp follow a different I-V curve than those measured by the second half. Secondly, the currents measured at negative voltage biases are usually at least one order of magnitude lower than those at positive biases and their impact on the measure of the polarization is much less. To combine the two effects means that the error done in measuring P_s^+ is not equally compensated by the error done in measuring P_s^-.

The issue of the residual polarization charge could be also due to the measure of the polarization being based solely on one current acquisition per applied voltage. Since the source meter does not provide the time evolution of the measured currents, as discussed previously the two peaks could be described by very different current profiles.

Finally, it can be observed that the width of the poling current peaks does not change very much across the different experimental conditions, laying around ~ 2 V and ~ 3 V for positive and negative peaks, respectively. Two exceptions come from the measures on the 9.12.F electrode: with 200 µs of acquisition time (figure 5.29), both the positive and negative peaks are much broader (around 7 V); with 20 ms of acquisition time (figure 5.31), the positive peaks present a large tail towards higher voltages. What can be understood from the observed phenomenon is that the polarization switching is actually completed only across a range of ~ 7 and ~ 10 kV/mm around the positive and negative coercive fields, respectively.

To conclude, the analysis shows that PEDOT:PSS electrodes are good candidates to study the polarization switching mechanism in Fe:LN. However, the material has the tendency to be easily damaged by the contact with the metal tip, making it more and more difficult to find a properly-working contact point on the electrode. To overcome this issue, as stated at the end of section 5.2, the PEDOT:PSS electrodes could be coated with another electrode material, with better mechanical properties. The measures could be improved by studying the time evolution of the poling current, using an oscilloscope in combination with properly designed custom input signals, as briefly introduced at the end of section 5.1 and described in the appendices.

5.4 Photogalvanic currents

The photogalvanic current has been measured as the current at 0 volts from I-V curves taken under uniform illumination provided by the two LEDs described in section 4.2.2. The I-V curves have been measured for 6 increasing light intensities varied by setting the LED-driver potentiometer. After each intensity variation, a minute has been waited before starting the next acquisition to let dissipate pyroelectric currents potentially due to the heating of the sample under illumination. The I-V curves have been measured by applying a postive triangle ramp, a positive-negative double-triangle ramp and a negative-positive ramp. The choice of applying two positive triangles before measuring the actual photogalvanic current should provide control over the polarization state of the film prior to the measurement; it should also ensure cleaner, hysteresis-free I-V curves. The next two negative triangle ramps should serve the same purpose. Using double-triangle ramps should instead ensure to get clean measures at 0 V, avoiding the offset shown in figure 4.8 of section 4.3. To distinguish the results obtained from the first and second double-triangle ramps, we will refer to their original datasets as A and B, respectively.

The measures were taken on the 9.10.B (PEDOT) and 9.8.E (ITO) electrodes. An example of I-V curves under illumination is presented in figure 5.33.

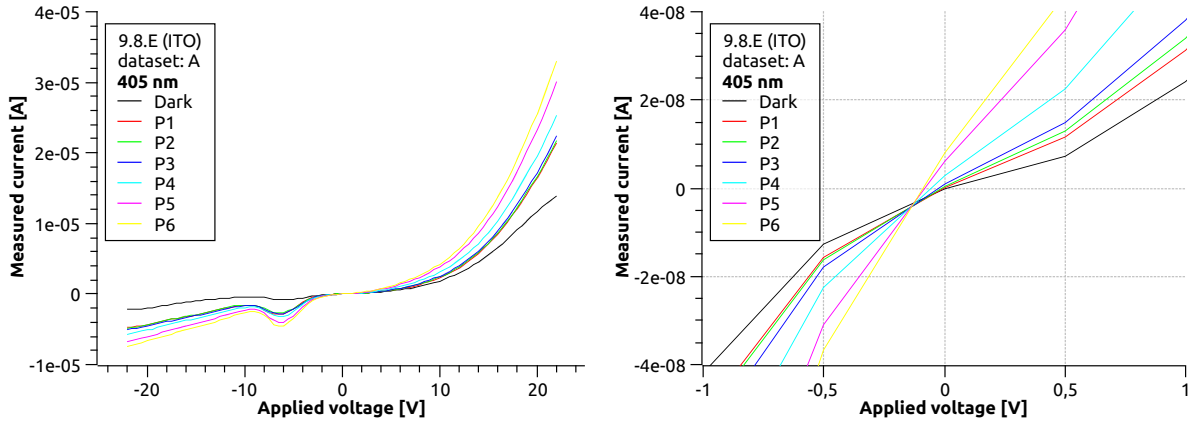

(a) (b)

Figure 5.33: *I-V curves measured for the 9.8.E electrode under* 405 nm *light illumination at different intensities. The curves correspond to voltage ramps going from* +20 *to* −20 V*, i.e. they are the central portion of a positive-negative double-triangle ramp. (a) shows the whole I-V curve, while (b) shows only the region around 0 volts.*

The photogalvanic currents are presented in fugures 5.34and 5.35 for the ITO electrode and in figures 5.36 and 5.37 for the PEDOT:PSS electrode. The plots show i_{PG} as function of the measured irradiance of the LEDs, appropriately multiplied by the optical transmittance of the electrodes at the different wavelengths, obtained in section 4.1.3. Specifically, the irradiance has been reduced to 85 % at 530 nm and to 90 % at 405 nm in the case of ITO, while it has been reduced to 90 % for all the wavelengths in the case of PEDOT:PSS.

The photogalvanic current, introduced in section 3.1.3, is described by the following relation

$$J_{\mathrm{PG}} = esN\frac{I}{h\nu}\phi L_{\mathrm{PG}} \tag{5.1}$$

and can be estimated approximately to get an order of magnitude, useful for comparison. Let us consider $s \sim 10^{-21}$ m^2 from [62], $N \sim 10^{-20}$ cm^{-3} from the fact that [Fe^{2+}] is only a fraction of the total [Fe] in the Fe:LN film, $h\nu = 2.3$ eV as the energy of the 530 nm LED radiation,

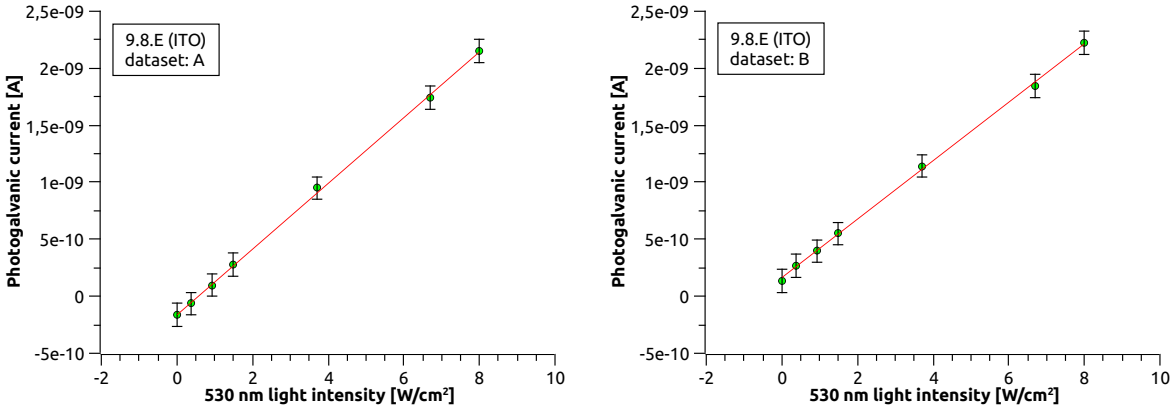

(a) (b)

Figure 5.34: *photogalvanic currents measured for the* ***ITO*** *electrode under* **530 nm** *light illumination. The linear interpolation of the data is represented by a red straight line.*

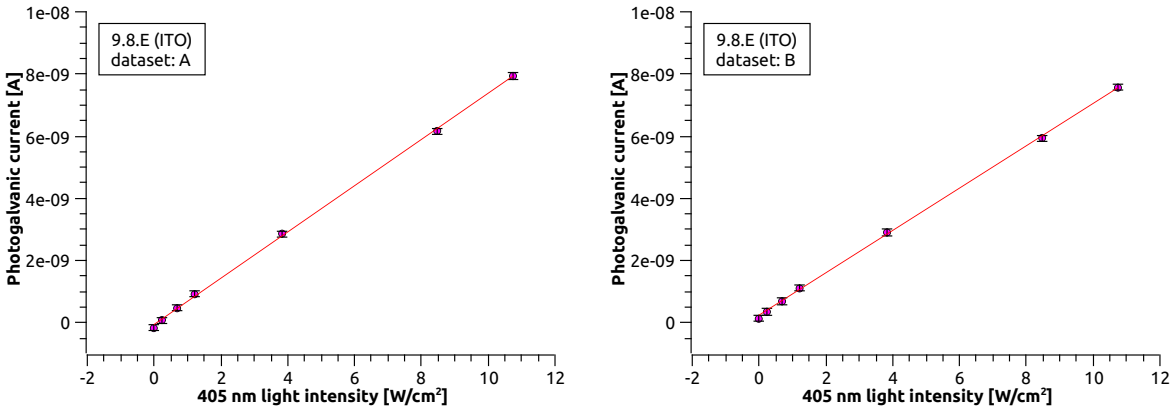

(a) (b)

Figure 5.35: *photogalvanic currents measured for the* ***ITO*** *electrode under* **405 nm** *light illumination. The linear interpolation of the data is represented by a red straight line.*

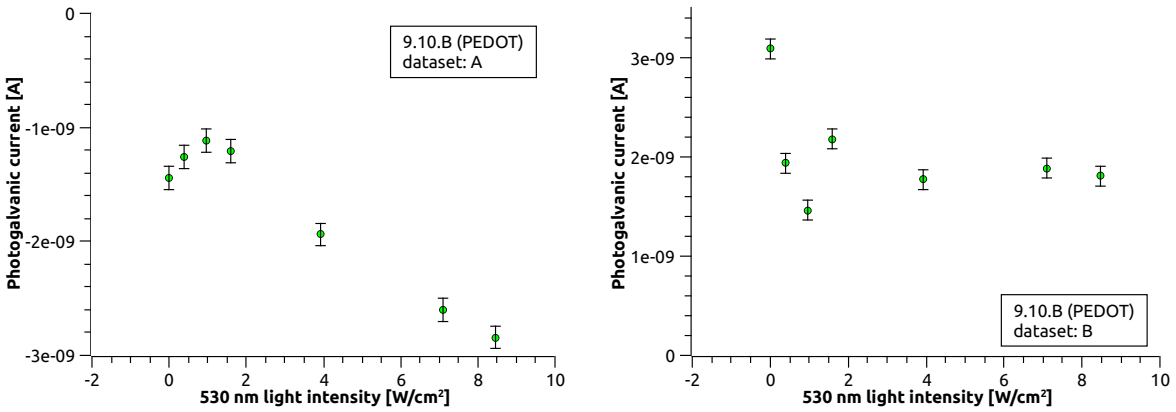

(a) (b)

Figure 5.36: *photogalvanic currents measured for the* ***PEDOT*** *electrode under* **530 nm** *light illumination.*

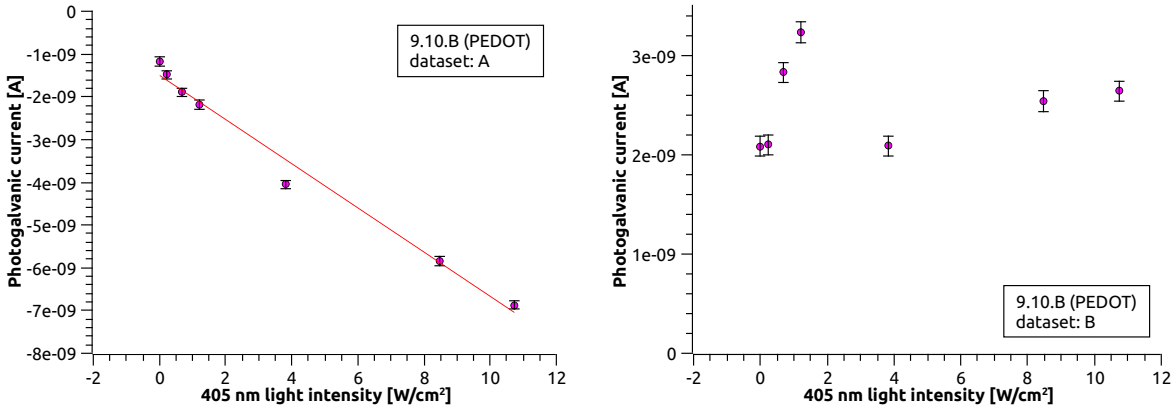

(a) (b)

Figure 5.37: *photogalvanic currents measured for the* ***PEDOT*** *electrode under* **405 nm** *light illumination. The linear interpolation of the data in (a) is represented by a red straight line.*

$I = 10$ W/cm^2, $L_{\mathrm{PG}} \sim$ nm and finally a realistic efficiency $\phi \sim 1$ %. Then, the expected photogalvanic current is estimated as $i_{\mathrm{PG}} = J_{\mathrm{PG}} A$, where $A \sim 5$ mm^2 is the area of our ITO and PEDOT:PSS electrodes, giving $i_{\mathrm{PG}} \sim 2$ nA. We should expect very similar results for the computation in the case of the 405 nm LED. As it can be seen, the photogalvanic currents measured for the 530 and 405 nm LEDs are consistent with the expected order of magnitude, both for ITO and PEDOT:PSS.

The sign of the photogalvanic currents is determined by the direction of the polarization of the Fe:LN film. In particular, the non-centrosymmetric atomic arrangement of the lattice dictates for the photo-generated charge carriers a preferred direction to follow.[34] Thus, a net current of negative charges flows in the same direction of the polarization vector, which is parallel to the c axis, and is read as a positive current flowing in the opposite direction of the polarization. Datasets A and B are measured, as said at beginning, after having run positive and negative voltage ramps, respectively, and for this reason they should correspond to positive and negative polarization states of the film, respectively. If this was true, negative photogalvanic currents should have been measured by datasets A and positive ones by datasets B. The data obtained with ITO electrodes appear not to be consistent with this expectation, as reported in figures 5.34 and 5.35. This must be due to the impossibility of polarization switching to occur in the 9.8.E electrode; a possible cause could be, for example, a higher thickness of the film under the ITO electrode, which would make the applied voltages insufficient to reach the coercive field of the film. This is in line with the I-V characteristic measured for ITO, presented at the beginning of section 5.2, which did not show clear evidence of poling currents.

In the case of PEDOT:PSS electrodes, the situation is less clear. While in figures 5.36a and 5.37a the photogalvanic current appears to be proportional to the light irradiance and with a sign in agreement with a polarization reversal, which is studied in section 5.3, the measures from dataset B for the electrode 9.10.B show currents that are scattered around a constant value of about ~ 2 nA, meaning that they do not depend on the light irradiance.

The linearity of the measures has been studied by performing a linear interpolation of the data, to obtain a measure of the increase rate of the photogalvanic current with the intensity of the radiation that invests the Fe:LN film for the different wavelengths. The fit results, already included in the plots, are presented in table 5.7. The case of dataset A at 530 nm for the PEDOT:PSS electrode will be discussed later.

Electrode	LED	Dataset	Slope [10^{-10} A cm^2/W]	Intercept [nA]
9.8.E (ITO)	530 nm	A	2.9 ± 0.1	-0.16 ± 0.05
	530 nm	B	2.6 ± 0.1	$+0.16 \pm 0.05$
	405 nm	A	7.4 ± 0.1	-0.05 ± 0.05
	405 nm	B	6.8 ± 0.1	$+0.22 \pm 0.05$
9.10.B (PEDOT)	530 nm	A	/	/
	530 nm	B	/	/
	405 nm	A	-5.2 ± 0.1	-1.50 ± 0.05
	405 nm	B	/	/

Table 5.7: *fit results for the photogalvanic currents measured as functions of illumination intensities.*

Let us discuss the case of ITO first.

The linear interpolations confirm the direct proportionality of the photogalvanic current on the light intensity I, as predicted by equation 5.1. The results show also that the increase rate of the photogalvanic current with light irradiance is different when illuminating with different wavelengths.

The proportionaly coefficient between the photogalvanic current and the light irradiance is given by

$$J_{\mathrm{PG}} = s(\lambda)\, N_{\mathrm{Fe^{2+}}}\, \kappa(\lambda)\, I \tag{5.2}$$

where s is the absorption cross section, $N_{\mathrm{Fe^{2+}}}$ is the filled donor concentration and κ is the Glass factor. We do not have a quantitative estimation of the Fe^{2+} concentration in our samples. However, the ratio $J_{\mathrm{PG}(530\ \mathrm{nm})}/J_{\mathrm{PG}(405\ \mathrm{nm})}$ is independent from the Fe^{2+} concentration and can be compared with literature data. Knowing that $\alpha = s\, N_{\mathrm{Fe^{2+}}}$, in [34] are found the quantities reported in table 5.8, which allow to estimate a ratio $(\alpha\kappa)_{530\ \mathrm{nm}}/(\alpha\kappa)_{405\ \mathrm{nm}} \sim 0.37$. In our case the ratios between the slopes at $\lambda = 530$ nm and $\lambda = 405$ nm for the ITO electrode are 0.39 ± 0.02 and 0.38 ± 0.02 for the A and B datasets, respectively, thus our results are in good agreement with what is found in literature.

λ [nm]	α [1/cm]	κ [10^{-9} A cm/W]
530	~ 20	~ 0.7
405	~ 25	~ 1.5

Table 5.8: *iron optical absorption coefficient α and Glass factor κ at two different wavelengths.*[34]

Let us consider now the case of the PEDOT:PSS electrode.

The slope of the linear interpolation in the case of 405 nm illumination is smaller than the one that is measured for the ITO electrode. Assuming the iron concentration to be exactly the same across the whole Fe:LN film, the difference could be due to a decrease in the Fe^{2+} concentration, corresponding to their possible oxidation to Fe^{3+} caused by the heat-treatment that has been performed on the samples with PEDOT:PSS electrodes. In fact, as stated for example in [63], thermal annealing is known to oxidize Fe^{2+} to Fe^{3+} in lithium niobate. Another possible explanation is that the polarization reversal responsible for the sign change of the photogalvanic current is not homogeneously completed along the whole film volume. If some domains with

polarization in the initial state remain, the current coming from those regions have an opposed sign with respect to the bulk contribution, resulting in an overall decrease of the absolute value of the current.

An issue that could complicate (and partly explain) the strange behaviour of the photogalvanic current in dataset A is that the I-V curves, with or without illumination, sometimes present an unexpected lack of repeatability: the same measurement, performed in the same conditions in different moments can give different results. In figure 5.38 is shown an example for the electrode 9.10.A, where 6 consecutive positive voltage ramps were measured one right after the other during a total time of about 1 hour. This change appears to work as an overall multiplicative factor in the I-V characteristic, with or without light. The multiplicative factor becomes smaller and smaller as time goes by, hinting that some sort of "degradation" is going on in the PEDOT:PSS electrodes.

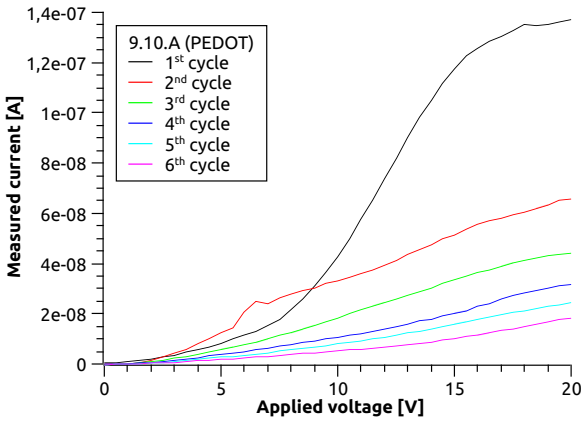

Figure 5.38: *I-V curves for the 9.10.A electrode showing the time-dependent behaviour often measured for PEDOT:PSS electrodes.*

As a tentative approach, we scaled the I-V curve in dark conditions and the I-V curves under illumination down to match the current reached at 22 V by the I-V curve at highest intensity. In figure 5.39a are shown the I-V curves matching their currents at 22 V. The scaling process has been performed by dividing the curves by the ratio between their current at 22 V and the current at 22 V at full power, $I_{(22\ \mathrm{V})}/I_{\mathrm{P6}(22\ \mathrm{V})}$. Notice that the procedure of matching the currents at 22 V is based on a mere convenience choice. The photogalvanic currents extracted from the scaled I-V curves are presented in figure 5.39b.

The scaled results appear to be linearly dependent on the light intensity and a linear interpolation estimates a slope of $(-3.2 \pm 0.1) \times 10^{-10}$ A cm^2/W and a y-intercept of (-0.10 ± 0.07) nA. The obtained slope is slightly larger than that estimated for the ITO electrode and this could clearly be due to the scaling procedure. The measures at maximum light intensity could have not been at steady state yet, for example, causing the slope of the linear fit to be overestimated. Nonetheless, what is more important to observe is that the time dependence often encountered in measurements involving PEDOT:PSS affects also the photogalvanic currents. The reason why this problem arises has not been understood yet.

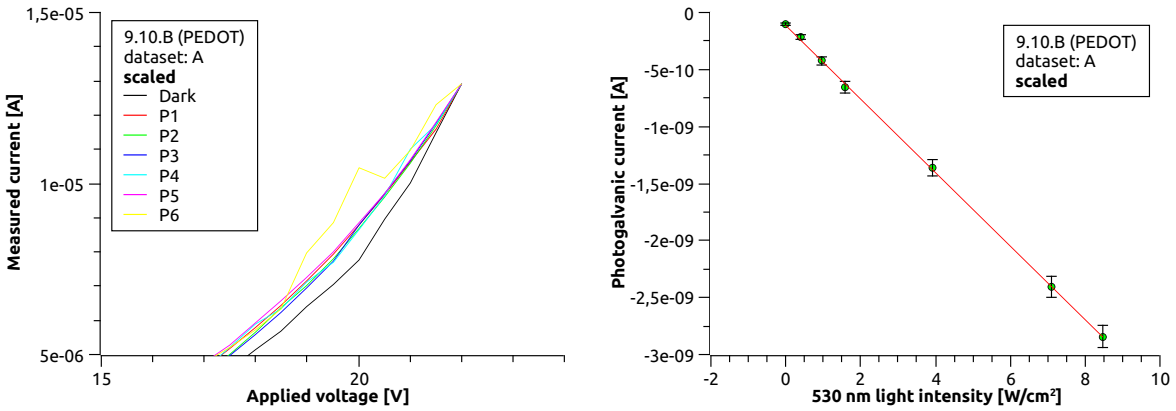

(a) (b)

Figure 5.39: *the matching of the I-V curves at 22 V after the scaling procedure and the photogalvanic currents obtained after the procedure. The linear interpolation of the data in (b) is represented by a red straight line.*

Chapter 6

Conclusions

In the present work we focused our attention on the electrical and photogalvanic properties of Fe:LN Smart-Cut™ samples with three different top electrodes. Aluminium was chosen as a prototypical metal electrode, while PEDOT:PSS and indium tin oxide were chosen because of their transparency in the visibile region as electrodes for measures under illumination.

In order to define a reliable measurement procedure, in section 5.1 we dealt with the transient behaviour of the current response of our samples, which could potentially complicate the analysis of experimental data. We studied the behaviour of the I-V curves at different settling time values, where the settling time is defined as the time for the source meter to wait before performing a current acquisition after applying a voltage. We found that a value of 3.5 seconds was the best tradeoff between the measurement precision and the time needed to measure a complete I-V characteristic.

The I-V curves measured in dark conditions have been studied in section 5.2. The analysis proceded by comparing the data with appriopriate models, which are discussed in section 3.2. In particular, Richardson-Schottky (R-S), Fowler-Nordheim (F-N), Poole-Frenkel (P-F) and high-field Mott's hopping models were considered.

For both Al and ITO electrodes, the R-S model estimated a dielectric constant close to what is found in literature, which is $\varepsilon_{33} = 28$. Still, for Al and ITO electrodes the P-F model measured a less precise dielectric constant, mainly around $\varepsilon_{33}/2$, but estimated an approximate trap concentration within the material between 10^{17} and 10^{19} cm^{-3}, which could correspond to a fraction of the iron or niobium antisites concentration in the Fe:LN film. As regards the PEDOT:PSS electrode, the conduction has been found to be qualitatively described by R-S or P-F.

The interfacial potential barrier was estimated by the F-N model to be of the order of 0.1 eV, much lower than the theoretical predictions, which are higher than 3 eV in all the considered cases. Moreover, the electron localization length was measured around 3 nm by the hopping model and was clearly not compatible with the small polaron localization length, which is instead of the order of the interatomic distances.

We conclude that R-S and P-F models are the most appropriate to describe charge conduction in our thin films under application of an external voltage.

The observation of current peaks in the dark I-V curves of PEDOT:PSS electrodes brought us to the study of the polarization switching currents, which is presented in section 5.3. The study was performed by analysing the dark I-V curves for two different PEDOT:PSS electrodes, which were measured with different combinations of settling time and acquisition time settings. We measured the main quantities related to the polarization switching: the coercive field, the internal residual field and the spontaneous polarization.

The coercive field, measured simply by marking the current-peak voltage, have been estimated to be between 28 and 43 kV/mm for positive applied voltages and between 45 and 58 kV/mm for negative applied voltages. The values are in line with other research works, were the coercive field is found to be of the order of 20 kV/mm. The residual field, measured as half of the difference between postive and negative coercive fields, was an indication of an additional field in the samples, probably due to polar defects. The measured values were between 7 and 11 kV/mm.

The spontaneous polarization was estimated as the total charge that flowed in the circuit during the application of a triangular voltage ramp. Altough some results were in line with the commonly measured value of 70 $\mu C/cm^2$ for congruent $LiNbO_3$, this method for the estimation of the polarization was found to be dependent on the measurement parameters. This suggested a non-trivial time profile of the poling currents. Also, the polarizations obtained from positive and negative current peaks resulted always different one from the other and this was imputed to the asymmetry of the I-V curves combined with the variation of the band diagram of the heterostructures during the acquisition of the I-V curves. Again, the measured difference was probably due also to the lack of information about the time profile of the poling currents.

The study proceded in section 5.4 with the measure of the photogalvanic currents for the two transparent electrodes at two different wavelengths, 405 and 530 nm. The photogalvanic current was estimated as the zero-volt current obtained from I-V curves measured under illumination. The characterization of the LEDs irradiance, reported in section 4.2.2, allowed the analysis of the dependence of photogalvanic currents on the light intensity.

As regards the ITO electrode, for both wavelengths the photogalvanic currents were in good agreement with the expected linear dependence of J_{PG} on the light irradiance I. The currents were analysed by performing linear interpolations. The ratio of the slopes at 530 and 405 nm is a parameter independent from the Fe^{2+} concentration, which is unknown in our samples, and thus its computation allowed us to compare our results with those of other works. Two different datasets produced ratios of 0.39 ± 0.02 and 0.38 ± 0.2 respectively, which were in good agreement with the theoretical value of about 0.37. The sign of the photogalvanic currents was not consistent with what expected from the voltage ramps that were used for measuring the I-V curves.

For what concerns the PEDOT:PSS electrode, instead, measured currents appeared to be lower than expected from previous measurements. The lower measured slope was probably due to incomplete polarization switching or to a decrease of the Fe^{2+} concentration after the thermal annealing performed on the PEDOT:PSS samples during their preparation. Moreover, the results for the 530 nm illumination presented a strange behaviour. This was partially attributed to a lack of repeatability of the I-V curves, which was probably caused by some sort of ongoing degradation of the PEDOT:PSS electrodes during the characterization and which was observed to affect also the photogalvanic currents.

As a perspective, the modeling of the conduction mechanisms in our samples could be improved by studying the dark I-V characteristics in a temperature controlled environment. The discrimination between the different models could become even more clear and the analysis of a series of temperature-dependent I-V curves would provide access to additional physical quantities, for example a more correct estimation of the height of the potential barrier at the interfaces. Finally, after the first characterization of the polarization switching currents in the PEDOT:PSS electrodes, this phenomenon could be further investigated by studying its time evolution as a response to defined voltages inputs with an oscilloscope.

Appendix A

A poling current measure with an oscilloscope

A circuit like the one in figure A.1 can be used to study the time-dependent current response of the Fe:LN film under the application of particular voltage inputs. The idea is to generate a custom input signal with an arbitrary function generator (A. F. G.), to amplify it if needed and to apply it to the sample. Then, the current output of the sample can be converted by a load resistor into a voltage, which can be read and displayed by an oscilloscope.

The generator at our disposal (HMF2550 from Hameg) has a maximum output of 10 V_{pp}. The signal from the generator can be amplified by a TLE2141 operational amplifier, which in turn can be powered with a maximum of ± 22 V, allowing to amplify the signal up to 42 V_{pp}, which is sufficient to study the electrical properties of our 300 nm films. The resistor R_3 is needed in the circuit to reduce some high-frequency oscillations that interest the amplified signals when dealing with steep voltage ramps.

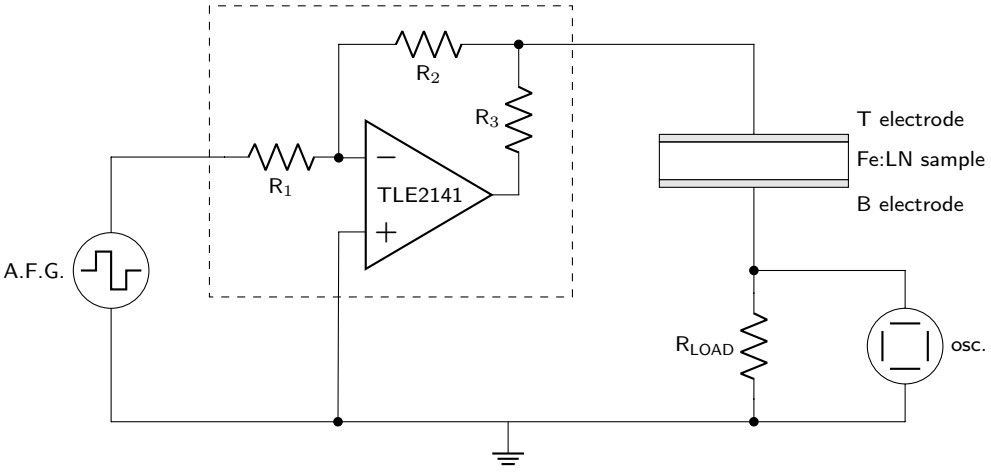

Figure A.1: *the circuit that would permit to study the current as a function of time.*

Bibliography

[1] IEA. *Global Energy Review 2019*. IEA, 2020.

[2] IEA. *Tracking Transport 2020*. IEA, 2020.

[3] IEA. *Electric Vehicles 2020*. IEA, 2020.

[4] IEA. *Global EV Outlook 2019*. IEA, 2019.

[5] IEA. *World Energy Outlook 2019*. IEA, 2019.

[6] N. L. Panwar *et al.* "Role of renewable energy sources in environmental protection: A review". *Renewable and Sustainable Energy Reviews* (2011).

[7] D. Cao *et al.* "High-Efficiency Ferroelectric-Film Solar Cells with an n-type Cu_2O Cathode Buffer Layer". *Nano Lett.* (2012).

[8] K. T. Butler *et al.* "Ferroelectric materials for solar energy conversion: photoferroics revisited". *Energy Environ. Sci.* (2015).

[9] S. Rühle. "Tabulated values of the Shockley–Queisser limit for single junction solar cells". *Solar Energy* (2016).

[10] V. M. Fridkin. *Photoferroelectrics*. 1979.

[11] L. Z. Tan *et al.* "Shift current bulk photovoltaic effect in polar materials - hybrid and oxide perovskites and beyond". *npj Comput Mater* (2016).

[12] I. Grinberg *et al.* "Perovskite oxides for visible-light-absorbing ferroelectric and photovoltaic materials". *Nature* (2013).

[13] A. Zenkevich *et al.* "Giant bulk photovoltaic effect in thin ferroelectric $BaTiO_3$ films". *Phys. Rev. B* (2014).

[14] V. M. Fridkin. "The bulk photovoltaic effect in the crystals without center of symmetry and solar harvesting". *Ferroelectrics* (2018).

[15] B. T. Matthias and J. P. Remeika. "Ferroelectricity in the Ilmenite Structure". *Phys. Rev.* (1949).

[16] R. S. Weis and T. K. Gaylord. "Lithium Niobate: Summary of Physical Properties and Crystal Structure". *Appl. Phys. A* (1985).

[17] K. Nassau *et al.* "Ferroelectric Lithium Niobate. 1. Growth, Domain Structure, Dislocations and Etching". *J. Phys. Chem. Solids* (1966).

[18] K. Nassau *et al.* "Ferroelectric Lithium Niobate. 2. Preparation of Single Domain Crystals". *J. Phys. Chem. Solids* (1966).

[19] S. C. Abrahams *et al.* "Ferroelectric Lithium Niobate. 3. Single Crystal X-Ray Diffraction Study at 24 °C". *J. Phys. Chem. Solids* (1966).

[20] S. C. Abrahams *et al.* "Ferroelectric Lithium Niobate. 4. Single Crystal Neutron Diffraction Study at 24 °C". *J. Phys. Chem. Solids* (1966).

[21] S. C. Abrahams *et al.* "Ferroelectric Lithium Niobate. 5. Polycrystal X-Ray Diffraction Study Between 24 °C and 1200 °C". *J. Phys. Chem. Solids* (1966).

[22] M. Sumets. "Thin films of lithium niobate: potential applications, synthesis methods, structure and properties". *Lithium Niobate-Based Heterostructures*. 2018.

[23] K. K. Wong. *Properties of Lithium Niobate*. 2002.

[24] Y. Liu H. Hatano K. Kitamura. "Growth and Photorefractive Properties of Stoichiometric $LiNbO_3$ and $LiTaO_3$". *Photorefractive Materials and Their Applications 2*. 2007.

[25] T. Volk and M. Wöhlecke. *Lithium Niobate*. 2008.

[26] M. Jazbinšek. "Material tensor parameters of $LiNbO_3$ relevant for electro- and elasto-optics". *Appl. Phys. B* (2002).

[27] A. M. Glass *et al.* "High-voltage bulk photovoltaic effect and the photorefractive process in $LiNbO_3$". *Appl. Phys. Lett.* (1974).

[28] V. M. Fridkin and R. G. Magomadov. "Anomalous photovoltaic effect in $LiNbO_3$:Fe in polarized light". *JETP Letters* (1979).

[29] A. P. Wilkinson *et al.* "The defect structure of congruently melting lithium niobate". *J. Appl. Phys.* (1993).

[30] I. Nee *et al.* "Role of iron in lithium-niobate crystals for the dark-storage time of holograms". *J. Appl. Phys.* (2000).

[31] D. Kip *et al.* "Holographic Measurement of Dark Conductivity in $LiNbO_3$:Ti:Fe Planar Optical Waveguides". *physica status solidi (a)* (1998).

[32] I. B. Barkan *et al.* "Transient optical storage in lithium niobate crystal". *Sov. J. Quantum Electron* (1979).

[33] L. Vittadello *et al.* "A polaron approach to photorefractivity in Fe:$LiNbO_3$". *J. Phys. Commun.* (2018).

[34] O. F. Schirmer *et al.* "Bulk photovoltaic effect of $LiNbO_3$:Fe and its small-polaron-based microscopic interpretation". *Phys. Rev. B* (2011).

[35] W. Li *et al.* "Fabrication and Characteristics of Heavily Fe-Doped $LiNbO_3$/Si Heterojunction". *Materials* (2019).

[36] J. G. Simmons. "Conduction in thin dielectric films". *J. Phys. D: Appl. Phys.* (1971).

[37] J. Bardeen. "Surface States and Rectification at a Metal Semi-Conductor Contact". *Phys. Rev.* (1947).

[38] R. M. Hill. "Poole-Frenkel Conduction in Amorphous Solids". *Philosophical Magazine* (1971).

[39] N. Mott and R. W. Gurney. *Electronic Processes in Solids*. 1948.

[40] A. Rose. "Space-Charge-Limited Currents in Solids". *Phys. Rev.* (1955).

[41] M. A. Lampert. "Simplified Theory of Space-Charge-Limited Currents in an Insulator with Traps". *Phys. Rev.* (1956).

[42] M. A. Lampert. "Volume-controlled current injection in insulators". *Phys. Prog.* (1964).

[43] N. Aspley and H. P. Hughes. "Temperature- and field-dependence of hopping conduction in disordered systems, II". *Philosophical Magazine* (1975).

[44] B. Aspar *et al.* "Basic mechanisms involved in the Smart-Cut™ process". *Microelectronic Engineering* (1997).

[45] Y. Shuai *et al.* "Fabrication of Y128- and Y36-cut lithium niobate single-crystalline thin films by crystal-ion-slicing technique". *Japanese Journal of Applied Physics* (2018).

[46] M. D. Tyona. "A theoritical study on spin coating technique". *Advances in materials Research* (2013).

[47] S. Jäckle *et al.* "Junction formation and current transport mechanisms in hybrid n-Si/PEDOT:PSS solar cells". *Scientific Reports* (2015).

[48] W. C. Chen *et al.* "Theoretical and Experimental Characterization of Small Band Gap Poly(3,4-ethylenedioxythiophene methine)s". *Macromolecules* (2004).

[49] Y. Park *et al.* "Work function of indium tin oxide transparent conductor measured by photoelectron spectroscopy". *Appl. Phys. Lett.* (1996).

[50] *Series 2600A System SourceMeter, Reference Manual.* 2011.

[51] M. Luennemann *et al.* "Improvements of sensitivity and refractive-index changes in photorefractive iron-doped lithium niobate crystals by application of extremely large external electric fields". *J. Opt. Soc. Am. B* (2003).

[52] Y. Noguchi *et al.* "Electronic Origin of Defect States in Fe-Doped $LiNbO_3$ Ferroelectrics". *Advances in Condensed Matter Physics* (2016).

[53] J. Yang *et al.* "First-principles investigations of the physical properties of lithium niobate and lithium tantalate". *Physica B* (2013).

[54] L. Pintilie. "Charge Transport in Ferroelectric Thin Films". *Ferroelectrics - Physical Effects.* 2011.

[55] Keun Woo Lee *et al.* "A two-dimensional DNA lattice implanted polymer solar cell". *Nanotechnology* (2011).

[56] M. R. Morris *et al.* "Effect of Internal Electric Fields on Charge Carrier Dynamics in a Ferroelectric Material for Solar Energy Conversion". *Adv. Mater.* (2016).

[57] Z. Fan *et al.* "Perovskites for photovoltaics: a combined review of organic-inorganic halide perovskites and ferroelectric oxide perovskites". *J. Mater. Chem. A* (2015).

[58] G. F. Nataf *et al.* "Low energy electron imaging of domains and domain walls in magnesium-doped lithium niobate". *Sci Rep* (2016).

[59] G. Arlt and H. Neumann. "Internal bias in ferroelectric ceramics: Origin and time dependence". *Ferroelectrics* (1998).

[60] Venkatraman Gopalan *et al.* "The role of nonstoichiometry in 180° domain switching of $LiNbO_3$ crystals". *Applied Physics Letters* (1998).

[61] R. L. Byer. "Quasi-Phasematched Nonlinear Interactions and Devices". *Journal of Nonlinear Optical Physics & Materials* (1997).

[62] S. A. Basun *et al.* "Optical absorption spectroscopy of Fe^{2+} and Fe^{3+} ions in $LiNbO_3$". *Journal of Applied Physics* (2002).

[63] M. Falk and K. Buse. "Thermo-electric method for nearly complete oxidization of highly iron-doped lithium niobate crystals". *Appl. Phys. B* (2005).

Acknowledgements

I would like to thank the following people who have helped me during the course of this work: my supervisor Dr. Marco Bazzan, for his support and guidance; Prof. Andrea Sanson, for his availability; Prof. Enrico Napolitani for sharing the source meter; the technicians, in particular Dr. Nicola Argiolas and Dr. Luca Bacci for the help with the source meter and Dr. Carlo Scian for the sputtering depositions and thickness measurements; Dr. Davide Ferraro for sharing the cutting plotter; my collegue Paolo Andrea Wetzl for the companionship and the initial help with the wafer dicing; Giovanni De Nardus for taking part to the computational work.